Investigating Chemical Evolution of Complex Molecules in Massive Hot Cores Using Astrochemical Modeling

The University of Virginia

Christopher J. Barger

July 29, 2020

Abstract

Hot cores represent an intermediate stage of massive star formation. These objects are the result of collapsing dark clouds in the interstellar medium (ISM) prior to the formation of new stars and star systems that may eventually harbor life. A salient feature of these cores is their strong millimeter/sub-millimeter molecular line emission, indicating the presence of myriad terrestrial molecules including alcohols, aldehydes, carboxylic acids, esters, and nitriles (Herbst & van Dishoeck 2009; Garrod & Widicus Weaver 2013). As such, these sources are compelling to study and model. Astrochemical modeling of objects including hot cores has evolved from relatively simple gas-phase steady-state calculations (Herbst & Klemperer 1973), to gas-grain models (e.g. Viti & Williams 1999), to robust three-phase modeling accounting for gas-phase, grain-surface, and ice-mantle-chemistry (e.g. Garrod 2013). We use the three-phase astrochemical modeling code *MAGICKAL* to investigate the chemical dependence of cosmic-ray ionization rate and warm-up timescale in hot cores. We then compare our chemical and spectroscopic modeling results to observational data (Bisschop et al. 2007) to constrain the cosmic-ray ionization rate and warm-up timescale in four well-studied sources: NGC 6334 IRS 1, NGC 7538 IRS 1, W3(H_2O), and W33A. Furthermore, we advance our hot-core modeling technique to incorporate one-dimensional radiation hydrodynamics, which includes explicit spatial structure, physical histories of gas parcels, and temperature treatment. These additions allow for a more robust and self-consistent treatment of hot core chemistry, and we briefly discuss chemical behavior for this new regime, and address how our results compare to observational data toward Sgr B2(N2), a chemically-rich source located near the Galactic Center.

Acknowledgements

I wish to foremost thank my faculty advisor, Robin Garrod, for his continued support, mentoring, and patience throughout my undergraduate and graduate studies at The University of Virginia. He has helped to foster the knowledge and skills that have allowed me to be successful in the greatest of my academic pursuits thus far.

I would also like to thank secondary mentors and collaborators, who have helped me throughout my studies in astrochemistry. In particular, I would like to thank Eric Herbst, Ka Ho (Andy) Lam, Zhi-Yun Li, and Shane Davis for their helpful suggestions and contributions to my work. I could not have accomplished all I have without their help.

I wish to thank my fellow research-group members for their professional and emotional support in my graduate career. Eric Willis has not only been an invaluable asset in training and assisting me with my work, but one of the best friends anyone could ask for. I would be remiss if I did not also mention Aspen Clements, Miwha Jin, Jherian Mitchel-Jones, and Drew Christianson for their support and friendship.

Finally, I wish to thank the NASA Astrophysics Theory Program for partially funding my work (grant No. 80NSSC18K0558), and the helpful reviewers and editors from AAS publishing to help me disseminate a major part of my work.

Contents

Chapter 1

Introduction: Astrochemistry, Astrochemical Modeling, and Motivation

1.1 A Brief History and Overview of Astrochemistry

Astrochemistry is broadly defined as the study of molecules in space, and observations of these molecules has shaped the field for nearly a century. The presence of simple species in the interstellar medium (ISM) was suggested after observations of a transition of the CH radical in diffuse gas (Swings & Rosenfeld 1937). Other diatomic species including CN (McKellar 1940), CH^+ (Douglas & Herzberg 1941), and OH (Weinreb et al. 1963) were detected by radio emission shortly thereafter. Larger and more terrestrial molecules were later detected by a variety of single-dish instruments in the following years. The first detections of ammonia (NH_3) and water (H_2O) were made using the Hat Creek Observatory (Cheung et al. 1968; 1969) toward various regions including the Galactic Center, Orion, and W49. Both formaldehyde (H_2CO) and methanol (CH_3OH) were detected using NRAO 140 ft observations toward a variety of sources (Snyder et al. 1969; Ball et al. 1970). Since these primitive detections, and with the advent of high-resolution interferometers such as ALMA, over 200 molecular species ranging from 2 to 70 atoms in size have been detected in the ISM (McGuire 2018). Carbon-bearing species containing 6 or more atoms are generally considered to be complex organic molecules (COMs) (Herbst & van Dishoeck 2009).

Observations and molecular detections in space constitute just one of roughly three major branches of astrochemistry. Laboratory experiments and modeling, both chemical and astrochemical, are also important components of the field. Observational and experimental data from laboratory studies influence chemical and astrochemical modeling. Compelling astrochemical modeling results may inspire or warrant further observational and laboratory studies.

Observational astronomers use radio telescopes to survey objects in space for molecular emission lines, typically in millimeter to sub-millimeter frequencies. These frequencies mostly correspond to rotational transitions, which tend to dominate in cold regions of space. Astronomers can identify the presence of a molecule in a survey by confirming the presence of several of its characteristic emission lines in a given spectra. The molecule can then be incorporated into a chemical network which is used in astrochemical modeling.

Laboratory experiments aim to accomplish a variety of goals in the context of astrochemistry. One such goal is to elucidate reaction pathways, both formation and destruction, for molecules identified in space. These pathways are studied by performing gas-phase experiments, and ice experiments. Typical gas-phase experiments include but are not limited to flowing afterglow, ion cyclotron resonance, Fourier-transform mass spectrometry, and low-temperature supersonic flow techniques. These experiments can help identify reaction products and the rate at which the reaction occurs under a given set of conditions. For any given two-body reaction, the temperature-dependent rate coefficient, $\kappa(T)$ (cm^3 s^{-1}), can be parameterized as an Arrhenius equation

$$\kappa(T) = \alpha\Big(\frac{T}{300K}\Big)^{\beta} exp\Big(\frac{-\gamma}{T}\Big), \tag{1.1}$$

where α, β, and γ are the pre-exponential factor, temperature index, and reaction barrier respectively (Walsh & Millar 2014). These parameters and some rate coefficients themselves can be fit using pure chemical modeling, such as molecular dynamics and DFT calculations.

Another important aim of laboratory experiments is to probe surface reactions and surface-binding energies of molecular species. It is widely acknowledged that COMs likely do not form substantially in the gas-phase, but rather on the surfaces and within the mantles of interstellar dust grains (Garrod et al. 2008). Reactions on surfaces can be studied using ice experiments. Typically pure ices or ice mixtures are deposited on a surface and then irradiated with ultraviolet radiation, and in some cases warmed (e.g. Öberg 2009a; 2009b). Reaction products can then be identified by spectroscopy or spectrometry. Surface-binding energies are important for determining how strongly bound a species is to the dust-grain surface. These energies can be determined using a process called thermal- or temperature-programmed desorption (TPD). A TPD experiment slowly warms deposited ice and measures the rate at which a species desorbs (e.g. Öberg 2009c). The surface-binding energy, or desorption energy, E_{des}, can be calculated from the experiment using

$$\frac{dN(A)}{dt} = \nu_0 exp\Big(\frac{-E_{des}}{T}\Big)N(A), \tag{1.2}$$

where $N(A)$ represents a count of species A, ν_0, is a characteristic frequency for species A, and T is the temperature of the surface.

Once reaction pathways including reactants, products, branching ratios, Arrhenius parameters, and binding energies are constrained by experiments and chemical modeling, they are assigned to a chemical network to be used in astrochemical modeling, which will be discussed in the following section.

1.2 Astrochemical Modeling

There are a variety of astrochemical modeling codes that are catered to different physical regimes. Monte Carlo kinetics models have been employed to study reactions and molecular processes occurring on the surfaces of dust grains. In particular, microscopic Monte Carlo simulations have been developed and used (Cuppen

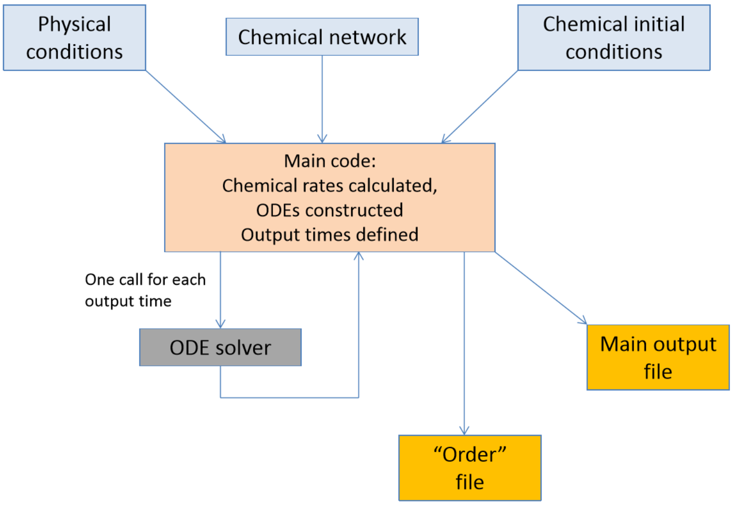

Figure 1.1: A schematic representation of a gas-phase or gas-grain model. *Credit: R. T. Garrod*

& Herbst 2005; Clements et al. 2018 and references therein) to study movement of particles on dust grain surfaces and particle deposition. These models track the positions of all particles explicitly, and particle movement is governed by random numbers. These models are computationally expensive, and may or may not include gas-phase chemistry. Alternatively, gas-grain models simulate gas-phase and grain chemistry together, and chemical evolution is governed by rate equations. This thesis features work that exclusively uses gas-grain models, which will be discussed in greater depth as follows.

Figure 1.1 illustrates a schematic representation of a gas-grain astrochemical kinetic model. The main code is responsible for calculating chemical rates using an ordinary differential equation solver (e.g. Gear's Algorithm) for specified output times. Initial conditions including elemental abundances, cosmic-ray ionization rate, initial H_2 and CO column densities, initial (and final, if applicable) local gas densities and temperatures are read into the code, often by a control file. The chemical network containing a comprehensive and self-consistent list of chemical species, reactions and corresponding parameters are typically kept in reaction files and also read into the main code.

Since conditions in space rarely permit chemical equilibrium, most gas-grain codes evolve chemistry using kinetics, which is solved by a system of differential equations (Herbst & Millar 2008). Consider the arbitrary two-body reaction to produce a single product

$$A + B \longrightarrow C. \tag{1.3}$$

The rate of increase in abundance for species C per unit time (cm^{-3} s^{-1}) is given as

$$\frac{dn(C)}{dt} = \kappa n(A)n(B), \tag{1.4}$$

where κ is the reaction rate coefficient (Equation 1.1), and n(A) and n(B) are the abundances of species A and B respectively. This process can apply to any binary chemical process. There are several types of binary reactions that form and destroy species in both the gas phase and on grain surfaces. Furthermore, species can be transferred to the grain surface from the gas phase by accretion, or transferred to the gas phase from the grain surface by desorption. To solve for the overall change in abundance over time for a given species i in the gas phase, the differential rate law (Equation 1.4) for each unique reaction that results in formation or destruction must be summed with all others following

$$\frac{dn_i}{dt} = \sum_{j,k} k_{jk} n_j n_k + \sum_l k_l n_l - n_i \big[\sum_m k_{im} n_m + \sum_n k_n \big] + k_{des} n_{i,s} - k_{acc} n_i. \quad (1.5)$$

Here, the first two sums on the right-hand side represent formation processes, whereas the two sums in brackets represent destruction processes. The last two terms represent the rates of desorption and accretion respectively. Gas-grain codes solve this equation for each species in each phase at each output time (Figure 1.1).

The advent of gas-grain modeling began with a simple gas-phase model introduced by Herbst & Klemperer (1973). This model solved steady-state chemistry for a network of a few dozen species. Quasi gas-grain models (e.g. Viti & Williams 1999) were developed thereafter, however their treatment of grain surface chemistry is over-simplistic. Hasegawa et al. (1992) introduced a full two-phase model in which both gas-phase and grain-surface chemistry were modeled. Hasegawa & Herbst (1993) introduced the first three-phase astrochemical model in which species present in the bulk ice mantles of dust grains were also considered. Lately the three-phase modeling approach has been revised to include an active ice mantle, in which proximal radicals can react to form new species below the surface of the ice. Garrod (2013) introduced such a model called *MAGICKAL* (Model for Astrophysical Gas and Ice Chemical Kinetics and Layering) to simulate the chemistry of hot cores (see section 1.3), and it is the model on which all the work presented here is based.

1.3 Astronomical Sources

This section briefly discusses different well-studied environments in the ISM, and important features of each.

1.3.1 Diffuse Clouds

Diffuse clouds are regions of the ISM with gas densities on the order of 10^2 to 10^3 cm^{-3}, gas temperatures of roughly 100 K, and visual extinctions on the order of 1 magnitude (Table 1.1). Dust temperatures are likely lower and uncoupled with gas temperatures due to the relatively low gas densities. The chemistry of diffuse clouds is relatively simple. Most of the hydrogen occurring in these sources is atomic, though a small fraction may be molecular (Duley & Williams 1984). Simple molecules incliding CO, OH, HCN, and CS have been detected toward diffuse clouds such as ζOph (Liszt 2020), however, more complex chemistry does not occur due to a high flux of ultraviolet radiation.

1.3.2 Dark Clouds

Dark clouds are denser, colder, and more obscured than diffuse clouds. Gas densities are on the order of 10^4 cm^{-3}, gas and dust temperatures are coupled at about 10 K, and visual extinctions are on the order of 10 magnitudes (Table 1.1). Here, most

Table 1.1: Important parameters of well-studied astronomical sources.

Source Type	Gas Density (cm^{-3})	Gas Temperature (K)	A_v
diffuse clouds	10^2 - 10^3	50-100	10^0
dark clouds	10^4	10	10^1
pre-stellar cores	10^5 - 10^7	10	10^2
hot cores	10^6 - 10^9	100+	10^2

hydrogen is molecular, and other simple molecules including CO, H_2CO, and NH_3 exist (Duley & Williams 1984). These sources are colder than diffuse clouds due to more efficient radiative cooling by molecules. TMC-1 CP is one of the most well-studied and modeled dark cloud environments (e.g. Garrod et al. 2007), and contains simple molecules in addition to many unsaturated hydrocarbon species (Herbst & Millar 2008).

1.3.3 Pre-stellar Cores

Pre-stellar cores are thought to result from collapsing gas clouds, and precursors to star-formation. These objects have gas densities on the order of 10^5 to 10^7 cm^{-3}, dust temperatures of about 8 K, gas temperatures of about 10 K, and visual extinctions of about 100 magnitudes (Table 1.1). A noteworthy feature of these objects is that there is apparent depletion or freeze-out, especially of CO (Bergin et al. 2002) due to very cold dust temperatures.

1.3.4 Hot Cores

Hot cores are sources where massive star formation is beginning to occur. These objects have high gas densities, typically in excess of 10^7 cm^{-3}, temperatures above 100 K, and visual extinctions in excess of 100 magnitudes (Table 1.1). These sources feature rich COM line emission (Herbst & van Dishoeck 2009; Garrod & Widicus Weaver 2013; Garrod 2013). The presence of a great variety of terrestial COMs in these sources is believed to be attributed to warm and dense physical conditions. These diverse molecules may become incorporated into star systems, and some such as glycine and glycolaldehyde may be precursors to life (Garrod 2013). As such, hot cores are attractive objects to study, and are the focus of the work featured in this thesis.

1.4 Project Motivation

The work presented in this thesis is organized into two parts. The first aims to understand the chemical evolution of hot cores in the context of comsic-ray ionization rate, and chemical warm-up timescale, and the second aims to assess chemical evolution of hot cores using more accurate and consistent modeling techniques. The motivation for these parts are discussed briefly in the following subsections.

1.4.1 Investigating Cosmic-Ray Ionization Rates and Warm-up Timescales

Cosmic rays are energetic subatomic particles, consisting mostly of protons, ejected from exploding stars and galaxies with strong polar outflows of radiation. They affect the chemistry of the ISM by two dominant processes: they collide with and excite gas-phase H_2, which generates ionizing and photo-dissociating photons (Prasad & Tarafdar 1983), and also ionize H_2 and other gas phase species directly. In the gas phase, these processes generate simple molecules including water, methane, and ammonia. For example, Duley & Williams (1984) demonstrate that water can be formed by cosmic-ray ionization of H followed by successive reactions with O and H_2 via

$$\mathrm{H + CR \longrightarrow H^+ + e^- + CR} \tag{1.6}$$

$$\mathrm{H^+ + O \rightleftharpoons H + O^+} \tag{1.7}$$

$$\mathrm{O^+ + H_2 \longrightarrow OH^+ + H} \tag{1.8}$$

$$\mathrm{OH^+ + H_2 \longrightarrow H_2O^+ + H} \tag{1.9}$$

$$\mathrm{H_2O^+ + H_2 \longrightarrow H_3O^+ + H} \tag{1.10}$$

$$\mathrm{H_3O^+ + e^- \longrightarrow H_2O + H.} \tag{1.11}$$

On dust grains, cosmic-ray photons can induce photo-dissociation of simple ices to form a variety of radicals including OH, CH_3, CH_3O, NH_2, and others (Garrod et al. 2008). These radicals can then add to form a variety of COMs. Since cosmic rays are critical to chemical evolution in the ISM, the cosmic-ray ionization rate, ζ, is an important parameter to study. However, the effects of varying ζ on the rich chemistry of hot cores has not been previously investigated in great detail. Furthermore, although the chemical response to varying the hot core warm-up timescale has been investigated by Garrod (2013), the chemical effects of warm-up timescale in the context of changing ζ has not been studied.

In Chapter 2, I use the hot core modeling code *MAGICKAL* to construct a cosmic-ray fluence grid consisting of nine values of ζ and warm-up timescale, and study resulting time and temperature-dependent fractional abundances of COMs. Furthermore, I use a spectroscopic modeling technique to compare observational results of four well-studied hot cores with model results. The comparison aims to constrain ζ and the chemical warm-up timescale in these sources.

1.4.2 Incorporating Radiation Hydrodynamics into Hot Core Modeling

The three-phase gas-grain models discussed in section 1.2 are more extensive and comprehensive than primitive astrochemical models. However, aside from general modeling uncertainties such as reaction barriers, initial conditions, incomplete reaction schemes, etc., hot-core modeling has consistently lacked an appropriate treatment of the physical evolution of star formation. Hot core models have often treated the physical evolution as a two-stage process: an isothermal collapse to high density followed by a warm-up at a constant density (e.g. Viti & Williams 1999; Garrod

& Herbst 2006). Major shortcomings of this approach include the fact that temperature evolves as a free parameter, and is not coupled with density, no spatial structure is included, and the physical history of a particular gas parcel is ignored.

In Chapter 3, I present work that incorporates one-dimensional radiation hydrodynamics in *MAGICKAL* aimed to produce a more accurate and consistent model of hot cores. This work addresses the chemical behavior of various COMs for three different hot core sources, and discusses trends in fractional abundances at various source masses and mass accretion rates. A comparison of the modeled results with observations toward Sgr B2(N2) is also given.

Finally, Chapter 4 concludes this thesis with a description of future work to follow from what has been done here.

Chapter 2

Constraining Cosmic-Ray Ionization Rates and Chemical Timescales in Massive Hot Cores

C. J. Barger & R. T. Garrod

2.1 Introduction

Cosmic rays are vital to the evolution of chemical complexity in the interstellar medium (ISM), especially in high-extinction regions that UV photons are unable to penetrate. There are two dominant processes by which cosmic rays affect this chemistry: (i) the direct collisional ionization of atoms and molecules, most notably hydrogen, and (ii) collisional excitation of gas-phase H_2 in particular, to generate Lyman–Werner band photons that can ionize and dissociate other chemical species (Prasad & Tarafdar 1983). Importantly, process (i) leads readily to the production of the ions ${H_2}^+$, H^+ and He^+ in the gas phase. ${H_2}^+$ reacts easily with neutral molecular hydrogen to form ${H_3}^+$; this ion drives much of the ion-molecule chemistry in dense interstellar clouds, through proton donation to neutral species, and is responsible for the gas-phase formation of simple molecules including H_2O, NH_3, and CH_4 (Herbst & Millar 2008). The cosmic-ray-induced UV field can also influence the chemical evolution of dust-grain-surface ices, through the photodissociation of major ice constituents such as water, formaldehyde, methanol, ammonia, and methane, to generate radicals including OH, HCO, CH_3, CH_3O, CH_2OH, and NH_2. Under warm conditions in which these radicals become thermally mobile, they may react to form a variety of complex organic molecules (COMs; Garrod & Herbst 2006; Garrod et al. 2008).

The cosmic-ray ionization rate, ζ, is typically defined in chemical models as the rate at which H_2 is ionized, while the rates of ionization and dissociation of other species usually are defined in fixed ratios to this value. For species with an ionization potential or dissociation energy low enough to allow the relevant process to be initiated by the secondary Lyman–Werner field, and not only by direct cosmic-ray collision, the rates of those processes may be as much as several orders of magnitude greater than the base rate ζ.

Several techniques have been employed to measure the cosmic-ray ionization rate in different regions of the ISM. Measurement of ${H_3}^+$ abundance has been a popular avenue in determining ζ, due to its direct dependence on cosmic-ray ionization of H_2. Oka et al. (2005) used total column density measurements of H_3^+ to infer a value $\zeta = (2-7) \times 10^{-15}$ s^{-1} toward diffuse regions of the Galactic center. Le Petit et al. (2016) modeled H_3^+ chemistry in the same regions and calculated ζ to be on the order of 10^{-14} s^{-1}. Other studies have invoked alternative means of determining the cosmic-ray ionization rate elsewhere in the ISM. Van der Tak & van Dishoeck (2000) used CO and HCO^+ observations and modeling to derive $\zeta = (3 \pm 2) \times 10^{-17}$ s^{-1} toward select massive protostars. Van der Tak et al. (2006) mapped H_3O^+ toward Sgr B2 and calculated $\zeta = 4 \times 10^{-16}$ s^{-1}. Caselli et al. (1998) used fractional ionization rates of HCO^+ and DCO^+ to constrain ζ in the range of 10^{-18} to 10^{-16} s^{-1}. Ceccarelli et al. (2011) and Vaupré et al. (2014) also used measurements of HCO^+ and DCO^+ to constrain $\zeta = 10^{-15}$ s^{-1} in supernova remnants. Favre et al. (2018) used observations and modeling of c-C_3H_2 toward OMC-2 FIR4 to calculate $\zeta = 4 \times 10^{-14}$ s^{-1}.

Despite thorough investigation of ζ in these studies, it remains unclear how applicable these results are generally or to other, specific sources, especially for the purposes of understanding chemistry in high-mass star-forming cores (see below). Gaches et al. (2019) suggest that the determination of cosmic-ray ionization rates through the above techniques is only reliable when cosmic rays dominate source thermochemistry, which may not be the case.

Furthermore, these results and others from related studies (e.g. Webber 1998; Le Petit et al. 2004; Yusef-Zadeh et al. 2013) indicate that ζ varies by several orders of magnitude throughout the Galactic ISM. The variability suggests that assigning to a source a uniform or canonical ionization rate for the purposes of chemical modeling may not be appropriate; unique physical conditions can alter the local ζ within a source, even if ζ is constrained in the surrounding medium. Rimmer et al. (2012) calculated depth-dependent cosmic-ray ionization rates in an interstellar cloud, using a Monte Carlo method to consider attenuation by gas-phase particles and magnetic field-related losses. Padovani et al. (2009) and Padovani & Galli (2011) also used similar approaches, with varying treatments for the magnetic interactions and using different cosmic-ray fluxes from the literature. More recent work by Padovani et al. (2018) looked carefully at the role of the flux low-energy protons in such calculations. Rimmer et al. (2012) calculated ζ for visual extinctions up to 10 mag, while Padovani et al. (2009) obtained values to rather larger extinctions, corresponding to hydrogen column densities $N(H_2) \leq 10^{25}$ cm^{-2}. These two studies determined that the ionization rate should fall off as a power law with respect to hydrogen column density, with indices ranging from $a = 0.6$ to 1 (Rimmer et al. 2012) and from 0.4 to 0.8 (Padovani et al. 2009), while Padovani et al. (2018) also found the same general trend. Interstellar clouds or star-forming cores of greater column density should therefore experience lower cosmic-ray ionization rates, in cases where the ambient intercloud rate is otherwise the same. Accordingly, for an accurate understanding of local chemical conditions, ζ should be determined explicitly for a given source. Unfortunately, cosmic-ray ionization rates are poorly constrained by observations for many interstellar regions of chemical interest, including well-known star-forming sources known as hot cores.

Hot cores represent a transient stage of massive star formation that is characterized by strong molecular emission and the presence of a broad range of COMs. The temperatures and densities of these cores are typically greater than 100 K and

10^7 cm^{-3}, respectively (Choudhury et al. 2015). Given their high densities, local thermodynamic equilibrium (LTE) is usually a good approximation for modeling the line emission from the inner regions where most of the complex molecular material resides. COMs detected toward hot cores include alcohols, aldehydes, carboxylic acids, ethers, and esters (Garrod & Widicus Weaver 2013). As such, hot cores are compelling regions of study for detections of new COMs and/or prebiotic species (e.g. Belloche et al. 2014), although molecules of true biological significance, such as amino acids, have not yet been detected (see, e.g. Snyder et al. 2005).

The influence of the specific value of ζ on the chemistry of these rich and diverse regions has been little investigated, and it is unclear what value may be optimal for the production of COMs. The dominant paradigm currently used to explain the production of most COMs in hot cores relies on the cosmic-ray-induced UV photodissociation of simple grain-surface ice species such as methanol, producing radicals that may further react with each other if grain temperatures are high enough to allow them to become mobile (typically >20 K). The addition of radicals in this way thus leads to typically observed COMs like methyl formate ($HCOOCH_3$) becoming abundant on the grain surfaces, and which ultimately desorb into the gas phase when the protostar heats its envelope and thus the characteristic hot-core temperatures (>100 K) are achieved. However, the dominant destruction mechanism for gas-phase COMs in most chemical networks involves reaction with simple ions such as $H_3{}^+$, H_3O^+, and several others, whose abundances are also directly dependent on the cosmic-ray ionization rate. The product molecules formed as the result of photodissociation of smaller species on the grains may also be dissociated by the same means, either in the gas phase or on the grains, prior to thermal desorption. The observable abundances of COMs must therefore be dependent on the balance between cosmic-ray-induced formation and a set of separate but related cosmic-ray-induced destruction mechanisms.

Typical values of ζ used in astrochemical models are on the order of 10^{-17} s^{-1}. Garrod (2013, hereafter G13) and related modeling efforts have consistently used $\zeta = 1.3 \times 10^{-17}$ s^{-1}, following estimates for dark clouds (Duley & Williams 1993), while others have adopted a broader range of values; Shingledecker et al. (2018) modeled cold-core ice chemistry using values from 10^{-17} to 10^{-14} s^{-1}. Although some authors have recognized the necessity to consider ζ as a free parameter in hot-core models (Allen et al. 2018), there persists a lack of information about how molecular abundances trend with varying ζ in the gas and solid phases for hot cores. The picture is further complicated by the fact that the timescale for the exposure of both grain-surface and gas-phase species to CR-induced processing is also poorly constrained, especially during the important period at elevated temperatures when reactive radicals on the dust grains become mobile enough to produce COMs. The time taken for the temperature of the hot core to progress from cold-core values around 10 K to the characteristic hot-core temperature, i.e. the "warm-up" timescale, t_{wu}, has been often been assigned a range of values; Garrod & Herbst (2006) adopted three timescales ranging from $t_{wu} = 5 \times 10^4$ to 10^6 yr, corresponding to a temperature progression from 10 to 200 K, following the approach of Viti & Williams (1999). Subsequent gas-grain hot-core models have adopted a similar scheme. Values on the shorter end of this range have typically been found to reproduce observational fractional abundances the best (e.g Belloche et al. 2009). However, this determination has usually been made for models with fixed cosmic-ray ionization rate; ζ and t_{wu} may indeed share a degenerate effect on the chemistry, making the cosmic-ray *fluence* (i.e. the product ζt_{wu}) perhaps more meaningful than ζ itself.

Using the astrochemical kinetics code *MAGICKAL*, we study the effects of t_{wu} and ζ on the chemistry of hot cores using a grid of generic models run at various cosmic-ray fluences. We concentrate especially on COMs, with the goal of using their observed abundances in specific sources to constrain both t_{wu} and ζ appropriate to those sources. The particular prevalence of COMs in the dense centers of hot cores makes them good candidates to determine ζ specifically in those dense regions.

Past modeling studies of hot-core chemistry have typically used a comparison between modeled fractional abundances and observationally determined values (based on column density ratios) to determine the quality of the match between model and observational data. However, such methods ignore the spatial variation of molecular emission as a function of density, temperature, and fractional abundance, all of which may vary between sources. Determinations of column densities for particular molecules are also prone to error, especially with single-dish instruments, due to beam dilution. The spatial extents of individual species are likely to depend strongly on the local temperature, as attested by the wide range of excitation temperatures observed for different COMs, even toward the same source. This may be caused by differences in the binding energies of different species, or by the sensitivity of their chemical formation and destruction routes to thermal activation, or by the presence or absence of other species with which they may react under such conditions.

In order to take account of these effects in our comparison between models and observational data, we simulate explicitly the emission from a complement of COMs, using chemical abundance data from the generic model grid mapped onto observationally determined physical profiles for specific sources (van der Tak et al. 2000). The resultant integrated line intensities are then compared with observational values from the molecular line surveys of Bisschop et al. (2007, hereafter B07), following the same approach as G13. We assess the chemistry of the 13 molecules in the B07 survey, as well as glycine, and compare results for four hot-core sources studied by both van der Tak et al. and B07: NGC 6334 IRS 1, NGC 7538 IRS 1, W3(H_2O), and W33A. This analysis allows the best-fitting values of ζ and t_{wu} to be determined for each source.

Details of the specific methods used in this study are provided in Section 2.2. Analysis of the model results for individual chemical species is presented in Section 2.3, and the comparison with specific observational sources is given in Section 2.4. Discussion and conclusions follow in Sections 2.5 and 2.6.

2.2 Methods

To study the effects of the warm-up timescale, t_{wu}, and the cosmic-ray ionization rate, ζ, on the chemistry of hot cores, we implement the three-phase astrochemical modeling code *MAGICKAL*, outlined by G13. *MAGICKAL* integrates the time-dependent gas-phase, grain-surface, and ice-mantle fractional abundances by solving a system of rate equations. The essential details of this model are provided below. In order to compare the chemical results to specific observations in a meaningful way, spectral simulations are conducted, under LTE conditions, using chemical abundances from the models mapped onto spherically symmetric physical profiles for specific sources taken from the literature. The details of this treatment are provided in Section 2.2.2.

2.2.1 Chemical model: MAGICKAL

The chemical model employs a three-phase treatment conceived by Hasegawa & Herbst (1993) and further described by Garrod & Pauly (2011). The model uses the chemical network of G13, which includes gas-phase, grain-surface, and ice-mantle reactions. Although more recent work has been done in the laboratory for certain chemical systems relevant to COMs, the G13 model and network are self-consistent and have been tested extensively. The chemistry of methanol (CH_3OH) is considered to be of particular importance to the production of complex organics (e.g. Öberg et al. 2009a), and some laboratory studies have obtained values for important parameters for that system (e.g Rimola et al. 2014; Álvarez-Barcia et al. 2018). However, in the case of, e.g. Rimola et al. (2014), the analysis does not consider all of the reactions included in our network for the methanol system (i.e. H-abstraction reactions). For reasons of self-consistency, we retain the reaction barrier treatment for the hydrogenation of CO and H_2CO, and abstraction from various species in the methanol system used by G13, which is based on private communications of quantum rate calculations by F. Goumans and S. Andersson, bypassing the need for more basic thermal or tunneling calculations in the G13 code using activation barrier and width estimates.

In our model, surface species may be returned to the gas phase either by thermal desorption, reactive desorption, or photo-desorption; the yields for the latter are based on values provided by Öberg et al. (2009b, 2009c), with rates dependent on both the external and cosmic-ray-induced UV fields. Likewise, photodissociation of molecules may be induced by either field but is allowed to occur in all chemical phases. Ivlev et al. (2015) used a new approach for cosmic-ray impacts of individual dust grains; however, the process is stochastic in nature, and not readily compatible with our own work. Alternatively, Shingledecker et al. (2017) presented a new model for cosmic-ray interactions in solids; however, its accuracy remains unclear, and so incorporating this work into our model is not currently appropriate. The reactive desorption mechanism assumes an efficiency coefficient $a = 0.01$ (see Garrod et al. 2007), which yields desorption probabilities somewhat less than 1%. During the hot phase, thermal desorption is the dominant desorption process.

Several experiments demonstrate that chemical reactions occuring on interstellar dust grains are important to the production of COMs (e.g Öberg et al. 2009a; Butscher et al. 2016), and as such, grain chemistry is an important facet of our model. Barrier-mediated thermal diffusion rates determine the reaction rates of surface and bulk species; the diffusional coupling between these two phases is determined by bulk diffusion rates. For surface and bulk-ice reactions with activation energy barriers, reaction rates are based on the faster of the thermal reaction rate and the rate of tunneling through a rectangular barrier; the majority of rates are dominated by the tunneling contribution at the temperatures considered in these models. For activated reactions, simple competition between reaction and thermal diffusion of the reactants is calculated, to determine the overall efficiency of reaction per meeting of the reactants. For the surface chemistry only, the modified-rate approach introduced by Garrod (2008) is used to approximate the stochastic behavior of surface reactants, where applicable. Chemical pathways for glycine and similar species (i.e. glycinal, propionaldehyde, and propionoic acid) were incorporated into the chemical network by G13, adopting formation mechanisms consistent with the radical reaction scheme used for other COMs.

Physical Considerations

The physical evolution of the hot core is treated as a two-stage process, following Garrod & Herbst (2006), whose approach was based on that of Viti & Williams (1999). Stage 1 involves the freefall collapse of material of initial gas density $n_H = 3.0 \times 10^3$ cm^{-3}, increasing over a period of around 1 Myr to $n_H = 2.0 \times 10^8$ cm^{-3} following Belloche et al. (2014). The visual extinction takes an initial value of 2 and scales with $n_H^{2/3}$. The gas temperature is held at a constant 10 K, whereas the dust temperature is allowed to fall as a function of the visual extinction (see Garrod & Pauly 2011) from 16 to 8 K. The chemistry of stage 1 begins in an entirely atomic state, save for H_2; initial chemical abundances are those used by G13.

During stage 2 (warm-up), the dust temperature increases from 8 to 400 K, at a fixed gas density determined at the end of stage 1. Gas and dust temperatures are assumed to be well coupled owing to the high density; thus, the gas is allowed to take on the temperature of the grains as it rises to values above 10 K. Following Garrod & Herbst (2006), G13 adopted three values of the warm-up timescale: $t_{wu} = 5 \times 10^4, 2 \times 10^5$ and 10^6 yr. These characteristic timescales correspond to the progression from 8 to 200 K; G13 simply extended the temperature progression to 400 K. To these three possible warm-up timescales, a further six are added in this work.

Although in the single-point models employed here the temperature varies over time, in the spectral simulations the temperature is treated also as a proxy for the radial dependence of the chemistry. Thus, the more central regions of a hot core have progressed for a longer period of chemical and thermal evolution. This method avoids having to run multiple individual trajectories for each set of physical conditions, allowing the grid of generic models presented here to be applied to multiple observed sources. This approach also implicitly assumes that the thermal history of each parcel of gas in the radial distribution is dominated by its radial position and not, for example, the changing luminosity of a protostellar source. We leave such considerations to future modeling efforts.

Cosmic-Ray Fluence Grid

To allow an investigation of the dependence of hot-core chemistry on the cosmic-ray ionization rate and warm-up timescale, a 9×9 grid of models in t_{wu} and ζ is constructed (Table 2.1). Each such model begins with an identical stage 1 collapse. The total cosmic-ray fluence in each model during the warm-up period (as defined by the time to reach 200 K) is the product of t_{wu} (s) and ζ (s^{-1}), which we simply quote throughout as a unitless quantity.

The grid consists of nine values of ζ and t_{wu}, and incorporates the *large*, *medium*, and *small* values of t_{wu} (t_9, t_7, and t_5 respectively) used by G13 and others. Two intermediate t_{wu} (t_8 and t_6) are created and assigned values such that they are evenly spaced (logarithmically) among the originals. Four smaller t_{wu} ($t_4 - t_1$) are chosen, each of which is a factor of 2 shorter than the last.

Table 2.1: Cosmic-Ray Fluence Grid Parameters.

	Warm-up Timescale	Cosmic-Ray Ionization Rate	
Notation	Time to Reach 200 K (yr)	Notation	ζ(s^{-1})
t_1	3.13×10^{3}	ζ_1	2.60×10^{-18}
t_2	6.25×10^{3}	ζ_2	5.81×10^{-18}
t_3	1.25×10^{4}	ζ_3	1.30×10^{-17}
t_4	2.50×10^{4}	ζ_4	2.60×10^{-17}
t_5	5.00×10^{4}	ζ_5	5.20×10^{-17}
t_6	1.00×10^{5}	ζ_6	1.04×10^{-16}
t_7	2.00×10^{5}	ζ_7	2.08×10^{-16}
t_8	4.50×10^{5}	ζ_8	4.16×10^{-16}
t_9	1.00×10^{6}	ζ_9	8.32×10^{-16}

Table 2.2: Cosmic-Ray Fluences Corresponding to Each Model.

	ζ_1	ζ_2	ζ_3	ζ_4	ζ_5	ζ_6	ζ_7	ζ_8	ζ_9
t_1	2.6(-7)	5.3(-7)	1.3(-6)	2.6(-6)	5.1(-6)	1.0(-5)	2.0(-5)	4.1(-5)	8.2(-5)
t_2	5.1(-7)	1.1(-6)	2.6(-6)	5.1(-6)	1.0(-5)	2.0(-5)	4.1(-5)	8.2(-5)	1.6(-4)
t_3	1.0(-6)	2.3(-6)	5.1(-6)	1.0(-5)	2.0(-5)	4.1(-5)	8.2(-5)	1.6(-4)	3.3(-4)
t_4	2.0(-6)	4.6(-6)	1.0(-5)	2.0(-5)	4.1(-5)	8.2(-5)	1.6(-4)	3.3(-4)	6.6(-4)
t_5	4.1(-6)	9.2(-6)	2.0(-5)	4.1(-5)	8.2(-5)	1.6(-4)	3.3(-4)	6.6(-4)	1.3(-3)
t_6	8.2(-6)	1.8(-5)	4.1(-5)	8.2(-5)	1.6(-4)	3.3(-4)	6.6(-4)	1.3(-3)	2.6(-3)
t_7	1.6(-5)	3.7(-5)	8.2(-5)	1.6(-4)	3.3(-4)	6.6(-4)	1.3(-3)	2.6(-3)	5.2(-3)
t_8	3.7(-5)	8.2(-5)	1.8(-4)	3.7(-4)	7.4(-4)	1.4(-3)	3.0(-3)	5.9(-3)	1.2(-2)
t_9	8.2(-5)	1.8(-4)	4.1(-4)	8.2(-4)	1.6(-3)	3.3(-3)	6.6(-3)	1.3(-2)	2.6(-2)

Values of ζ are chosen to produce a degeneracy in the cosmic-ray fluence of the models running along the grid's lower left to top right diagonal (Table 2.2). The diagonal model of t_7 is assigned a standard value of $\zeta_3 = 1.3\times10^{-17}$ s^{-1} used by G13 and previous versions. The cosmic-ray fluence of this model equals 8.2×10^{-5} yr s^{-1}, and the ζ values for the on-diagonal models of other t_{wu} are chosen to be degenerate with this fluence, producing a set of values ranging from $\zeta = 2.60\times10^{-18}$ s^{-1} to 8.32×10^{-16} s^{-1}. Since the spacing between the original three t_{wu} is not precisely uniform, the grid is asymmetric and not all diagonals (except the principal diagonal) have the same fluence across each model. Timescales t_8 and t_9 are irregular, as are the ionization rates ζ_1 and ζ_2.

2.2.2 Spectral Modeling

The submillimeter spectral line survey of B07 provided integrated intensities for spectral lines in emission from 13 different molecules, for seven high-mass protostellar sources, with data obtained using the James Clerk Maxwell Telescope (JCMT) and the IRAM 30m telescope. The survey identified typically dozens of lines from each molecule, making this a rich data set for comparison with chemical models. In order to compare our results with the observations of B07 in a direct way, radiative transfer for each molecule detected in that survey is simulated using fractional abundance data from the chemical models, according to the method described by G13. This treatment requires information on the spatially dependent physical conditions within the source being modeled. Spherically symmetric temperature and density profiles for a selection of high-mass sources were fit by van der Tak et al. (2000), four of which were also included in the B07 study: NGC 6334 IRS 1, NGC 7538 IRS 1, W3(H_2O) and W33A. These four sources are thus the target of the spectral calculations.

For each individual simulation of one of the four sources, all temperature-dependent fractional abundance data from one of the models presented in Section 3 are mapped to the corresponding temperature in the profile of that source. This results in a spherically symmetric model of the source, in which the abundance of each molecule in the chemical models is defined, and for which the local emission and absorption coefficients can be calculated. Under the assumption of LTE, plane-parallel radiative transfer is calculated for lines of sight through the source, providing raw emission maps in the plane of the sky for each frequency channel. Spectroscopic information for the calculation of the absorption and emission coefficients relating to each molecule is obtained from the Cologne Database for Molecular Spectroscopy[1] and from the JPL molecular spectroscopy database[2].

Following the radiative transfer calculations, the emission maps are convolved with a Gaussian beam at the on-source position. The beamwidth is frequency dependent and corresponds to the telescope used for the simulation, which is either the JCMT or IRAM 30m, depending on which instrument was used to obtain which line in the B07 survey. The individually simulated and convolved frequency channels are then used to construct simulated spectra for each observed line. The lines observed by B07 were generally unblended, but to ensure the same in these simulations, radiative transfer for each line was modeled separately. The resulting spectral emission for each line was then integrated to produce a value directly comparable with the integrated intensities quoted by B07. A frequency resolution of $\sim$400 kHz per channel was used in the simulations. Line widths for each source were taken from the average values quoted by B07, and were in the range of 4 – 6 km/s for the four sources simulated here.

Since we are also interested in the chemistry of glycine and the prospect of its detection in the ISM, we run spectral simulations of it following the same method described here. We use the six lines in ALMA band 6 that were studied by G13. Likewise, each line is modeled separately with the same frequency resolution used for all other simulations. Following G13, we convolve the emission using a beam size of 0.4 arcsec, which is within current ALMA capabilities.

2.2.3 Population Diagrams

After obtaining line-integrated intensities from the spectroscopic model, we employ the population diagram technique described by Goldsmith & Langer (1999). The integrated intensities are used to derive upper-level populations, which are then plotted as a function of excitation energy to derive total source-averaged molecular column densities (N_{tot}) and excitation temperatures (T_{ex}). If LTE conditions apply and external pumping mechanisms are negligible, excitation temperatures are representative of the kinetic gas temperatures at which molecules emit radiation.

The optical depth, τ, for each frequency channel is calculated explicitly from absorption coefficients in the radiative transfer simulations. Some of the lines of

---

[1] https://cdms.astro.uni-koeln.de

[2] https://spec.jpl.nasa.gov/

interest in the B07 survey are calculated to have non-negligible optical depths in our simulations. To allow such lines to be used in the population diagrams, a correction factor is applied to their upper-level column densities (N_u). The correction factor is given by Herbst & van Dishoeck (2009) as $C_\tau = \frac{\tau}{1-e^{-\tau}}$. The value of τ used to determine the correction factor in our simulations is that calculated for the line-center channel.

2.3 Model Results

The following subsections detail the chemical and physical model results. Chemical mechanisms and fractional abundance trends across the cosmic-ray fluence grid are explored for 14 molecules of interest. These include the 13 detected by B07, while – to follow up on the study by G13 – the results for glycine, the simplest amino acid, are also considered. Analysis of the chemical results includes the use of the population diagram technique to derive source-averaged column densities and excitation temperatures.

2.3.1 Chemistry

Time- and temperature-dependent fractional abundance plots for pertinent species are provided for selected models from the grid in Figures 2.1 – 2.5. The chemistry of each molecule is briefly recounted in the following subsubsections, including a description of the main formation and destruction reactions for each. It should be noted that, for the sake of simplicity, only the most influential reactions are discussed. Descriptions of the chemistry are given in the context of the different models with varying t and ζ values; thus, the relative influence of individual mechanisms can vary between the models. The subscript labels (g) and (s) applied to the names of molecules refer to their gas phase and solid phase (i.e. grain surface/mantle), respectively.

In general, molecules may be formed on grains at low temperature by hydrogenation and at somewhat higher temperatures (>20 K) by radical addition. Following their formation, molecules may be destroyed on grains via H-atom abstraction by the surface radicals $OH_{(s)}$ and $NH_{2(s)}$, and by cosmic-ray-induced photo-dissociation (CRPD). Radical-radical and H-addition reactions tend to be more effective as ζ increases, because radicals are produced at greater rates, via CRPD of major grain constituents.

COMs thermally desorb at higher temperatures, typically around 100 K or higher. Large ice abundances do not necessarily translate to large gas abundances, due to the prominence of destruction processes on grains (see Table 2.3 for a summary of highest amd lowest grain-and gas-phase abundances). Once released into the gas phase, molecules are typically destroyed through protonation by HCO^+ and H_3O^+. Once protonated, they recombine with electrons to form a variety of fragments. In the G13 network, the production of a hydrogen atom and a single, stable molecule as the result of electronic recombination of a protonated molecule is assumed to occur in only 5 % of cases, where such fractions have not been experimentally determined. Protonation reactions become more efficient as ζ increases, because cosmic-ray ionization increases gas-phase ion and electron abundances (Figure 2.1).

Table 2.3: Highest and Lowest Peak Grain- and Gas-Phase Fractional Abundances among All Models.

species	highest (solid)	highest (gas)	lowest (solid)	lowest (gas)
CH_3OH	1.0(-5)	1.0(-5)	9.0(-6)	6.0(-11)
H_2CO	2.0(-5)	1.0(-5)	2.0(-6)	3.0(-10)
HCOOH	3.0(-7)	8.0(-8)	1.0(-9)	1.0(-11)
CH_3CHO	3.0(-6)	4.0(-7)	6.0(-8)	5.0(-9)
CH_2CO	6.0(-7)	2.0(-7)	2.0(-9)	9.0(-11)
C_3H_4	5.0(-6)	1.0(-7)	5.0(-10)	2.0(-10)
CH_3OCH_3	4.0(-7)	1.0(-7)	6.0(-9)	8.0(-15)
CH_3OCHO	4.0(-7)	2.0(-7)	3.0(-7)	4.0(-14)
C_2H_5OH	5.0(-6)	2.0(-7)	3.0(-8)	2.0(-13)
NH_2CHO	1.0(-6)	1.0(-6)	8.0(-8)	3.0(-13)
HNCO	9.0(-8)	6.0(-8)	3.0(-9)	3.0(-11)
CH_3CN	1.0(-7)	6.0(-9)	9.0(-10)	3.0(-10)
C_2H_5CN	1.0(-6)	4.0(-8)	1.0(-8)	1.0(-11)
NH_2CH_2COOH	4.0(-8)	7.0(-10)	3.0(-13)	6.0(-18)

Thus, the cosmic-ray ionization rate is seen to influence both the formation and destruction of COMs in hot cores.

Methanol

Methanol (CH_3OH) forms on grains during the cold collapse stage, by successive H-atom addition to $CO_{(s)}$. Laboratory studies indicate that this process is efficient at low temperatures (Watanabe & Kouchi 2002; Hidaka et al. 2004). Methanol abundances on the grains remain essentially static in the warm-up prior to desorption in most t_{wu} and ζ models; however, methanol is significantly diminished at 30–40 K for the $t_{wu} = t_9$, $\zeta = \zeta_9$ model (Figure 2.2, panel $t_9\zeta_9$). This is due to CRPD and to H abstraction by $OH_{(s)}$. These processes are rapid for large ζ, and large t_{wu} values permit them to occur for longer times. CRPD produces $CH_{3(s)}$, $CH_3O_{(s)}$, and $CH_2OH_{(s)}$ radicals with branching ratios (1/1/5) taken from Öberg et al. (2009a). H abstraction by $OH_{(s)}$ also produces $CH_3O_{(s)}$ and $CH_2OH_{(s)}$. These radicals can be rehydrogenated by atomic H or by radicals capable of donating a hydrogen atom, and they may also donate a hydrogen atom to other reactive species, producing formaldehyde (H_2CO). However, reactions of these with other radicals may also engender formation of other COMs on the grains, including acetaldehyde, ethanol, dimethyl ether, and methyl formate.

Methanol desorbs in these models at around 110 K, and its gas-phase abundances remain mostly largely unchanged up to 400 K in the $t_{wu} = t_1$ models (Figure 2.2, panels $t_1\zeta_1$, $t_1\zeta_5$, $t_1\zeta_9$), which provide too little time to permit appreciable changes in abundance. However, for larger t_{wu} and especially large ζ, gas abundances are strongly diminished following thermal desorption of methanol (panels $t_5\zeta_9$, $t_9\zeta_5$, $t_9\zeta_9$). Gas-phase methanol destruction proceeds with the protonation of methanol by ${H_3O_{(g)}}^+$ to form ${CH_3OH_2}^+{}_{(g)}$. The latter recombines to give a variety of products with branching ratios following Geppert et al. (2006). Large ζ results in large abundances of ${H_3O_{(g)}}^+$ as it is formed indirectly following cosmic-ray ionization of

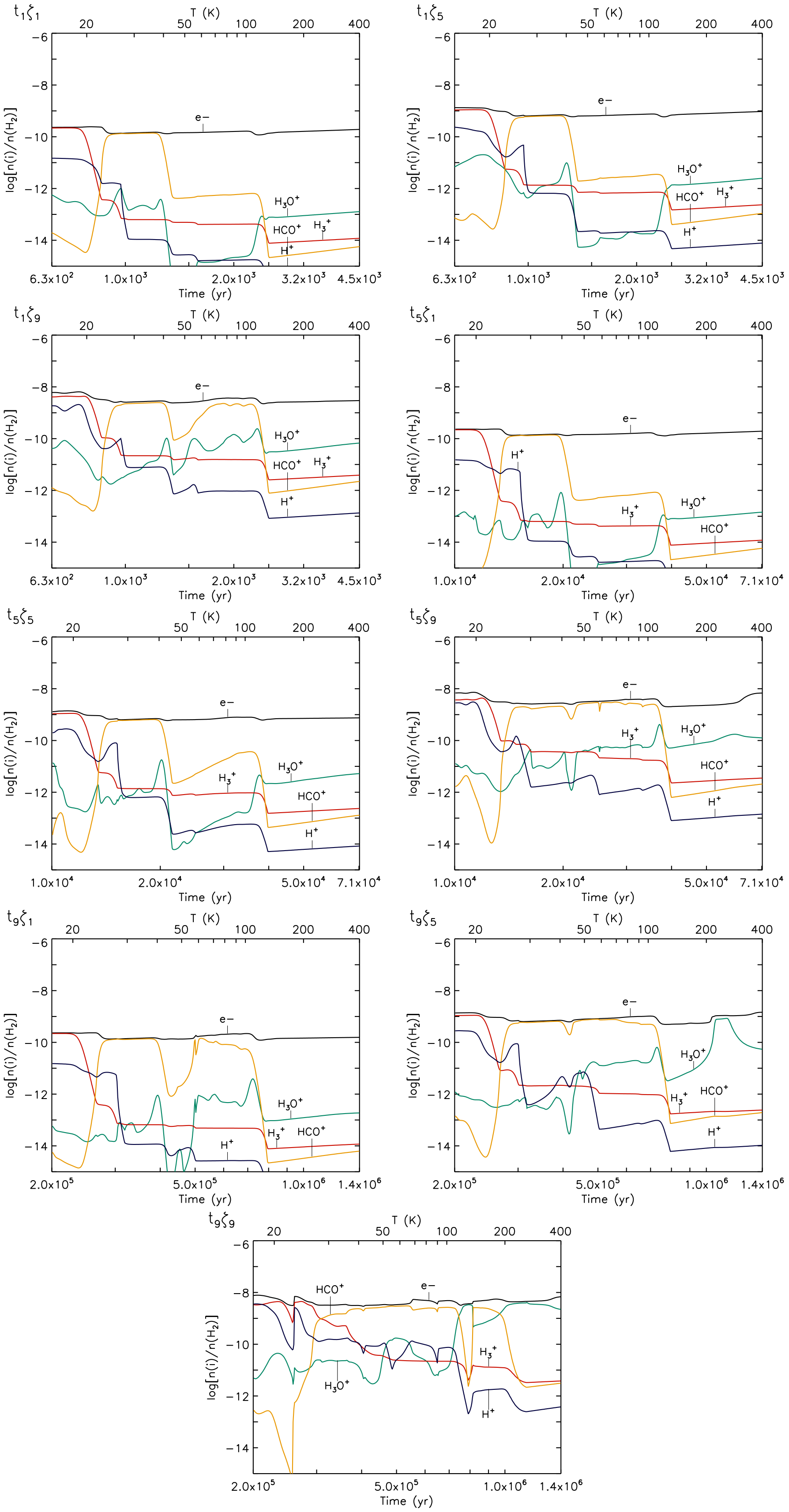

Figure 2.1: Select time- and temperature-dependent gas-phase fractional abundance plots (with respect to H_2) for electrons and important ions. The fractional abundance, time, and temperature (upper axis) are plotted logarithmically.

$H_{2(g)}$.

The largest grain and gas peak fractional abundances of methanol with respect to total hydrogen are both around 1×10^{-5}, and occur for small to medium ζ (Figure 2.2, $t_1\zeta_1$, $t_1\zeta_5$, $t_5\zeta_1$, $t_5\zeta_5$, $t_9\zeta_9$). Large abundances result from low influence of the grain-surface and gas-phase destruction reactions. Conversely, the smallest grain and gas peak fractional abundances are around 9×10^{-6} and 6×10^{-11}, respectively, and occur for $t_{wu} = t_9$, and $\zeta = \zeta_9$ (panel $t_9\zeta_9$).

Formaldehyde

Like methanol, formaldehyde forms on grains during the collapse stage by successive hydrogenation of $CO_{(s)}$. Likewise, its grain abundances are static until desorption for most conditions except for $t_{wu} = t_9$, and $\zeta = \zeta_9$ (Figure 2.2, panel $t_9\zeta_9$). Abundances are diminished at 30 K for those models, due to H abstraction by $OH_{(s)}$ to form $HCO_{(s)}$, which is a barrierless process.

Formaldehyde desorbs at 40 K, and its post-desorption gas abundances remain static up to 400 K for models with $t_{wu} = t_1$ and small to medium ζ (Figure 2.2, panels $t_1\zeta_1$, $t_1\zeta_5$). For larger t_{wu} and ζ (panels $t_5\zeta_9$, $t_9\zeta_5$, $t_9\zeta_9$), reaction with $H_{(g)}$ and $O_{(g)}$ destroys gas-phase formaldehyde to produce $HCO_{(g)}$; gas-phase abundances of atomic hydrogen and oxygen are larger for greater ζ values. A surplus of $H_{(g)}$ forms following the reaction

$$H_2{}^+{}_{(g)} + H_{2(g)} \rightarrow H_3{}^+{}_{(g)} + H_{(g)} \tag{2.1}$$

which is more rapid owing to more frequent cosmic-ray ionization of $H_{2(g)}$. $O_{(g)}$ forms via reaction

$$He_{(g)}{}^+ + CO_{(g)} \rightarrow He_{(g)} + C_{(g)}{}^+ + O_{(g)} \tag{2.2}$$

which is more rapid owing to more frequent cosmic-ray ionization of $He_{(g)}$.

Some models lead to a peak in gas-phase formaldehyde at 110-200 K (Figure 2.2, panels $t_1\zeta_9$, $t_5\zeta_5$, $t_9\zeta_1$). For these models, gas-phase methanol abundances are large, which permits efficient formation of protonated dimethyl ether, via the reaction

$$CH_3OH_{(g)} + CH_3OH_2{}^+{}_{(g)} \rightarrow CH_3OCH_4{}^+{}_{(g)} + H_2O_{(g)} \tag{2.3}$$

As well as forming a small fraction of dimethyl ether, in the G13 network the recombination of protonated dimethyl ether with electrons is allowed to produce formaldehyde:

$$CH_3OCH_4{}^+{}_{(g)} + e\text{-}_{(g)} \rightarrow H_2CO_{(g)} + CH_{4(g)} + H_{(g)} \tag{2.4}$$

The largest peak formaldehyde abundances on the grains are around 2×10^{-5}, and occur for $t_{wu} = t_5$ and $\zeta = \zeta_9$ (Figure 2.2, panel $t_5\zeta_9$). The largest peak gas-phase abundances are around 1×10^{-5}, and occur for $t_{wu} = t_1$ and $\zeta = \zeta_5$ (panel $t_1\zeta_5$). The smallest peak grain abundances are about 2×10^{-6} and occur for $t_{wu} = t_1$ and $\zeta = \zeta_1$ (panel $t_1\zeta_1$). The smallest peak gas-phase abundances are about 3×10^{-10}, and occur for $t_{wu} = t_9$ and $\zeta = \zeta_5$ owing to the high influence of gas-phase H-abstraction reactions.

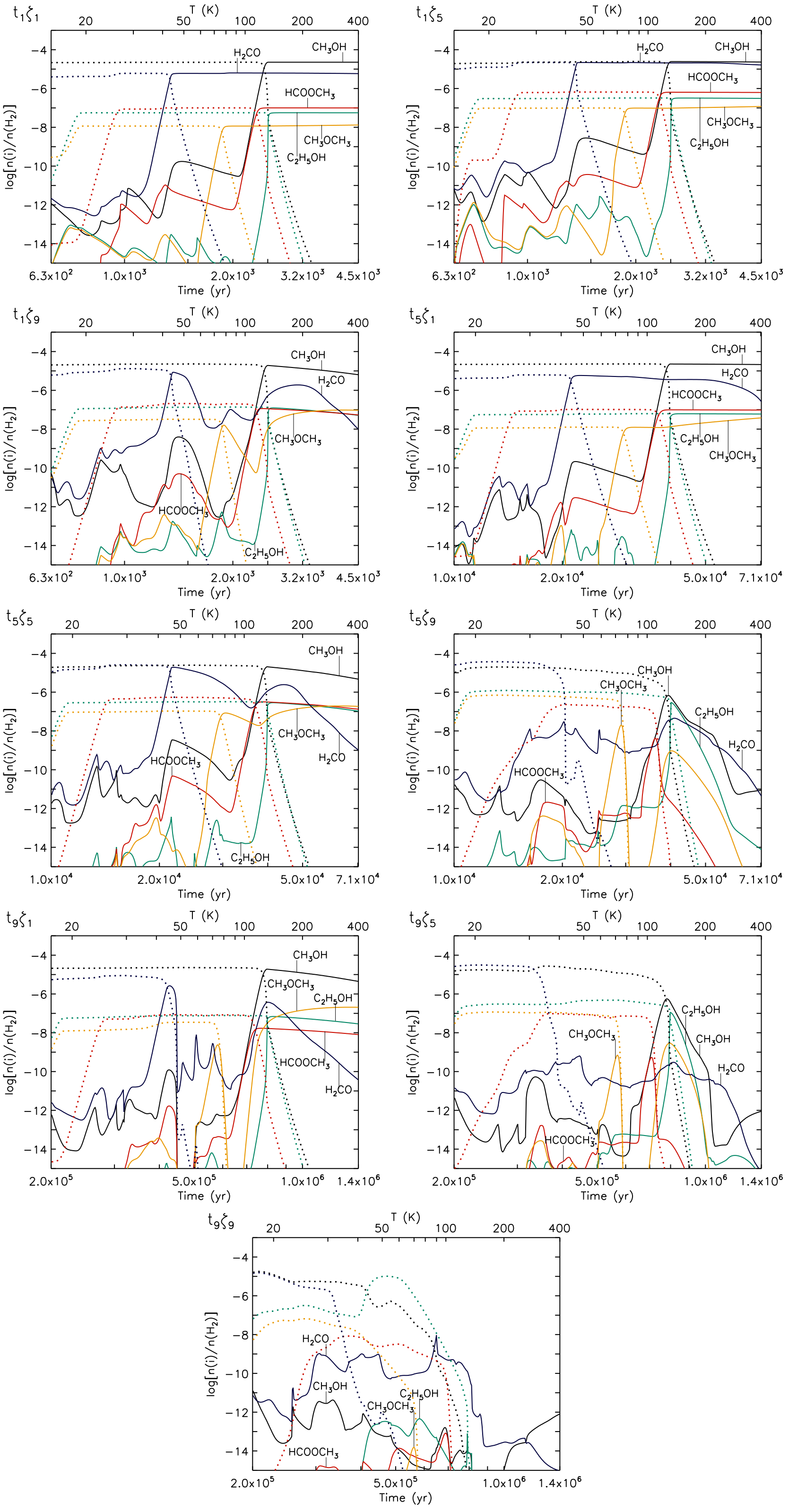

Figure 2.2: Select time- and temperature-dependent fractional abundance plots (with respect to H_2) for methanol (black), formaldehyde (blue), methyl formate (red), ethanol (green), and dimethyl ether (yellow). Dotted lines represent the sum of grain-surface and ice-mantle abundances, whereas solid lines represent gas-phase abundances. Fractional abundances, time, and temperature (upper axis) are plotted logarithmically.

Formic Acid

Two formation schemes generate formic acid in the warm-up phase (Figure 3). At ∼30 K it forms on grains according to the reaction

$$HCO_{(s)} + OH_{(s)} \rightarrow HCOOH_{(s)} \tag{2.5}$$

which was suggested by Allen & Robinson (1977). At around 40 K, the thermal desorption of grain-surface formaldehyde promotes rapid reaction with the radical OH through the reactions

$$H_2CO_{(g)} + OH_{(g)} \rightarrow HCOOH_{(g)} + H_{(g)} \tag{2.6a}$$

$$H_2CO_{(g)} + OH_{(g)} \rightarrow HCO_{(g)} + H_2O_{(g)} \tag{2.6b}$$

Reaction (2.6a) produces a spike in gas-phase formic acid abundance that is dissipated both by ion-molecule destruction mechanisms and by accretion of HCOOH back onto the grains; the high binding energy of formic acid then allows it to remain on the grains to high temperatures. The alternative branch, Reaction (2.6b), produces water and the HCO radical. The chemical network used in the model adopts a branching ratio for Reactions (2.6a) to (2.6b) of 1:50 (Yetter et al. 1989; DeMore et al. 1997), yet more recent studies suggest that the efficiency of Reaction (2.6a) may still be too high (Alvarez-Idaboy et al. 2001; Ocaña et al. 2017; Zanchet et al. 2018; see section 4).

The production of formic acid through the above reactions increases with greater ζ values. The total rate of Reaction (2.5) increases with ζ as elevated CRPD of formaldehyde and water ices produces more $HCO_{(s)}$ and $OH_{(s)}$ respectively. Production through Reaction (2.6a) increases with ζ as the higher rate of CR-induced dissociation of water produces more $OH_{(s)}$, some of which which desorbs into the gas. Combined, these reactions contribute to larger abundances of solid-phase HCOOH at 30–40 K for $\zeta = \zeta_9$ (Figure 2.3 panels $t_1\zeta_9$, $t_5\zeta_9$, $t_9\zeta_9$). However, at temperatures above 50 K, H abstraction by $OH_{(s)}$, which is the dominant destruction pathway on grains, destroys much formic acid for large t_{wu} and ζ (panels $t_5\zeta_9$, $t_9\zeta_5$, $t_9\zeta_9$). Consequently, abundances are diminished at high temperatures, and the large grain abundances at 40 K do not translate to large gas abundances later in the warm-up.

Formic acid thermally desorbs at around 120 K, and its gas abundances are mostly static for small t_{wu}, and for small ζ until 400 K (Figure 2.3, panels $t_1\zeta_1$, $t_1\zeta_5$, $t_1\zeta_9$, $t_5\zeta_1$, $t_9\zeta_1$). For other conditions, especially those of large t_{wu} and ζ (panel $t_9\zeta_9$), gas-phase formic acid is strongly destroyed by protonation with ${H_3O_{(g)}}^+$, which leads to diminished abundances.

The largest peak solid-phase abundances are about 3×10^{-7}, and occur for $t_{wu} = t_9$ and $\zeta = \zeta_5$ (Figure 2.3, panel $t_9\zeta_5$). For these conditions, Reactions (2.5) and (2.6a) are efficient and have much time to produce formic acid on grains. Largest peak gas abundances are about 8×10^{-8}, and occur for $t_{wu} = t_5$ and $\zeta = \zeta_5$ (panel $t_5\zeta_5$). Smallest peak grain abundances are about 1×10^{-9}, and occur for $t_{wu} = t_1$ and $\zeta = \zeta_1$ (panel $t_1\zeta_1$) owing to the low influence of Reactions (2.5) and (2.6a) and a brief period of formation. Smallest peak gas abundances are about 1×10^{-11}, and occur for $t_{wu} = t_9$ and $\zeta = \zeta_9$ (panel $t_9\zeta_9$) owing to the high influence of protonation with ${H_3O_{(g)}}^+$.

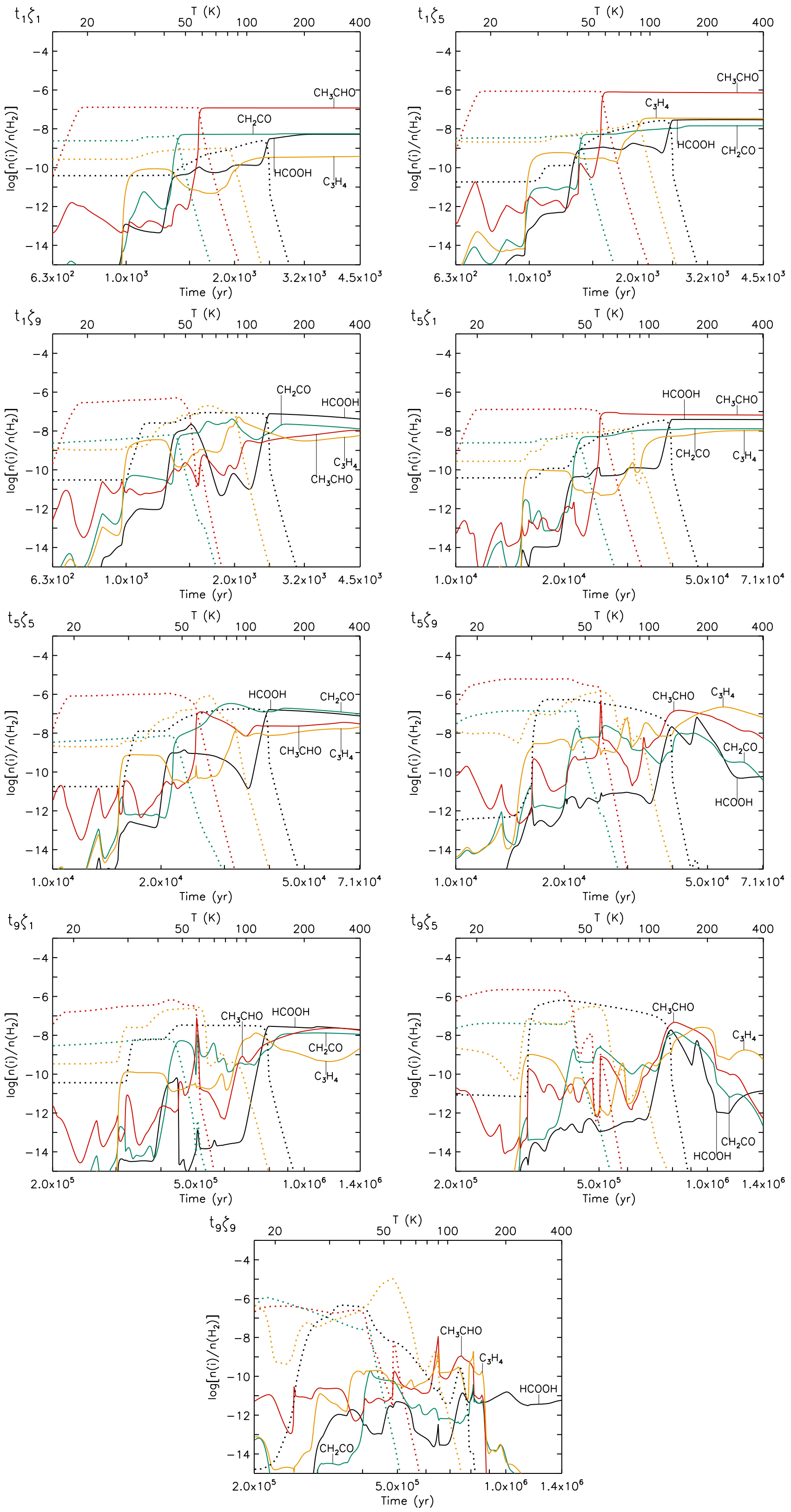

Figure 2.3: Select time and temperature-dependent fractional abundance plots (with respect to H_2) for formic acid (black), acetaldehyde (red), ketene (green), and C_3H_4 (yellow). Dotted lines represent the sum of grain-surface and ice-mantle abundances, whereas solid lines represent gas-phase abundances. Fractional abundances, time, and temperature (upper axis) are plotted logarithmically.

Acetaldehyde

Acetaldehyde (CH_3CHO) production on grains during the warm-up phase starts to increase significantly beyond temperatures of around 12 K, peaking at ~20 K (see Figure 2.3), through the reaction

$$\mathrm{CH_{3(s)} + HCO_{(s)} \rightarrow CH_3CHO_{(s)}} \tag{2.7}$$

as well as through hydrogenation of $\mathrm{CH_2CHO_{(s)}}$. The production rates for these reactions increase with ζ owing to greater production of the reactants, producing larger solid-phase acetaldehyde abundances with increasing ζ for all but the largest t_{wu} (panels $t_1\zeta_9$, $t_5\zeta_9$). The solid-phase abundances are mostly static from 20 K until desorption for all but large t_{wu} and medium to large ζ (panels $t_9\zeta_5$, $t_9\zeta_9$). For these conditions, CRPD of acetaldehyde and H abstraction by $\mathrm{OH_{(s)}}$ and $\mathrm{NH_{2(s)}}$, to form radicals $\mathrm{CH_3CO_{(s)}}$, $\mathrm{CH_2CHO_{(s)}}$, $\mathrm{CH_{3(s)}}$, and $\mathrm{HCO_{(s)}}$, are efficient and diminish solid-phase acetaldehyde abundances at temperatures around 40 K.

Acetaldehyde desorbs at about 55 K, and its abundances remain static for small to medium t_{wu} and ζ until 400 K (Figure 2.3, panels $t_1\zeta_1$, $t_1\zeta_5$, $t_5\zeta_1$). For medium to large t_{wu} and small to medium ζ (panels $t_5\zeta_5$, $t_5\zeta_9$, $t_9\zeta_1$, $t_9\zeta_5$), gas abundances increase at ~100 K owing to the reaction

$$\mathrm{C_2H_{5(g)} + O_{(g)} \rightarrow CH_3CHO_{(g)} + H_{(g)}} \tag{2.8}$$

This reaction is efficient for larger t_{wu} owing to the extended period in which to form $\mathrm{C_2H_{5(g)}}$. This radical is produced on the grains, from the abstraction of hydrogen from ethane (C_2H_6) by the OH radical, or by the addition of a hydrogen atom to C_2H_4. The resultant $\mathrm{C_2H_{5(s)}}$ then desorbs into the gas phase. For all other conditions, $\mathrm{HCO_{(g)}}^+$ and $\mathrm{H_3O_{(g)}}^+$ protonate and destroy gas-phase acetaldehyde appreciably throughout the warm-up. This effect is most severe for $t_{wu} = t_9$ and $\zeta = \zeta_9$ (panel $t_9\zeta_9$).

The largest peak solid-phase abundances are $\sim 3 \times 10^{-6}$, and occur for $t_{wu} = t_5$ and $\zeta = \zeta_9$ (Figure 2.3, panel $t_5\zeta_9$). For these conditions, Reaction (2.7) and hydrogenation of $\mathrm{CH_2CHO_{(s)}}$ are very efficient, whereas CRPD and H abstraction reactions, while also efficient, do not have enough time to greatly diminish abundances. The largest peak gas-phase abundances are $\sim 4 \times 10^{-7}$, and occur for $t_{wu} = t_1$ and $\zeta = \zeta_5$ (panel $t_1\zeta_5$). The smallest peak solid-phase abundances are $\sim 6 \times 10^{-8}$ and occur for $t_{wu} = t_1$ and $\zeta = \zeta_1$ (panel $t_1\zeta_1$). The time period available to form acetaldehyde is very brief under these conditions. The smallest peak gas-phase abundances are $\sim 5 \times 10^{-9}$, and occur for $t_{wu} = t_9$ and $\zeta = \zeta_9$ (panel $t_9\zeta_9$) owing to the high influence of protonation reactions.

Ketene

Much ketene (CH_2CO) forms on grains during the collapse phase by successive hydrogenation of $\mathrm{C_2O_{(s)}}$ that originates in the gas phase, although some ketene also forms in the warm-up, via CRPD of $\mathrm{CH_2CHO_{(s)}}$ (Figure 2.3). $\mathrm{CH_2CHO_{(s)}}$ forms at low temperatures via the addition of $\mathrm{CH_{2(s)}}$ and $\mathrm{HCO_{(s)}}$ radicals, which are formed mostly from CRPD of methane and formaldehyde, respectively. This mechanism elevates solid-phase ketene abundances slightly throughout the warm-up phase up until desorption, for most model setups. However, for $t_{wu} = t_9$ and $\zeta = \zeta_9$ (panel

$t_9\zeta_9$), CRPD of ketene to $CH_{2(s)}$ and $CO_{(s)}$ diminishes abundances until desorption. This is the strongest grain-surface destruction mechanism, and it is more effective than formation reactions for these conditions, producing a net loss.

Ketene desorbs at ∼45 K, and its gas-phase abundances remain mostly static for small to medium t_{wu} and ζ until 400 K (Figure 2.3, panels $t_1\zeta_1$, $t_1\zeta_5$, $t_5\zeta_1$). In some models, ketene may be formed in appreciable quantities as a product of the dissociative electronic recombination of protonated dimethyl ether (at around 60–70 K), which elevates abundances particularly for panels $t_1\zeta_9$, and $t_5\zeta_5$. Ketene may also form late in the warm-up, starting at ∼130 K, as the product of electronic recombination of protonated acetic acid ($CH_3COOH_2{}^+$), which elevates abundances somewhat for models $t_5\zeta_9$, $t_9\zeta_1$, and $t_9\zeta_5$. Gas-phase abundances are otherwise diminished at medium to high t_{uw} and ζ (panels $t_5\zeta_9$, $t_9\zeta_5$, $t_9\zeta_9$) owing to protonation by $HCO_{(g)}{}^+$ and $H_3O_{(g)}{}^+$. However, the product branching ratios for neither of the above-mentioned dissociative recombination processes are well-constrained, so the gas-phase formation of ketene during the warm-up phase should be treated with some caution.

The largest peak solid-phase abundances are $\sim 6 \times 10^{-7}$, and occur for $t_{wu} = t_9$ and $\zeta = \zeta_9$ (Figure 2.3, panel $t_9\zeta_9$). The largest gas-phase abundances are $\sim 2\times10^{-7}$, and occur for $t_{wu} = t_5$, and $\zeta = \zeta_5$ (panel $t_5\zeta_5$). These intermediate models mark the conditions at which formation reactions are most efficient compared to destruction reactions. The smallest peak solid-phase abundances are $\sim 2 \times 10^{-9}$, and occur for $t_{wu} = t_1$ and $\zeta = \zeta_1$ (panel $t_1\zeta_1$). Here, formation reactions have low influence and the period of formation is brief. The smallest gas-phase abundances are $\sim 9\times10^{-11}$, and occur for $t_{wu} = t_9$ and $\zeta = \zeta_9$ owing to the high influence of destruction reactions.

Methyl acetylene

B07 observe methyl acetylene (CH_3CCH) in their survey; however, the chemical network used here does not explicitly distinguish it from the other stable linear structural isomer of formula C_3H_4, propadiene (CH_2CCH_2). In the description of the models, we will therefore refer simply to C_3H_4.

C_3H_4 is first formed appreciably in the gas phase at around 30 K and then accreted onto grains (Figure 2.3). At this temperature, methane reacts with $C^+{}_{(g)}$ and $H_3{}^+{}_{(g)}$, as well as with the products of these reactions, to form a variety of neutral and ionic hydrocarbons. Among them are $C_3H_5{}^+{}_{(g)}$ and $C_4H_5{}^+{}_{(g)}$, which recombine with electrons to form $C_3H_{4(g)}$. Some C_3H_4 also forms on grains at low temperatures via hydrogenation of related hydrocarbons. These formation reactions gradually build up the grain-surface abundances, until C_3H_4 eventually desorbs. The gas-phase reactions become more effective in producing C_3H_4 under conditions of greater ζ, since ionic abundances are larger, resulting in greater abundances on the grains for all t_{wu} (models $t_1\zeta_9$, $t_5\zeta_9$, $t_9\zeta_9$).

Following desorption of C_3H_4 at 80 K, there remain a few mechanisms by which it continues to be formed in the gas phase; the strongest of these include the electronic recombination of protonated propylene and protonated propanal. The production of C_3H_4 through these reactions increases with ζ, owing to the greater protonation rates of the precursor molecules by abundant molecular ions. As a result, these reactions elevate gas-phase C_3H_4 abundances at temperatures greater than 100 K for some models with medium to large ζ (Figure 2.3, panels $t_5\zeta_9$, $t_9\zeta_5$). As with ketene, the uncertainty in the dissociation products of large molecular ions means that the higher-temperature gas-phase production routes should be viewed with some caution. Despite the influence of these reactions, gas-phase abundances of C_3H_4 are generally diminished for large t_{wu} and ζ (panel $t_9\zeta_9$) owing to protonation by $H_3O_{(g)}{}^+$.

The largest peak grain abundances are $\sim 5 \times 10^{-6}$, and occur for models with $t_{wu} = t_9$ and $\zeta = \zeta_9$ (Figure 2.3, panel $t_9\zeta_9$) since the low-temperature formation reactions are efficient and have a long time to form C_3H_4. The largest peak gas-phase abundances are $\sim 1 \times 10^{-7}$, and occur for $t_{wu} = t_5$ and $\zeta = \zeta_9$ (panel $t_5\zeta_9$). In this case, all formation reactions are much more effective than the gas-phase destruction reaction. The smallest peak grain and gas-phase abundances are $\sim 5 \times 10^{-10}$ and $\sim 2 \times 10^{-10}$ respectively, and occur for $t_{wu} = t_1$ and $\zeta = \zeta_1$ (panel $t_1\zeta_1$), under which conditions the formation reactions are inefficient and the formation time is brief.

Dimethyl Ether

Dimethyl ether (CH_3OCH_3) begins to form on grains early in the warm-up stage, peaking at around 20 K (see Figure 2.2), through the reaction

$$CH_3O_{(s)} + CH_{3(s)} \rightarrow CH_3OCH_{3(s)} \tag{2.9}$$

This reaction is more effective at higher ζ values, as the reactants are formed from CRPD of methanol. Consequently, grain-surface abundances increase with ζ, particularly for small and medium t_{wu} (panels $t_1\zeta_1$, $t_1\zeta_5$, $t_1\zeta_9$, $t_5\zeta_1$, $t_5\zeta_5$, $t_5\zeta_9$). After formation, grain abundances remain static for most conditions until desorption. However, for $t_{wu} = t_9$ and $\zeta = \zeta_9$ (panel $t_9\zeta_9$), CRPD diminishes abundances at temperatures greater than 30 K. Although this is not the only destruction reaction on grains, it is the strongest.

Dimethyl ether desorbs at 70 K, and its gas abundances remain static for small t_{wu} and small to medium ζ until 400 K (Figure 2.2, panels $t_1\zeta_1$, $t_1\zeta_5$). Dimethyl ether can also form in the gas phase from methanol, via Reaction 2.3 followed by dissociative electronic recombination of $CH_3OCH_4{}^+{}_{(g)}$. This scheme leads to a gas-phase peak at ~110 K for certain conditions (models $t_1\zeta_9$, $t_5\zeta_5$, $t_5\zeta_9$, $t_9\zeta_1$, $t_9\zeta_5$). Although the efficiency of this dissociative recombination in producing dimethyl ether is likely very low (Hamberg et al. 2010), a large abundance of gas-phase methanol, derived from the grains, can make it very effective. Dimethyl ether is destroyed in the gas phase via protonation by $HCO_{(g)}{}^+$ and $H_3O_{(g)}{}^+$ (again, followed by dissociative recombination), which diminishes abundances particularly for large t_{wu} and ζ (panel $t_9\zeta_9$).

The largest peak grain-surface abundances of dimethyl ether are $\sim 4 \times 10^{-7}$, and occur for $t_{wu} = t_5$ and $\zeta = \zeta_9$ (Figure 2.2, panel $t_5\zeta_9$) owing to the high influence of Reaction (2.9). Largest peak gas abundances are about 1×10^{-7}, and occur for $t_{wu} = t_9$ and $\zeta = \zeta_1$ (panel $t_9\zeta_1$) owing to the high influence of Reaction (2.3). The smallest peak grain-surface abundances are $\sim 6 \times 10^{-9}$, and occur for $t_{wu} = t_9$ and $\zeta = \zeta_1$. The smallest peak gas-phase abundances are $\sim 8 \times 10^{-15}$, and occur for model $t_9\zeta_9$, owing to rapid grain-surface and gas-phase destruction reactions.

Methyl Formate

Methyl formate forms on grains during the warm-up from 15 to 25 K (Figure 2.2) via the reaction

$$CH_3O_{(s)} + HCO_{(s)} \rightarrow CH_3OCHO_{(s)} \tag{2.10}$$

Grain abundances remain static thereafter until desorption for most models. However, for large t_{wu} and ζ (panel $t_9\zeta_9$) abundances are diminished at temperatures greater than 40 K, primarily due to H-abstraction reactions. Methyl formate is first destroyed at about 40 K owing to H abstraction by $OH_{(s)}$ to form $CH_3OCO_{(s)}$ and water. Some of the $CH_3OCO_{(s)}$ produced rehydrogenates to methyl formate, though the rate of methyl formate destruction typically exceeds the rate of reformation by a factor of several. Beginning at 60 K, H abstraction by $NH_{2(s)}$ becomes the strongest destruction pathway, again with some rehydrogenation to methyl formate.

Methyl formate desorbs at about 100–110 K, and its gas abundances remain mostly static for small t_{wu} and ζ (Figure 2.2, panels $t_1\zeta_1$, $t_1\zeta_5$, $t_1\zeta_9$, $t_5\zeta_1$, $t_9\zeta_1$) until 400 K. However, for all other models, gas-phase methyl formate is destroyed appreciably by protonation with ${HCO_{(g)}}^+$ and ${H_3O_{(g)}}^+$. The rate of destruction is especially high for large ζ, and diminishes abundances most dramatically for large $_{wu}$ (panel $t_9\zeta_9$).

The largest peak solid-phase abundances are $\sim 4 \times 10^{-7}$, and occur for $t_{wu} = t_1$ and $\zeta = \zeta_5$ (Figure 2.2, panel $t_1\zeta_5$) owing to the high influence of Reaction (2.10) and low the influence of H abstraction reactions. The largest peak gas-phase abundances are $\sim 2 \times 10^{-7}$, and occur for $t_{wu} = t_5$ and $\zeta = \zeta_5$ (panel $t_5\zeta_5$) also owing to the high influence of Reaction (2.10) and low influence of H abstraction reactions. The smallest peak grain-surface and gas-phase abundances are $\sim 3 \times 10^{-7}$ and 4×10^{-14} respectively, and occur for $t_{wu} = t_9$ and $\zeta = \zeta_9$ (panel $t_9\zeta_9$), since both the H-abstraction reactions on grains and the protonation reactions in the gas phase are most efficient.

Ethanol

B07 suggest that ethanol (C_2H_5OH) may be formed on grains by hydrogenation of ketene and acetaldehyde, though we lack these pathways in our network. In the present models (see Figure 2.2), ethanol forms on grains during the warm-up between 13 and 20 K, via the reaction

$$CH_{3(s)} + CH_2OH_{(s)} \rightarrow CH_3CH_2OH_{(s)} \tag{2.11}$$

At 40 K, ethanol is also formed on grains via

$$CH_3CH_{2(s)} + OH_{(s)} \rightarrow CH_3CH_2OH_{(s)} \tag{2.12}$$

The rates of these reactions increase with ζ, and produce larger grain abundances for all t_{wu} (panels $t_1\zeta_9$, $t_5\zeta_9$, $t_9\zeta_9$). Reaction (2.11) is particularly efficient for large timescales, as there is adequate time to form $CH_3CH_{2(s)}$, which mostly originates from the hydrogenation of $C_2H_{(s)}$. Consequently, a large solid-phase abundance peak occurs from 40 to 60 K for $t_{wu} = t_9$ and $\zeta = \zeta_9$ (panel $t_9\zeta_9$). Solid-phase abundances are static until desorption for most models; however, for large t_{wu} and ζ (panel $t_9\zeta_9$), ethanol abundances on the grains are diminished at temperatures greater than 60 K, primarily due to H abstraction by $OH_{(s)}$ to form $C_2H_5O_{(s)}$ and water ice.

Ethanol desorbs at 110 K, and its gas-phase abundances remain mostly static for small t_{wu} and ζ (Figure 2.2, panels $t_1\zeta_1$, $t_1\zeta_5$, $t_1\zeta_9$, $t_5\zeta_1$, $t_9\zeta_1$) until 400 K. For other conditions, it is destroyed efficiently via protonation by ${H_3O_{(g)}}^+$, which diminishes gas-phase ethanol abundances. This effect is pronounced for large t_{wu} and ζ (panel $t_9\zeta_9$).

The largest peak solid-phase abundances are $\sim 5 \times 10^{-6}$, and occur for $t_{wu} = t_9$ and $\zeta = \zeta_9$ (Figure 2, panel $t_9\zeta_9$) owing to the high influence of Reaction (2.11), and especially Reaction (2.12). The largest peak gas-phase abundances are $\sim 2 \times 10^{-7}$, and occur for $t_{wu} = t_1$ and $\zeta = \zeta_5$ (panel $t_1\zeta_5$). For these conditions, the influence of protonation by ${H_3O_{(g)}}^+$ is low, which allows for a large gas-phase peak. The smallest peak grain-surface abundances are $\sim 3 \times 10^{-8}$, and occur for $t_{wu} = t_1$ and $\zeta = \zeta_1$ (panel $t_1\zeta_1$). The smallest peak gas-phase abundances are $\sim 2 \times 10^{-13}$, and occur for $t_{wu} = t_9$ and $\zeta = \zeta_9$, due to the high influence of protonation by ${H_3O_{(g)}}^+$.

Formamide

Formamide (NH_2CHO) forms on the grains at temperatures around 20–30 K (see Figure 2.4) via the reaction

$$NH_{2(s)} + HCO_{(s)} \longrightarrow NH_2CHO_{(s)} \tag{2.13}$$

Grain abundances are static thereafter until desorption, for most models. However, for medium to large t_{wu} and ζ (panels $t_5\zeta_9$, $t_9\zeta_5$, $t_9\zeta_9$), formamide is destroyed at temperatures greater than 60 K, primarily due to H abstraction by $NH_{2(s)}$ to form $NH_2CO_{(s)}$ and ammonia. Some $NH_2CO_{(s)}$ rehydrogenates to formamide, though the reformation rate is up to one order of magnitude smaller than the H abstraction rate. Consequently, solid-phase abundances are diminished for these conditions.

Formamide desorbs at 110 K and remains static in the gas phase for small to medium t_{wu} and ζ (Figure 2.4, panels $t_1\zeta_1$, $t_1\zeta_5$, $t_5\zeta_1$) until 400 K. It is efficiently destroyed in the gas phase for all other conditions via protonation by ${H_3O_{(g)}}^+$. This reaction diminishes gas-phase abundances, especially for large t_{wu} and ζ (panel $t_9\zeta_9$).

The largest peak solid- and gas-phase abundances are both $\sim 1 \times 10^{-6}$, and occur for $t_{wu} = t_1$ and $\zeta = \zeta_5$ (Figure 2.4, panel $t_1\zeta_5$) owing to the low influence of destruction reactions. The smallest peak solid- and gas-phase abundances are $\sim 8 \times 10^{-8}$ and $\sim 3 \times 10^{-13}$, respectively, and occur for $t_{wu} = t_9$ and $\zeta = \zeta_9$ (panel $t_9\zeta_9$).

It may be noted that the chemical network does not include the reaction between NH_2 and formaldehyde that has been suggested as a possible gas-phase formation mechanism for formamide (Barone et al. 2015). Production of formamide through Reaction (2.13) in the present model appears more than sufficient to reproduce observational abundances (see later sections). The efficiency of the reaction is also subject to some doubt (Song & Kästner 2016).

Isocyanic Acid

Isocyanic acid (HNCO) forms on grains during the collapse and warm-up phases by the hydrogenation of $OCN_{(s)}$ (Figure 2.4). This process becomes more efficient with increasing ζ, due to increased abundances of $OCN_{(s)}$, which forms in the gas phase through ion-molecule reactions involving $HCN_{(g)}$. Hydrogenation of OCN

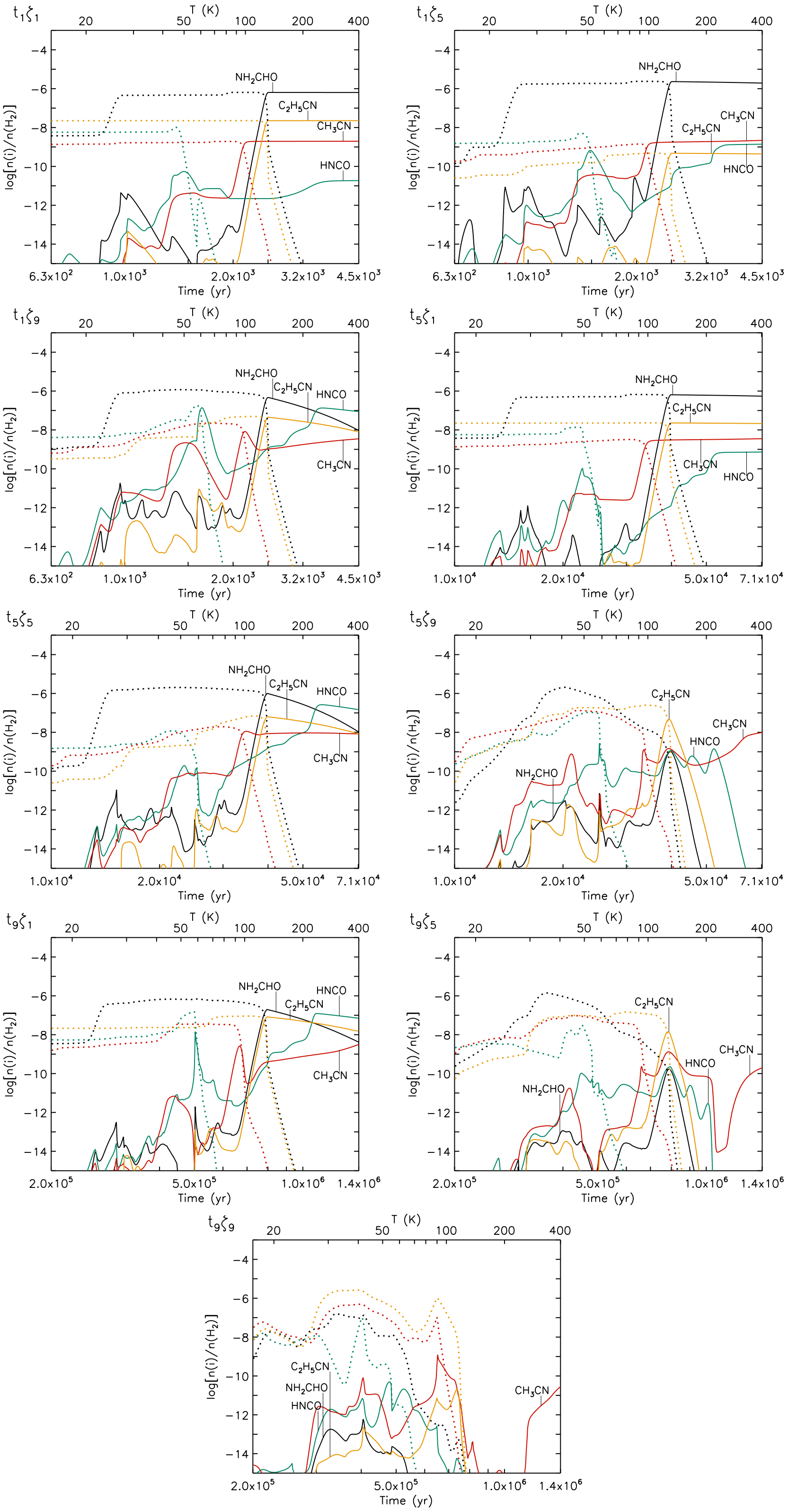

Figure 2.4: Select time- and temperature-dependent fractional abundance plots (with respect to H_2) for formamide (black), methyl cyanide (red), isocyanic acid (green), and ethyl cyanide (yellow). Dotted lines represent the sum of grain-surface and ice-mantle abundances, whereas solid lines represent gas-phase abundances. Fractional abundances, time, and temperature (upper axis) are plotted logarithmically.

elevates solid-phase abundances of isocyanic acid over the temperature range 15–60 K, especially for some large-ζ models (panels $t_1\zeta_9$, $t_5\zeta_9$).

Isocyanic acid desorbs at about 60 K, and its gas-phase abundances tend to increase in the temperature range of 100–400 K for most models (see Figure 2.4). Several reactions contribute to the increase, most importantly one of the branches for the dissociative electronic recombination of protonated urea, in line with other studies (Garrod et al. 2008; Tideswell et al. 2010). Formation of HNCO through this mechanism becomes more important with increasing ζ, since there are more ions to protonate urea ($NH_2CONH_{2(g)}$). As a result, isocyanic acid gas-phase abundances tend to increase with ζ for small t_{wu}, and somewhat for medium t_{wu} (panels $t_1\zeta_1$, $t_1\zeta_5$, $t_1\zeta_9$, $t_5\zeta_1$, $t_5\zeta_5$). Gas-phase production of HNCO also increases with greater t_{wu} (panels $t_1\zeta_1$, $t_5\zeta_1$, $t_9\zeta_1$, $t_5\zeta_1$, $t_5\zeta_5$). However, as t_{wu} and ζ increase, protonation by $HCO_{(g)}{}^+$ and $H_3O_{(g)}{}^+$ becomes efficient and diminishes gas abundances (panels $t_5\zeta_9$, $t_9\zeta_5$, $t_9\zeta_9$).

The largest peak solid-phase abundances are $\sim 9 \times 10^{-8}$, and occur for $t_{wu} = t_1$ and $\zeta = \zeta_9$ (Figure 2.4, panel $t_1\zeta_9$). The largest peak gas-phase abundances are $\sim 6 \times 10^{-8}$, and occur for $t_{wu} = t_9$, and $\zeta = \zeta_1$ (panel $t_9\zeta_1$). The smallest peak grain abundances are $\sim 3 \times 10^{-9}$, and occur for $t_{wu} = t_1$ and $\zeta = \zeta_5$ (panel $t_1\zeta_9$). The smallest peak gas-phase abundances are about 3×10^{-11}, and occur for $t_{wu} = t_9$ and $\zeta = \zeta_9$ (panel $t_9\zeta_9$) owing to the high influence of protonation reactions.

Methyl Cyanide

Methyl cyanide (CH_3CN) forms on grains during the collapse and warm-up by hydrogenation of $CH_2CN_{(s)}$ and less hydrogenated forms of $C_2N_{(s)}$, as well as through the radical-radical addition reaction

$$CH_{3(s)} + CN_{(s)} \rightarrow CH_3CN_{(s)} \tag{2.14}$$

as seen in Figure 2.4. These reactions are more effective for greater values of ζ, due to larger abundances of reactants, producing increased solid-phase CH_3CN abundances that are greatest for the largest ζ models (panels $t_1\zeta_9$, $t_5\zeta_9$, $t_9\zeta_9$). Conversely, for small ζ models, grain abundances are mostly static until desorption (models $t_1\zeta_1$, $t_5\zeta_1$, $t_9\zeta_1$).

Once methyl cyanide desorbs at about 85 K, its gas abundances remain static for models with small to medium t_{wu} and ζ (Figure 2.4, panels $t_1\zeta_1$, $t_1\zeta_5$, $t_5\zeta_1$, $t_5\zeta_5$) until 400 K. For models with greater t_{wu} and ζ, methyl cyanide can be formed more efficiently in the gas phase at temperatures greater than ~100 K through the radiative association reaction between $CH_3{}^+{}_{(g)}$ and $HCN_{(g)}$ (Charnley et al. 1992), followed by dissociative electronic recombination of the resultant protonated methyl cyanide. Gas-phase abundances of methyl cyanide tend to increase toward the end of the warm-up as a result ($t_1\zeta_9$, $t_5\zeta_9$, $t_9\zeta_1$, $t_9\zeta_5$, $t_9\zeta_9$). Despite this reaction, gas-phase abundances are diminished overall for for large t_{wu} and ζ (panels $t_9\zeta_5$, $t_9\zeta_9$) owing to protonation by $HCO_{(g)}{}^+$ and $H_3O_{(g)}{}^+$.

The largest peak solid-phase abundances are $\sim 1 \times 10^{-7}$, and occur for $t_{wu} = t_9$ and $\zeta = \zeta_9$ (Figure 2.4, panel $t_9\zeta_9$). Largest peak gas abundances are $\sim 6 \times 10^{-9}$, and occur for $t_{wu} = t_5$ and $\zeta = \zeta_5$ (panel $t_5\zeta_5$). The smallest peak solid-phase abundances are $\sim 9 \times 10^{-10}$, and occur for $t_{wu} = t_1$ and $\zeta = \zeta_1$ (panel $t_1\zeta_1$) owing to the inefficiency of formation reactions and the brief period of formation. The smallest peak gas-phase abundances are $\sim 3 \times 10^{-10}$, and occur for $t_{wu} = t_9$ and $\zeta = \zeta_9$ owing to the high influence of protonation reactions.

Ethyl Cyanide

Ethyl cyanide (C_2H_5CN) forms on grains during the collapse stage, via successive hydrogenation of $C_3N_{(s)}$ (Figure 2.4). Destruction of solid-phase ethyl cyanide via CRPD, to form radicals $CH_3CH_{2(s)}$, $CH_{3(s)}$, $CN_{(s)}$, $CH_2CN_{(s)}$, $CH_3CHCN_{(s)}$, and $CH_2CH_2CN_{(s)}$, also gains in importance for models with greater ζ values. As a result, solid-phase abundances tend to be diminished for large ζ models compared to small ζ models at the beginning of the warm-up phase (panels $t_1\zeta_1$, $t_1\zeta_9$).

Solid-phase ethyl cyanide abundances remain static throughout the warm-up until desorption for small ζ (Figure 2.4 panels $t_1\zeta_1$, $t_5\zeta_1$, $t_9\zeta_1$). It can also be formed efficiently on grains during the warm-up phase for models with greater ζ values, via the reactions

$$CH_{3(s)} + CH_2CN_{(s)} \rightarrow CH_3CH_2CN_{(s)} \tag{2.15}$$

$$CH_3CH_{2(s)} + CN_{(s)} \rightarrow CH_3CH_2CN_{(s)} \tag{2.16}$$

These reactions are more effective with greater ζ, due to larger abundances of the reactants, which are formed primarily from CRPD of methanol, methane, and $HCN_{(s)}$. Accordingly, ethyl cyanide abundances gradually increase for medium to large ζ (models $t_1\zeta_9$, $t_5\zeta_5$, $t_5\zeta_9$, $t_9\zeta_5$, $t_9\zeta_9$).

Ethyl cyanide desorbs from the grains at ~110 K, and its gas-phase abundances remain mostly static for small t_{wu} (Figure 2.4, panels $t_1\zeta_1$, $t_1\zeta_5$, $t_1\zeta_9$) and small ζ (panels $t_5\zeta_1$, $t_9\zeta_1$) until 400 K. For all other conditions, it is destroyed efficiently via protonation by ${H_3O_{(g)}}^+$, leading to diminished gas-phase abundances, especially for large t_{wu} and ζ (panel $t_9\zeta_9$).

The largest peak solid-phase abundances are $\sim 1 \times 10^{-6}$, and occur for $t_{wu} = t_9$ and $\zeta = \zeta_9$ (Figure 4, panel $t_9\zeta_9$) owing to the high influence of Reactions (2.15) and (2.16). The largest peak gas-phase abundances are $\sim 4 \times 10^{-8}$, and occur for $t_{wu} = t_9$ and $\zeta = \zeta_1$ (panel $t_9\zeta_1$) owing to the low influence of the protonation reaction. The smallest peak solid-phase abundances are about 1×10^{-8}, and occur for $t_{wu} = t_1$ and $\zeta = \zeta_1$. The production rates of the reactants that form ethyl cyanide via Reactions (2.15) and (2.16) are small in this case, and the formation period is brief. The smallest peak gas-phase abundances are $\sim 1 \times 10^{-11}$, and achieved in the model with for $t_{wu} = t_9$ and $\zeta = \zeta_9$ owing to the high influence of the protonation reaction.

Glycine

Glycine (NH_2CH_2COOH), as yet undetected in an interstellar source, in these models forms on grains in the warm-up stage, via the reactions

$$NH_2CH_2CO_{(s)} + OH_{(s)} \rightarrow NH_2CH_2COOH_{(s)} \tag{2.17}$$

$$NH_{2(s)} + CH_2COOH_{(s)} \rightarrow NH_2CH_2COOH_{(s)} \tag{2.18}$$

as well as through hydrogenation of $NHCH_2COOH_{(s)}$ (Figure 2.5). The $NH_2CH_2CO_{(s)}$ radical (Reaction (2.17)) is formed primarily by H abstraction from glycinal (NH_2CH_2CHO). Glycinal itself is mostly formed by the reaction of $CH_{2(s)}$ and $NH_{2(s)}$, whose product, $CH_2NH_{2(s)}$, reacts with $HCO_{(s)}$. The $CH_2COOH_{(s)}$ radical of Reaction (2.18) mostly

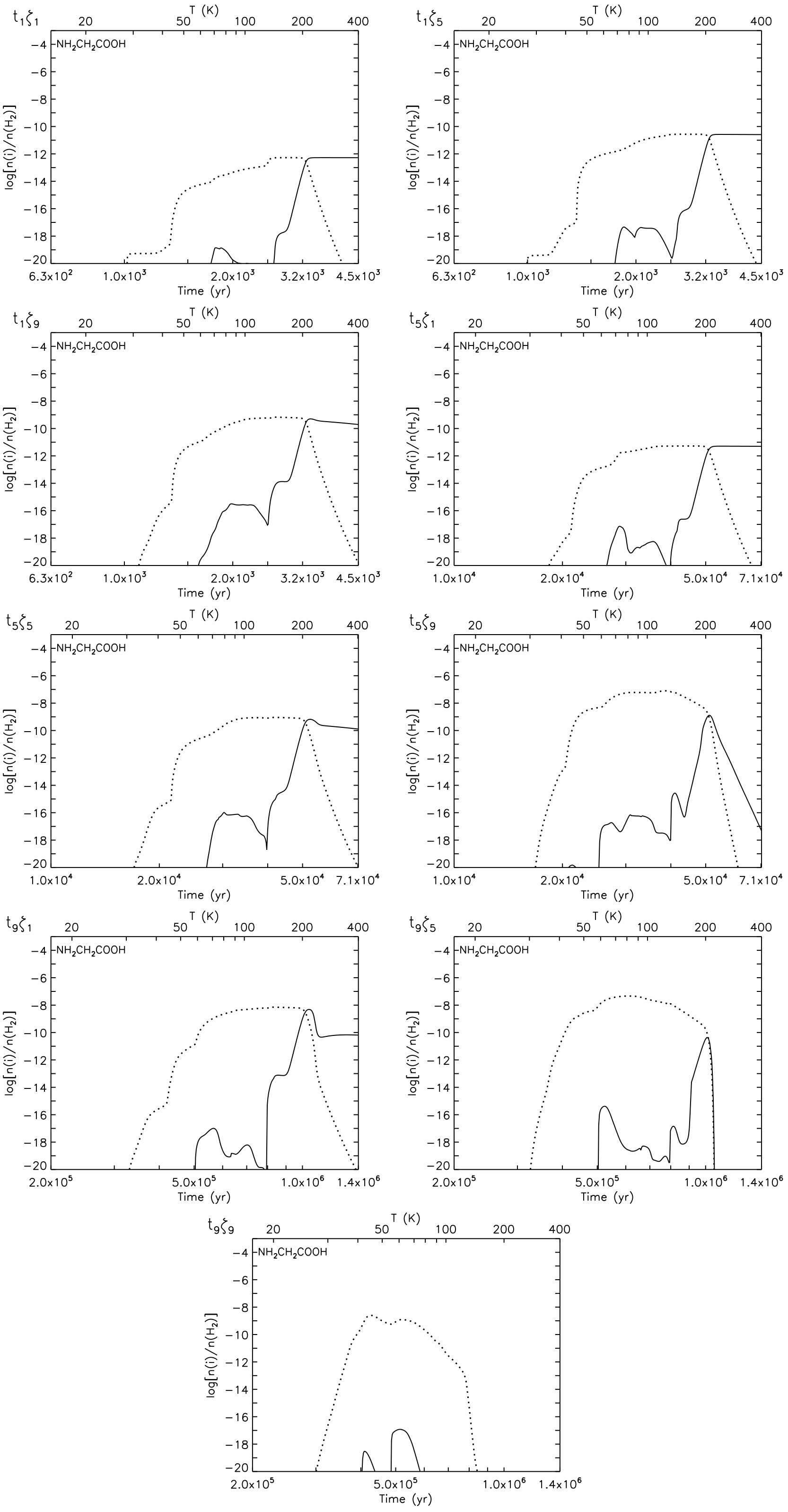

Figure 2.5: Select time- and temperature-dependent fractional abundance plots (with respect to H_2) for glycine. The dotted line represents the sum of grain-surface and ice-mantle abundances, whereas the solid line represents the gas-phase abundance. The fractional abundance, time, and temperature (upper axis) are plotted logarithmically.

forms from CRPD of acetic acid (CH_3COOH) and through the reaction of $CH_{2(s)}$ and $HOCO_{(s)}$. The $NHCH_2COOH_{(s)}$ radical forms mostly through the addition reaction of $NH_{(s)}$ with $CH_2COOH_{(s)}$, with $NH_{(s)}$ produced by CRPD of solid-phase ammonia.

The formation reactions on grains elevate solid-phase glycine abundances appreciably at ∼30 K (Figure 2.5). These reactions are more effective for models with greater ζ, as the reactants involved form from CRPD of primary ice constituents. Accordingly, grain abundances grow larger for large ζ compared to small ζ for most t_{wu} (models $t_1\zeta_1$, $t_1\zeta_9$, $t_5\zeta_9$). At large t_{wu} and ζ (panel $t_9\zeta_9$), however, solid-phase abundances are diminished by CRPD to form $NH_{2(s)}$ and $CH_2COOH_{(s)}$, and H abstraction by $OH_{(s)}$ and $NH_{2(s)}$ beginning at 40 and 60 K, respectively. In the $t_9\zeta_9$ model, glycine is completely destroyed on the grain surfaces prior to desorption.

Glycine desorbs at ∼200 K, and its gas-phase abundances remain static for small t_{wu} (Figure 2.5, panels $t_1\zeta_1$, $t_1\zeta_5$, $t_1\zeta_9$), and mostly static for small ζ (panels $t_5\zeta_1$, $t_9\zeta_1$). However, for all other conditions it is efficiently destroyed via protonation by $H_3O_{(g)}{}^+$, which leads to diminished gas-phase abundances, especially for large t_{wu} and ζ (panel $t_9\zeta_9$). A more extensive discussion of the grain and gas-phase glycine chemistry included in this network is given by G13.

The largest peak solid- and gas-phase abundances for glycine are $\sim 4 \times 10^{-8}$ and $\sim 7 \times 10^{-10}$ respectively, and occur for $t_{wu} = t_5$ and $\zeta = \zeta_9$ (Figure 2.5, panel $t_5\zeta_9$) owing to rapid production and the limited influence of grain and gas-phase destruction reactions. The smallest peak solid-phase abundances are $\sim 3 \times 10^{-13}$, and occur for $t_{wu} = t_1$ and $\zeta = \zeta_1$ (panel $t_1\zeta_1$). The smallest peak gas-phase abundances are about 6×10^{-18}, and occur for $t_{wu} = t_9$ and $\zeta = \zeta_9$ (panel $t_9\zeta_9$). For these conditions, solid-phase glycine is destroyed almost entirely prior to desorption, due to the high influence of CRPD and H-abstraction reactions.

2.3.2 Column Densities and Excitation Temperatures

In order to obtain abundance information that can be directly compared with observational data, modeled fractional abundance data from the grid are mapped onto the temperature and density profiles obtained for NGC 6334 IRS 1, NGC 7538 IRS 1, W3(H2O), and W33A by van der Tak et al. (2000). For each model in the grid, all molecular emission lines observed by B07 for the source in question are simulated using the radiative transfer model, including convolution with the appropriate telescope beam size for the line frequency and the instrument with which it was observed by B07. Integrated intensities for the resultant molecular line spectra are plotted in population diagrams to derive a value for N_{tot} and for T_{ex}, for each molecule, for all chemical models and sources. In order to replicate as precisely as possible the population diagram method carried out by B07, the line-integrated intensities plotted in the population diagrams are rescaled according to the size of the telescope beam at the line frequency (see B07 for details). The line emission is also corrected for optical depth effects, where appropriate, following the correction given by Herbst & van Dishoeck (2009). The radiative transfer calculations automatically provide the optical depth for each frequency channel.

As an example, population diagrams for ethanol are shown in Figure 2.6, for a selection of chemical models applied to source NGC 6334 IRS 1. N_{tot} generally parallels abundance trends; however, since it represents space-integrated number

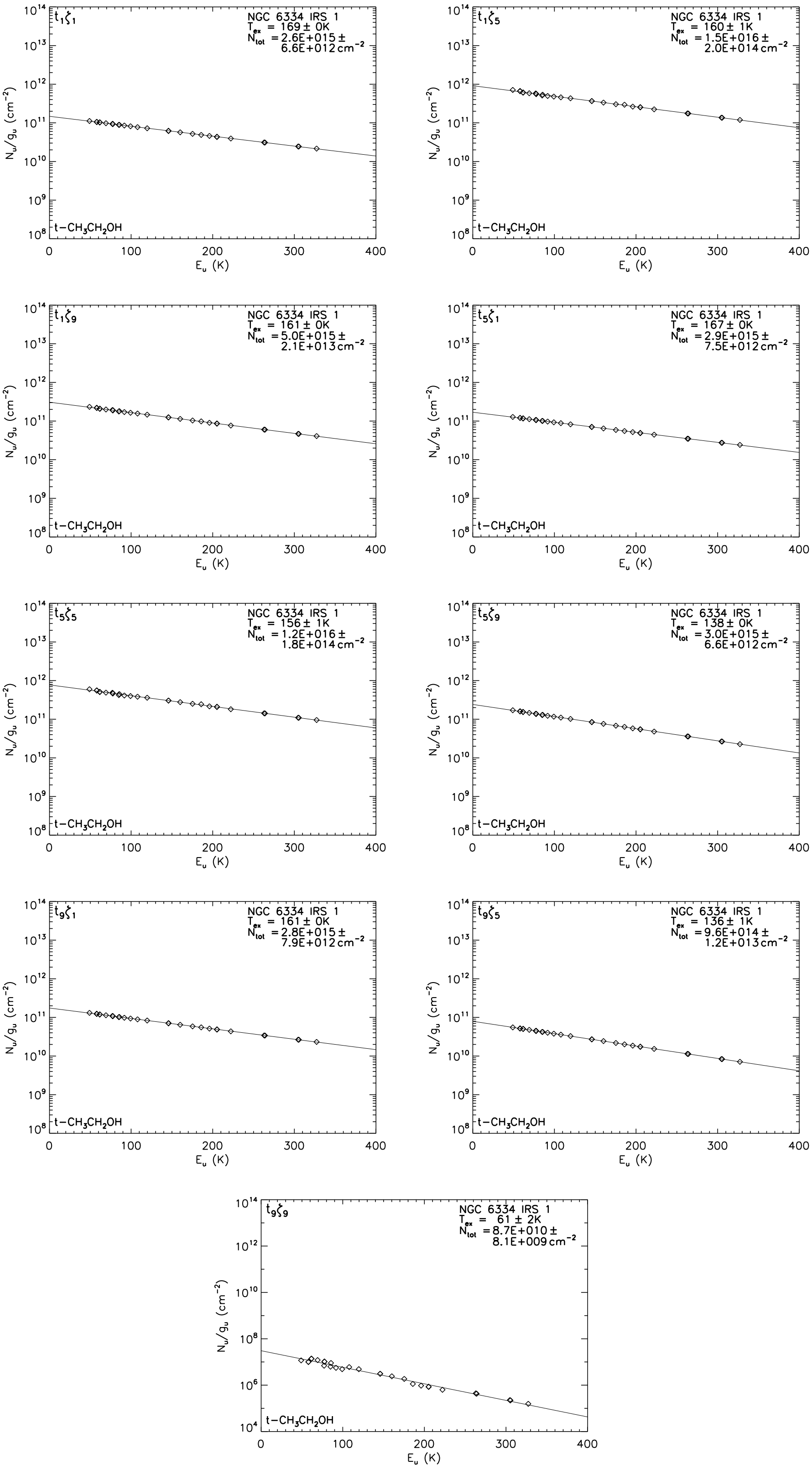

Figure 2.6: Select population diagrams of ethanol for source NGC 6334 IRS 1. Data points have been corrected for optical depth. Data points are not corrected for non-LTE emission.

densities, its value gives a more comprehensive representation of a molecule's abundance throughout the source as a whole. T_{ex} is indicative of temperatures at which peak fractional abundances occur and trends somewhat differently than integrated intensities and N_{tot}. The data are seen to be well represented by a single N_{tot} and T_{ex} value.

For most molecules, N_{tot} values increase from small to large ζ for small t_{wu} models and decrease from small to large ζ for large t_{wu} models. For example, N_{tot} of ethanol for source NGC 6334 IRS 1 increases from 8.7×10^{10} cm^{-2} to 2.8×10^{15} cm^{-2} from large to small ζ for $t_{wu} = t_9$ (Figure 2.6, panels $t_9\zeta_1$, $t_9\zeta_9$), and increases from 2.6×10^{15} cm^{-2} to 5.0×10^{15} cm^{-2} from small to large ζ for $t_{wu} = t_1$ (panels $t_1\zeta_1$, $t_1\zeta_9$). This trend is also apparent for other molecules including methyl formate and dimethyl ether. Figure 2.7 shows these trends for a selection of molecules in source NGC 6334 IRS 1; within each panel, the column density for a particular molecule is plotted for each model, starting with each cosmic-ray ionization model using $t_{wu} = t_1$, and finishing with the $t_{wu} = t_9$ models. The trend of increasing molecular column densities with increasing t_{wu} values continues to t_{wu} values around the $t_5 - t_4$ range, after which the trend reverses, as described above. However, the turnover in the trend varies somewhat depending on the molecule considered.

For most molecules, N_{tot} is also sensitive to t_{wu} changes. For instance, the N_{tot} values for methyl formate, ethanol, dimethyl ether, formic acid, and formamide increase significantly for small t_{wu}, for any single value of ζ. Figure 2.7 illustrates this trend for methyl formate and dimethyl ether. The N_{tot} values for a couple molecules including ketene and methyl cyanide tend to increase for medium t_{wu} (Figures 2.7(c)-(d)).

Trends in the excitation temperatures, T_{ex}, obtained from the population diagrams are less dependent on t_{wu}, but temperatures generally decrease for increasing ζ. Ethanol in source NGC 6334 IRS 1 (Figure 2.6) exemplifies this trend as its T_{ex} decreases from 169 to 161 K for $t_{wu} = t_1$, from 167 to 138 K for $t_{wu} = t_5$, and from 161 to 61 K for $t_{wu} = t_9$, with increasing ζ. Although several molecules do exhibit strong T_{ex} changes with different t_{wu} for a particular source, the behavior is mostly inconsistent between sources, and, in many cases, for low ζ values the excitation temperatures show little variation with t_{wu}. For example, T_{ex} of ethanol decreases for large t_{wu} for NGC 6334 IRS 1 and W33A but is essentially static across different t_{wu} for NGC 7538 IRS 1 and W3(H_2O) except for very high ζ. Figure 2.8 (panels (a) and (b)) highlights this inconsistency for ethanol in sources NGC 6334 IRS 1 and NGC 7538 IRS 1. Ketene and isocyanic acid are the only molecules having strong, consistent trends in T_{ex} with changing t_{wu}. The temperatures of these molecules are generally greatest at intermediate t_{wu} (Figures 2.8(c)-(d)). Aside from these exceptions, T_{ex} consistently decreases across the grid of models from small to large ζ.

2.4 Comparison with Observations

While it is possible to compare column densities and excitation temperatures obtained from the spectral models directly with those derived from observations for individual molecules, the determination of the overall best model to match the observations of all molecules toward a specific source, based on N_{tot} and T_{ex}, is more challenging. Instead, rather than lend the column density and excitation temper-

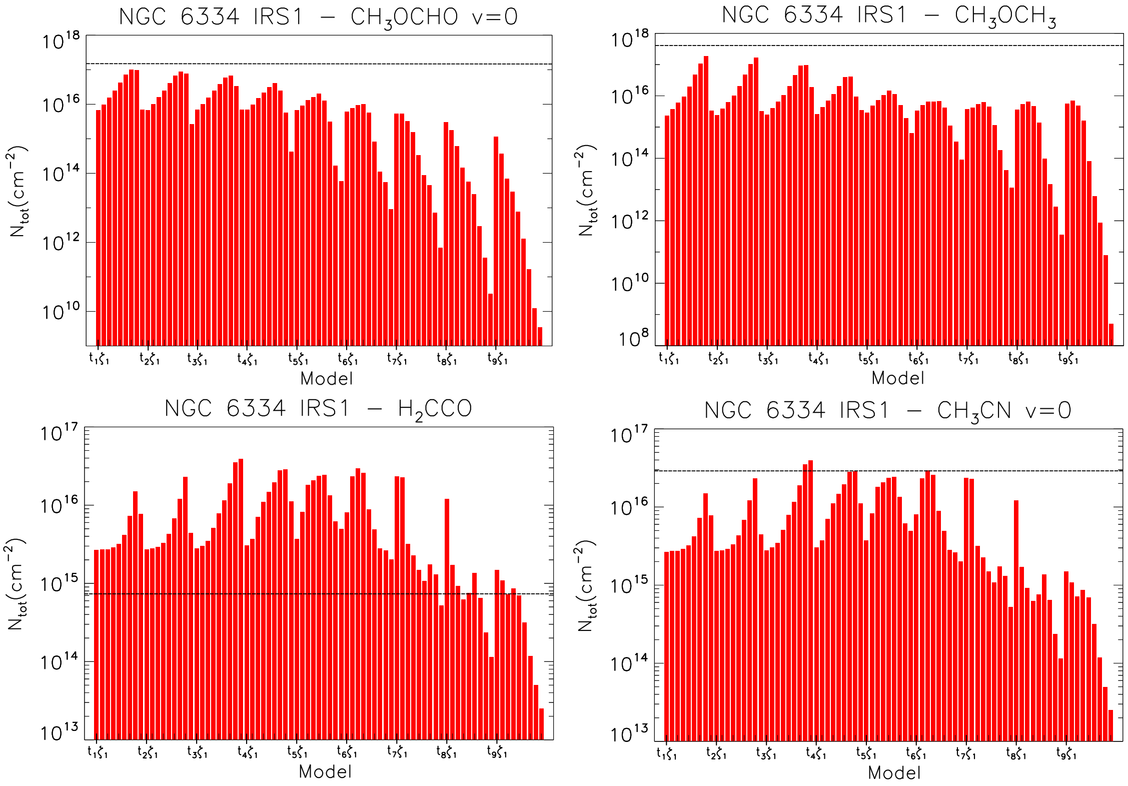

Figure 2.7: Source-averaged column densities (N_{tot}) for methyl formate (panel (a)), dimethyl ether (panel (b)), ketene (panel (c)), and methyl cyanide (panel (d)), obtained with each chemical model as applied to source NGC 6334 IRS 1. ζ increases from ζ_1 to ζ_9 going from left to right across the figure for each t_{wu}. The dashed lines in panels (a)-(d) correspond to the measured values $N_{tot} = 1.2 \times 10^{17}$ cm^{-2}, $N_{tot} = 5.8\times10^{17}$ cm^{-2}, $N_{tot} = 7.4\times10^{14}$ cm^{-2} and $N_{tot} = 2.9\times10^{16}$ cm^{-2} respectively (B07).

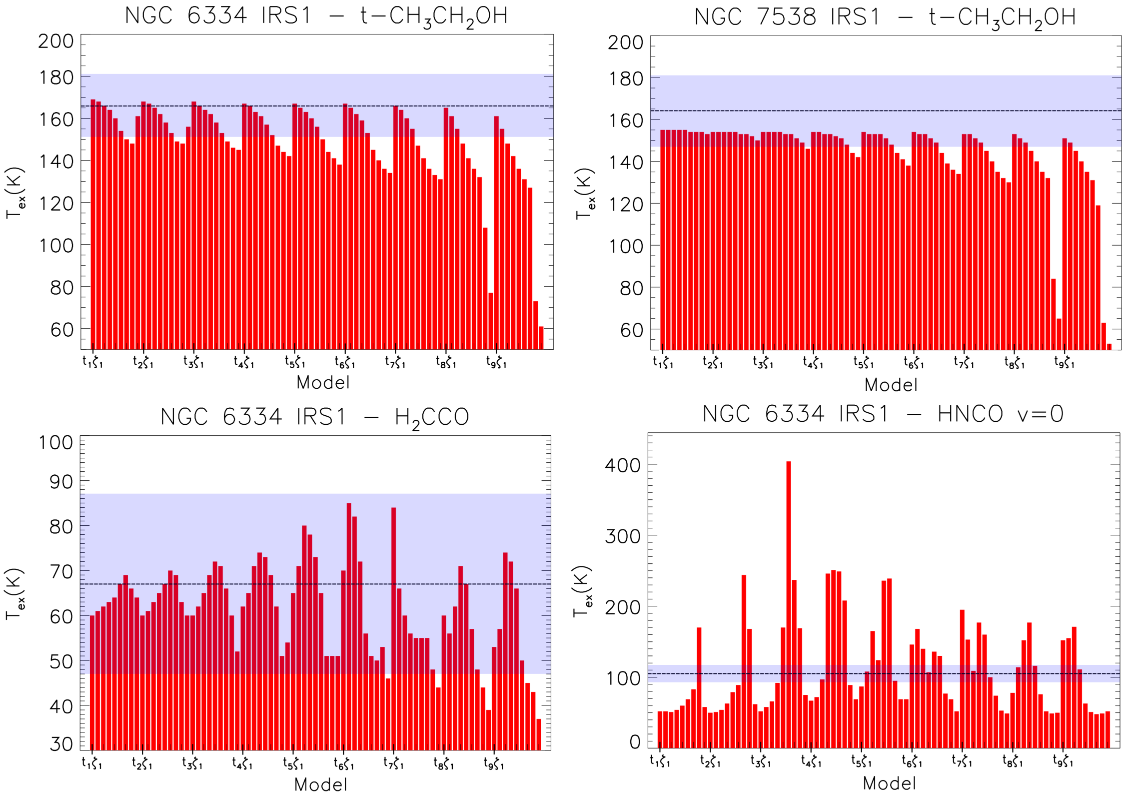

Figure 2.8: Excitation temperatures (T_{ex}) obtained with each chemical model for a selection of molecules and sources. Results are shown for ethanol in NGC 6334 IRS 1 (panel (a)), for ethanol in NGC 7538 IRS 1 (panel (b)), for ketene in NGC 6334 IRS 1 (panel (c)), and for isocyanic acid in NGC 6334 IRS 1 (panel (d)). The dashed lines and blue rectangles in panels (a)-(d) correspond to measured T_{ex} and uncertainties of $T_{ex} = 166 \pm 15$ K, $T_{ex} = 164 \pm 17$ K, $T_{ex} = 67 \pm 20$ K, and $T_{ex} = 105 \pm 12$ K, respectively (B07).

ature of each molecule some artificial weight, here we concentrate on how well the models reproduce each individual observed emission line, regardless of the molecule from which they derive. By obtaining a global best-fit parameter based on the matches between observational and modeled determinations of integrated line intensities, the best-fitting model for each source is obtained, allowing ζ and t_{wu} in turn to be constrained.

In this comparison of simulated integrated intensities with those observed by B07, we exclude several lines from the analysis that may adversely affect the fit. Observed transitions of excited states including those of gauche ethanol and higher vibrational levels are discarded because our chemical model computes ground-state fractional abundances only. Observed blended lines are discarded to best suit the pure spectrum treatment employed in the simulation. Integrated intensities for which upper limits are cited are also excluded to avoid uncertainty in the comparison. Finally, lines that are simulated to be optically thick are eliminated on the basis that their integrated intensities reflect only lower limits on true emission intensities and thus may skew the fit.

A few molecules observed by B07 are excluded from the analysis entirely, due to either poor or suspect model results (discussed below, in section 2.5.3). Formic acid is discarded because recent literature indicates that its gas-phase chemistry may be incorrect in our model (Alvarez-Idaboy et al. 2001; Ocaña et al. 2017; Zanchet et al. 2018). In particular, the 1:50 branching ratio of Reactions (2.6a) to (2.6b) is likely too high. Accordingly, formic acid abundances are overproduced by a few orders of magnitude in most models. Also, the modeled integrated intensities of formaldehyde compare poorly with the observed value for all sources. For example, the observed integrated intensity for the $3_{1,2} - 2_{2,1}$ transition is reported to be 57 K km s^{-1} for source NGC 6334 IRS 1; however, most models give a result that is greater than 500 K km s^{-1}. The modeled results for the other sources are also too high by a similar magnitude. Consequently, formaldehyde is excluded on the basis of a uniformly poor match. Formamide is also excluded, due to it being overproduced and having optically thick emission in the models. The results for these molecules indicate that their chemistry is incorrect in our models and are not therefore appropriate to compare with observations.

Having eliminated poor lines and molecules, we compare qualifying integrated intensity data with corresponding observed data using the confidence of agreement treatment introduced by Garrod et al. (2007), which was originally used by those authors to compare fractional abundances. In the present treatment, the confidence of agreement, κ_i, for a pair of simulated and observed integrated intensities, $I_i = \int T_{B,i}(\nu)d\nu$, for line i is defined using the complimentary error function:

$$\kappa_i = \frac{\mathrm{erfc}[|log_2(I_{\mathrm{i,mod}}) - log_2(I_{\mathrm{i,obs}})|]}{\sqrt{2}} \tag{2.19}$$

In this treatment, the value of κ_i ranges from 1 to 0, corresponding to a good or a poor match, respectively. The final matching parameter, κ, is simply the mean average of κ_i for all i lines observed for the source in question. Because the value of κ_i for an arbitrarily bad match approaches zero, this ensures that it does not unduly affect the overall match. Thus, this method rewards success but does not punish failure beyond some scale distance from the “true value.” This scale distance corresponds to the models diverging by a factor of two, up or down, as compared to the observed integrated intensity of the line. We choose log base-2 instead of base-10 to produce a tolerance that is more sensitive to small changes in the comparison.

Figures 2.9–2.12 illustrate the variation in the agreement parameter, κ, for each source, using each model in the grid. Red colors indicate a better match, while blue indicates a worse match. The same color scale is used to map κ in each plot, so that the quality of the match may be compared between sources. The height and width of each colored rectangle scale to the logarithmic spacing between models.

In order to constrain the ζ and t_{wu} values beyond the resolution of the main model grid, refined grids were created for each source using the best-fit model as the central value. Taking the original 3×3 subgrid of models surrounding the best-fit model, the resolution is doubled to generate a 5×5 fine grid featuring two additional timescales and values of ζ, corresponding to 16 new chemical models, each denoted with half-integer values for t and ζ. For example, $\mathrm{t}_{5.5}$ is the timescale corresponding to the logarithmic midpoint between t_5 and t_6. The new refined grid parameters are listed in Table 2.4. The confidence of agreement treatment is then reiterated for the fine grid to give a new best-fit model with improved resolution. The results of the analytical treatment for the four sources surveyed are summarized in the following subsection. The best-fit results and constraints on ζ and t_{wu} are summarized in Table 2.5.

Table 2.4: Fine Fluence Grid Parameters.

Warm-up Timescale		Cosmic-Ray Ionization Rate	
Notation	Time to Reach 200 K (yr)	Notation	ζ(s^{-1})
t_0	1.56×10^3	$\zeta_{3.5}$	1.84×10^{-17}
$t_{0.5}$	2.21×10^3	$\zeta_{4.5}$	3.68×10^{-17}
$t_{1.5}$	4.42×10^3	$\zeta_{5.5}$	7.35×10^{-17}
$t_{2.5}$	8.84×10^3	$\zeta_{6.5}$	1.47×10^{-16}
$t_{3.5}$	1.77×10^4	$\zeta_{7.5}$	2.94×10^{-16}
$t_{4.5}$	3.54×10^4	$\zeta_{8.5}$	5.88×10^{-16}

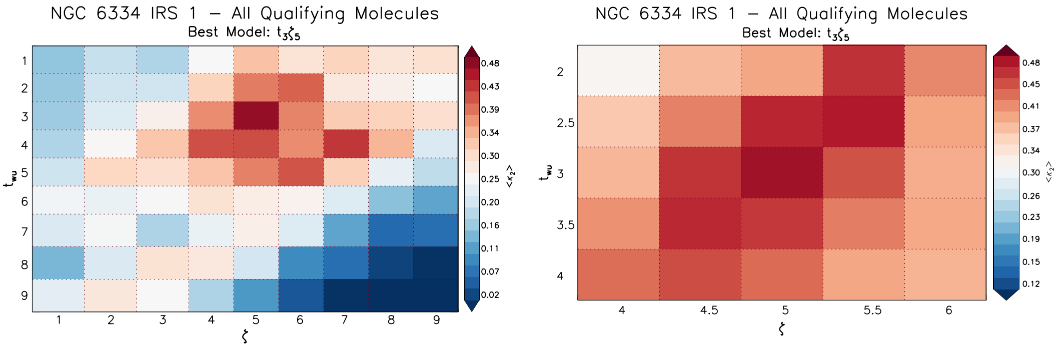

Figure 2.9: Comparison of modeled and observed integrated intensities for source NGC 6334 IRS 1 using the κ analysis. Higher (redder) values of κ indicate a better match. Formic acid, formamide, and formaldehyde are omitted from the analysis. Panel (a) features the results for all chemical models. Panel (b) features the results of fine grid models. The additional models in the fine grid are denoted as half-integer values of the original timescales and cosmic-ray ionization rates.

2.4.1 NGC 6334 IRS 1

Model comparisons for source NGC 6334 IRS 1 are presented in Figure 2.9. For the full grid (panel (a)), κ values are generally greater than 0.15 (an average agreement between modeled and observed integrated intensities within a factor of about 2), and the best agreement lies roughly in the upper middle with values greater than 0.30 (an average within a factor of about 1.7). For both the full and fine grid (panel (b)), the best fit occurs for model $t_3\zeta_5$, with $\kappa = 0.471$ (an average within a factor of about 1.4), and gives $\zeta = 5.20 \times 10^{-17}$ s^{-1}.

2.4.2 NGC 7538 IRS 1

Model comparison results for source NGC 7538 IRS 1 are presented in Figure 2.10. For the full grid (panel (a)), κ values are generally greater than 0.05 (an average within a factor of about 2.6), and the best agreement lies in the upper middle right with values greater than 0.23 (an average within a factor of about 1.8). The best-fit models of the full and fine grid (panel (b)) are $t_1\zeta_6$ ($\kappa = 0.334$) and $t_{1.5}\zeta_6$ ($\kappa = 0.337$), respectively (both an average within a factor of about 1.6). Using the fine grid result, $\zeta = 1.04 \times 10^{-16}$ s^{-1}.

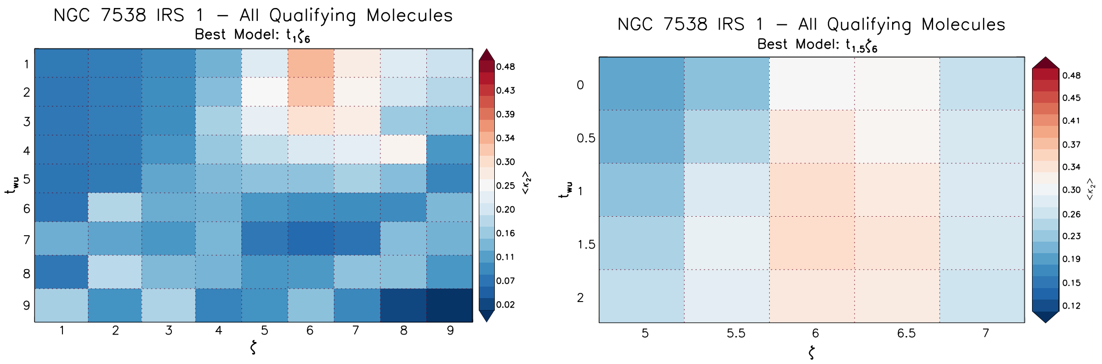

Figure 2.10: Comparison of modeled and observed integrated intensities for source NGC 7538 IRS 1. As per Figure 2.9.

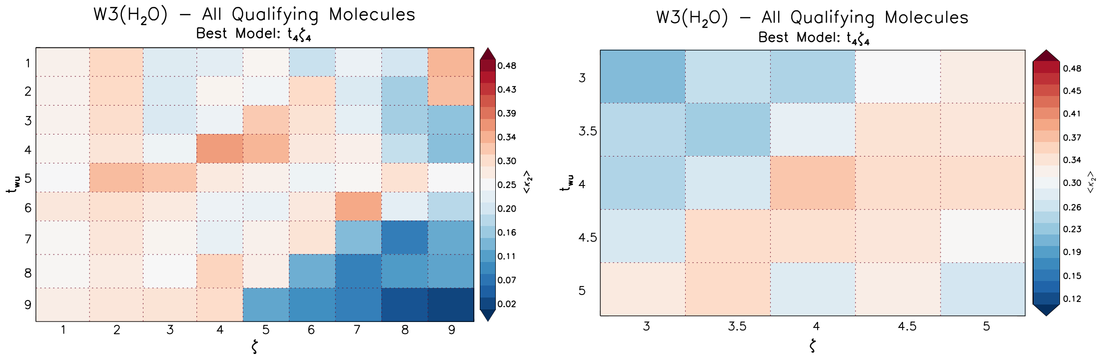

Figure 2.11: Comparison of modeled and observed integrated intensities for source W3(H_2O). As per Figure 2.9.

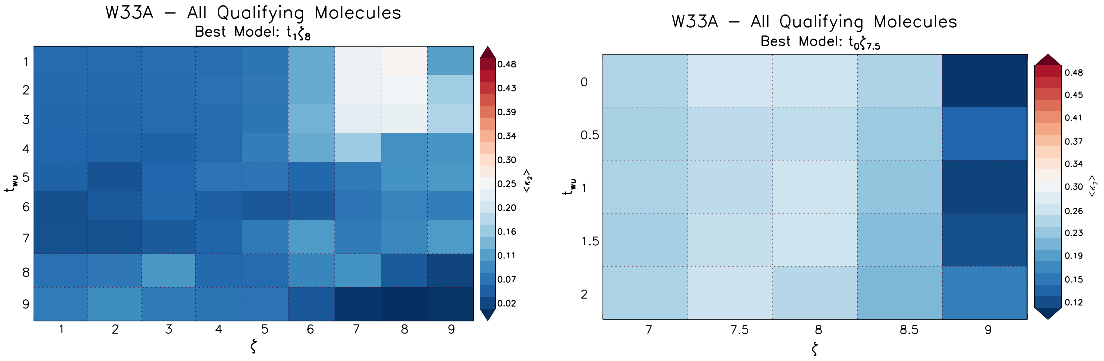

Figure 2.12: Comparison of modeled and observed integrated intensities for source W33A. As per Figure 2.9.

Table 2.5: Summary of Best-Fit Results.

Source	Best Model	κ	Fit to ζ (s^{-1})	Fit to t_{wu} (yr)
NGC 6334 IRS 1	$t_3\zeta_5$	0.471	5.20×10^{-17}	1.25×10^4
NGC 7538 IRS 1	$t_{1.5}\zeta_6$	0.337	1.04×10^{-16}	4.42×10^3
W3(H_2O)	$t_4\zeta_4$	0.357	2.60×10^{-17}	2.50×10^4
W33A	$t_0\zeta_{7.5}$	0.261	2.94×10^{-16}	1.56×10^3

2.4.3 W3(H_2O)

Model comparison results for source W3(H_2O) are presented in Figure 2.11. For the full grid (panel (a)), κ values are mostly greater than 0.15 (an average within a factor of about 2.0); however, there is no apparent region of the grid where the agreement converges to produce best results (discussed in Section 5.2). Nonetheless, there are a few points in parameter space that give good matches. For both the full and fine grid (panel (b)), the best fit occurs for model $t_4\zeta_4$, with $\kappa = 0.357$ (an average within a factor of about 1.6), and gives $\zeta = 2.60 \times 10^{-17}$ s^{-1}.

2.4.4 W33A

Model comparison results for source W33A are presented in Figure 2.12. For the full grid (panel (a)), κ values are low across most of the grid, as they do not exceed 0.10 (an average within a factor of about 2.2) for the majority of the models. There is, however, a well-defined region of best fit in the upper right corner with κ values greater than 0.20 (an average within a factor of about 1.9). The best-fit models of the full and fine grid (panel (b)) are $t_1\zeta_8$ ($\kappa = 0.259$) and $t_0\zeta_{7.5}$ ($\kappa = 0.261$), respectively (both an average within a factor of about 1.7). Using the fine grid result, $\zeta = 2.94 \times 10^{-16}$ s^{-1}.

2.5 Discussion

The models presented here consider the dependence of COM chemistry in hot cores on the complementary parameters of cosmic-ray ionization rate and warm-up timescale. A large proportion of the parameter space appears to provide a potentially acceptable set of results to match observed COM abundances, although the models with the highest nominal cosmic-ray fluence (i.e. the product of ζ and t_{wu}) demonstrate a catastrophic destruction of gas-phase molecules, in spite of significant COM production on the dust grains.

The general behavior shown by the models is that, with increasing ζ, CRPD of major ice constituents generates more radicals, which react to produce greater abundances of COMs in ice mantles, while large t_{wu} lead to diminished abundances. Although formation reactions tend to elevate abundances, they are only effective for a small fraction of a molecule's lifetime in the ice, prior to desorption. At temperatures above about 40 K, destruction by H abstraction and CRPD mechanisms predominates. As ζ increases, abundances are larger for small t_{wu} (Figures 2.2-2.5), somewhat smaller for medium t_{wu}, and considerably smaller for large t_{wu} at the time of desorption. In the models with the smallest ζ values, variation of t_{wu} has little effect on COM abundances.

Most COMs considered in this study are first formed on grains and then desorb at a characteristic temperature. Therefore, higher ice abundances correspond to larger gas-phase peaks upon desorption, and lower ice abundances result in smaller gas-phase peaks for these species. However, the effect of increasing ζ results in greater destruction of gas-phase material via ion-molecule protonation schemes and is especially strong for large t_{wu} (Figures 2.2-2.5) For these conditions, gas abundances become severely diminished at the desorption temperature. For small t_{wu}, abundances are also diminished with increasing ζ (panels $t_1\zeta_1$, $t_1\zeta_5$, $t_1\zeta_9$), although they survive to higher temperatures, since the time for which destruction can occur is very brief. Thus, abundances are larger for the remainder of the warm-up relative to large t_{wu}. Abundance trends of species having significant gas-phase formation routes are somewhat variable, though they are also generally diminished at large t_{wu} and high ζ.

To summarize these trends, large ζ leads to production of COMs on grains especially at low temperatures in the warm-up, while at higher temperatures these conditions also tend to destroy COMs once their formation has ceased. Large t_{wu} allow COMs to accumulate at low temperatures, but they are also destroyed at high temperatures. Intermediate values of t_{wu} provide a balance between early formation and late destruction of ices. Since most molecules lack significant gas-phase formation pathways, they are destroyed through protonation and dissociative recombination after they desorb. This effect is amplified for large t_{wu}. The trends seen in the fractional abundances are similarly carried through to the column densities calculated for COMs using the radiative transfer model.

According to these trends, rapidly evolving sources (i.e., those with short warm-up timescales) may lack significant formation or processing of dust-grain ice mantles, which corresponds to lower gas-phase abundances in warm regions. Alternatively, more slowly evolving sources would develop chemically processed grain mantles in their outer envelopes, but the constituents would likely be diminished in warmer regions. We may infer that sources with intermediate warm-up timescales and elevated ζ (on the order of 10^{-16} s^{-1}) provide a balance to these conditions and possess the greatest and most widespread chemical richness on grains and in the gas phase. It should be noted that the warm-up timescale corresponds to the physical/chemical evolution of a parcel of gas/dust but does not necessarily correspond to the physical age of the source as a whole. The warm-up stage in theory reflects both the increase in luminosity of the protostar and the gradual decrease in radial distance of the gas parcel from the source. The warm-up timescale therefore should have more to do with the overall mass accretion rate of the protostar than with its age.

2.5.1 General Trends in Simulated Column Densities and Excitation Temperatures

Similar trends are seen in the column densities of COMs calculated using our LTE radiative transfer and beam convolution model as are obtained for the peak fractional abundances in the models. Thus, for the COMs modeled here at least, this indicates that observed column density trends may be taken as a good indicator of the underlying chemical behavior. As may be seen in Figure 2.7, for short warm-up timescales, increasing ζ leads to greater COM column densities, whereas for long warm-up timescales, higher zeta leads to greater destruction of the COMs. Although there is some degeneracy seen between models of the same nominal cosmic-ray fluence, e.g., models $t_3\zeta_1$ and $t_2\zeta_2$, in general the models with the same fluence cannot be said to show the same behavior, although this varies for each molecule.

In all of the sources modeled here, T_{ex} for many molecules increases consistently across the model grid from large to small ζ (e.g., Figures 2.8(a)-(b)). This behavior emerges from the fact that large ζ destroys molecules in the gas phase more rapidly; rapid destruction in the gas phase prohibits the survival of those molecules to later times and thus to higher temperatures. However, considering the large errors in the observational determinations of T_{ex} by B07, which is typical for hot-core sources, the models show a much broader agreement with observations based on excitation temperature than on column density.

Such variation as there is in the simulated T_{ex} values appears to reflect a balance between the spatial region of emission (which depends on both the source density profile and the molecular fractional abundance) and the beam size, rather than the characteristic desorption temperature or temperature of greatest abundance in the gas. For example, ethanol (C_2H_5OH) desorbs from the dust grains at ~110 K, but its T_{ex} values are consistently higher. The centrally peaked density and temperature structure has a strong effect on the region of strongest emission. T_{ex} is typically in the range of about 130–170 K for NGC 6334 IRS 1 (Figure 2.8a). Furthermore, there are several models for which the gas-phase fractional abundances of ethanol remain large until the warm-up stage ends, at 400 K (e.g. Figure 2.2, panels $t_1\zeta_1$, $t_1\zeta_5$, $t_5\zeta_1$), but for which T_{ex} is not close to 400 K. This is due to the fact that, at the point in the radial profile where a temperature of 110 K is attained, the emission is extended but the gas density is somewhat low, and for the gas at 400 K, the gas density is high but the emission is compact. Instead, T_{ex} is intermediate to these values and represents a position where the gas density and spatial extent of the emission are both sufficiently high to dominate the line intensity. In fact, for the beam sizes simulated in these models, all of this emission is well within the telescope beam.

The agreement of modeled with observed values of T_{ex} and, in particular, N_{tot} is mixed. For source NGC 6334 IRS 1, for example, simulated values for ethanol agree well with observations, whereas those for dimethyl ether do not. B07 determined ethanol to have $N_{tot} = 1.9 \times 10^{16}$ cm^{-2} and $T_{ex} = 166 \pm 14$ K for this source. The best-fit model ($t_3\zeta_5$) from the present grid produces $N_{tot} = 1.4 \times 10^{16}$ cm^{-2} and $T_{ex} = 158 \pm 1$ K, which agrees well with the observations. However, observed N_{tot} and T_{ex} for dimethyl ether are 5.8×10^{17} cm^{-2} and 241 ± 35 K, respectively, whereas our best-fit model gives $N_{tot} = 2.0 \times 10^{16}$ cm^{-2} and $T_{ex} = 105 \pm 0$ K.

Thus, although the models are differentiated strongly for a molecule, it is quite possible that there exist systematic errors in the chemical treatment that underproduces it. For example, gas-phase COMs are destroyed by protonation ions in our models. However, other gas-phase molecules with high proton affinities such as ammonia may neutralize a significant fraction of these ions (Taquet et al. 2016). Accordingly, COM gas-phase abundances may be higher, though we do not currently account for such processes. Also, our model assumes an equal efficiency of UV photodissociation in the solid and gas phases. However, Kalváns (2018) suggests that solid-phase photodissociation is only about one-third as efficient as gas-phase photodissociation. This may result in some systematic error in modeling surface abundances; however, it is difficult to speculate how this error would propagate in the context of cosmic-ray ionization. Inaccuracies in the physical treatment are also possible. In particular, the density and temperature profiles that we use incorporate no smaller-scale or asymmetric structure, while more recent observations of, for example, NGC 6334 IRS 1 with ALMA indicate its presence (Brogan et al. 2018).

2.5.2 Constraints on ζ and t_{wu}

Based on a match parameter that directly compares the simulated and observed line-integrated intensities for a range of COMs (thus removing the need to compare column densities and excitation temperatures directly), we determined the best-matching model for each of the four observational sources, NGC 6334 IRS 1, NGC 7538, W33A, and W3(H_2O); see Table 2.5. These best-fit models correspond to a particular value of the cosmic-ray ionization rate and warm-up timescale. It is immediately apparent that the ζ values obtained are uniformly greater than the canonical value, 1.3×10^{-17} s^{-1}, while the warm-up timescales are uniformly shorter than any of the values previously used in our hot-core models (e.g., Garrod 2013; Belloche et al. 2017). The best-fit values of ζ range from around 2 to 20 times the canonical cosmic-ray ionization rate. The warm-up timescales are around 4–32 times shorter than the *fast* value of 5×10^4 yr used in the past. These timescales of around 10^3–10^4 yr indicate that there would be little time for ion-molecule processes to destroy gas-phase COMs, almost regardless of cosmic-ray ionization rate. The high ζ values favored by the fits are then free to produce high grain-surface abundances of COMs.

Although the constraints on ζ are lower than those determined toward the Galactic center (e.g., Oka et al. 2005; Le Petit et al. 2016), they are not inconsistent, as those observational values are more reflective of diffuse cloud conditions. Cosmic rays are attenuated by intervening dust as they pass through a source (Padovani et al. 2009; Padovani 2018; Rimmer et al. 2012). This implies that although we model ζ as 10^{-17} to 10^{-16} s^{-1}, these values only reflect conditions present within the sources. The values toward the edges are likely larger and could be on the order of 10^{-15} to 10^{-14} s^{-1}. The method of finding best-fit models presented here, based on COM abundances, provides means with which to estimate – albeit indirectly – the cosmic-ray ionization rate most appropriate to the dense conditions found in hot-core sources.

Referring to Table 2.5, the match parameter, κ, is greatest for NGC 6334 IRS 1 and lowest for W33A (with values of 0.471 and 0.261, respectively), indicating that the modeled integrated intensities of surveyed molecules have comparatively better agreement for NGC 6334 IRS 1 than W33A. In particular, methanol, ethanol, methyl formate, and dimethyl ether agree well for several models across the grid for NGC 6334 IRS 1, but have very poor agreement across the grid for W33A. The discrepancy could be attributed to the fact that NGC 6334 IRS 1 is observed to be chemically rich, whereas W33A is chemically poor (also see section 5.4). B07 note that NGC 7538 IRS 1 is also chemically poor, and it achieves the second-lowest κ value in our comparison (0.337). Alternatively, the temperature and density profiles that we use for these sources may not be such a good representation of reality as those for NGC 6334 IRS 1 and W3(H_2O).

Model comparison results for source W3(H_2O) show that best-matching models do not seem to converge in one region of the grid (Figure 2.11a). The fit is patchy,

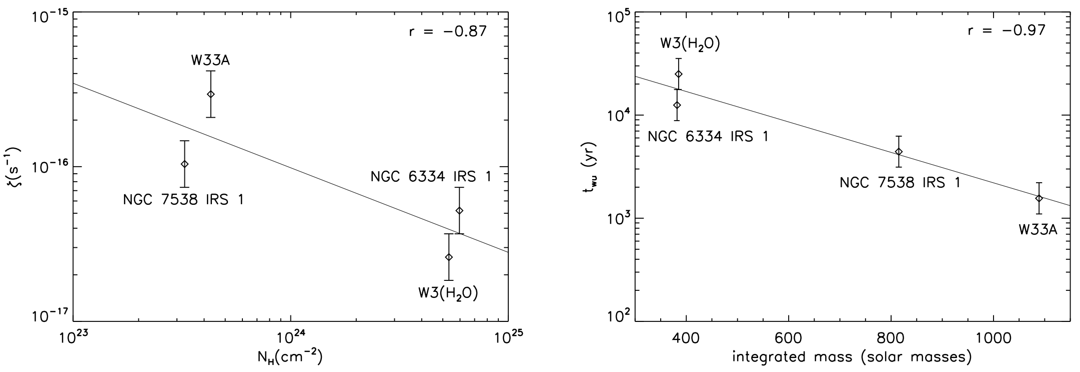

Figure 2.13: Relationships between ζ, t_{wu} and key physical parameters for observed sources. Panel (a) shows the best fit to ζ plotted as a function of the calculated unconvolved H column density for each source. Panel (b) shows the best fit to t_{wu} plotted as a function of stellar mass for each source. The equation of best fit is used to derive analytical expressions for the relationships among these parameters. Error bars on ζ and t_{wu} correspond to the model grid resolution.

and the best matches are spread across different regions of parameter space. The three best matches occur for models $t_4\zeta_4$, $t_6\zeta_7$, and $t_1\zeta_9$. This arises from individual molecules having their own best fits to observed integrated intensities in these different regions. For example, C_3H_4, dimethyl ether, and isocyanic acid agree best in the $t_4\zeta_4$ region, ethyl cyanide agrees well in both the $t_4\zeta_4$ and $t_6\zeta_7$ regions, and ethanol agrees well in both the $t_6\zeta_7$ and $t_1\zeta_9$ regions. The mixed agreement could be due to the fact that W3(H_2O) is a protobinary system rather than a single core (Chen et al. 2006), and the respective cores could possess disparate chemical compositions. Indeed, the other three sources are reported to consist of multiple fragments or substructures (Caproni et al. 2002; Beuther et al. 2013; Izquierdo et al. 2018), though they may all be consistent in age and composition, or dominated by a single component. Though it is unlikely for the components of W3(H_2O) to originate from different clouds, it could be that they vary in age and thus account for the chemical differences. If this is the case, then our modeling approach could provide an indirect means of chemically resolving such sources into multiple components.

To provide an alternative test for the rate of cosmic-ray-induced ionization provided by the best-fit models, we plot (Figure 2.13, panel (a)) the best-fit ζ as a function of total hydrogen column density, based on a simple integration of the gas density profiles provided by van der Tak et al. (2000). Following the theoretical relationship between these two quantities obtained by Padovani et al. (2009), Rimmer et al. (2012), and others, they are plotted here in log-log space. The error bars on the points indicate the uncertainty in the models based on the grid resolution. The negative correlation between ζ and N(H) shown in Figure 2.13a agrees qualitatively with the theoretical behavior. The correlation coefficient for the best-fit line is $r = -0.87$, with the fit given by

$$\log_{10}\zeta = (-0.547 \pm 0.25)\log_{10} N(\mathrm{H}) - (2.89 \pm 6.13) \tag{2.20}$$

A rough comparison between this fit and the recent calculations by Padovani et al. (2018) for dark-cloud conditions places our values a little above those authors' upper limit for ionization caused solely by external cosmic rays. This could provide evidence that there is some protostellar source of cosmic-ray ionization, an idea that Padovani and coworkers have also suggested. However, considering the few data points upon which our fit is based, our values would also be consistent with the upper values of ζ found by Padovani et al. (2018), without the assistance of an internal source. It is also reasonable to suggest that the values that provide the best fits to observed values could have some bias toward the earlier stages of chemical evolution, during which icy grain mantles are processed, which may be characterized by somewhat lower hydrogen column densities appropriate to this material being somewhat more extended and (relatively) diffuse. More specific modeling efforts are clearly needed that consider variable cosmic-ray ionization rates in the context of more detailed dynamical treatments. It is nevertheless encouraging that the values produced by our chemical/spectral model fits, which are otherwise unbiased with respect to total hydrogen column density, should produce the appropriate behavior for our sample of sources. This adds some further weight to the validity of the best-fit estimates for each source.

Figure 2.13(b) shows the warm-up timescales obtained from the best-fit models for each source, plotted against the integrated mass provided by the density profiles as determined by van der Tak et al. (2000). Here, there is an even stronger (anti)correlation ($r = -0.97$) for the log-linear best-fit line:

$$\log_{10} t_{wu} = (1.48 \pm 0.47 \times 10^{-3})M + (4.82 \pm 0.32) \tag{2.21}$$

where M is the integrated mass of a source in units of solar mass. Again, the clear relationship between these values adds further confidence to the general approach taken in this paper. The specific relationship in which warm-up timescales are shorter for more massive sources also makes sense, if this timescale is related to the mass accretion rate of the central protostar. The empirical relationship we find here goes in the same sense as that suggested by Viti et al. (2004), whereby more massive protostars would have shorter timescales. Their treatment was based on the protostellar luminosity function of Molinari et al. (2000), with the warm-up timescales ultimately constrained by contraction timescales. All of the sources we model here are high-mass objects; however, if this relationship holds to yet lower masses, one might expect that low-mass sources would be more strongly characterized by stronger gas-phase destruction of COMs, especially if combined with the somewhat higher cosmic-ray ionization rates that our fits suggest would be appropriate for sources with lower overall hydrogen column densities. This could manifest itself through a bias toward lower excitation temperatures in low-mass sources.

The accuracy of the above constraints may be limited by the fidelity of the temperature and density profiles used. These profiles are observationally determined best fits using continuum emission (van der Tak et al. 2000). These profiles may provide satisfactory agreement for extended regions of a source, but they fail in the compact regions where most molecular emission occurs. For example, recent ALMA surveys indicate great small-scale complexity in NGC 6334 I (Brogan et al. 2018).

Our comparison with observed molecular emission omits formaldehyde, formic acid, and formamide, on the basis of uniformly poor matches with the line-integrated intensities. All of these molecules are consistently overproduced in the models, which leads to integrated intensities that are too high for all sources. These results suggest that either the chemical or spectral modeling for these molecules is incorrect or

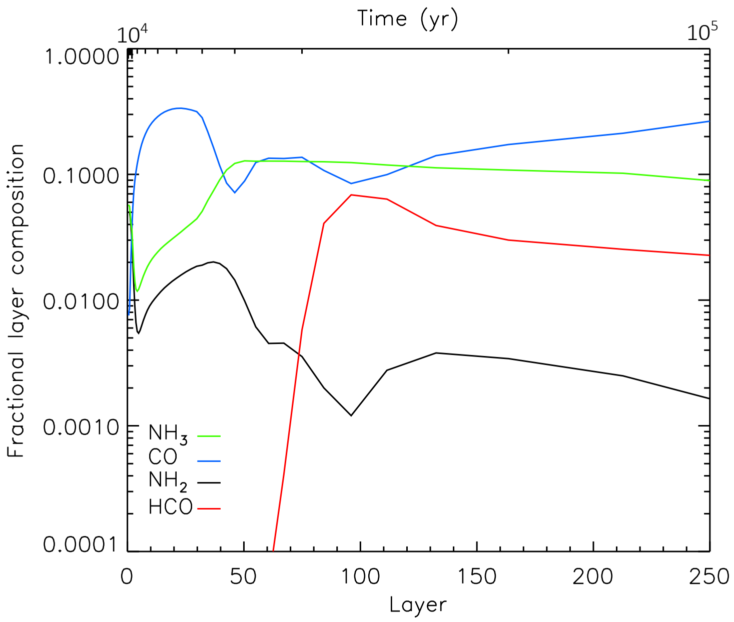

Figure 2.14: Ice-mantle abundances of NH_3, CO, NH_2, and HCO with respect to cumulative water abundances for each monolayer in a typical grain for model $t_7\zeta_3$. The model corresponds to the medium t_{wu} and standard ζ from G13.

incomplete.

The poor match of formaldehyde could be attributed to difficulty in tuning the balance between activation barriers for the reactions that form and destroy it on grains (listed in G13), which compose a part of the grain-surface chemistry network leading from CO to methanol. It is possible that either the barriers for H_2CO destruction to form CH_3O, CH_2OH, or HCO are too high, or the barriers for reformation by H abstraction from methanol are too low, or some combination thereof. However, the model results for methanol agree well with observations. Alternatively, trapping of formaldehyde in ice mantles may contribute to the poor match. If the models do not adequately account for trapping, then simulated abundances may be artificially large, in particular at low temperatures.

More likely, however, is that the radiative transfer calculations performed here are inadequate for this molecule. Only one transition of $H_2{}^{12}C^{16}O$ $(3_{1,2} - -2_{1,1})$ out of the seven searched for by B07 was detected by those authors in the sources that are modeled here. That line should have a critical density on the order of 10^7 cm^{-3}. If the majority of the gas-phase formaldehyde is released from grains and reaches a gas-phase abundance peak at around 40 K at the radii at which that temperature is achieved, the source densities, which we calculate from the physical profiles to be on the order of 10^5 cm^{-3}, are too low to assume LTE to be valid. The paucity of formaldehyde lines at millimeter/submillimeter frequencies that have both a small-enough Einstein A-coefficient and a low-enough upper energy level to be well populated at 40 K therefore means that a non-LTE treatment is unavoidable for an accurate reproduction of observed line intensities.

On the topic of formic acid production, the gas-phase reaction between formaldehyde and OH to generate formic acid is likely incorrect. The present network takes a 1:50 branching ratio between Reactions (6a) and (6b), while Alvarez-Idaboy et al.

Table 2.6: Calculated Column Densities for Glycine Using Best-Fit Models for Each Source.

Source	N_{tot} (cm^{-2})
NGC 6334 IRS 1	1.3(15)
NGC 7538 IRS 1	8.2(12)
W3(H_2O)	4.0(14)
W33A	6.4(13)

(2001), Ocaña et al. (2017), and Zanchet et al. (2018) suggest that Reaction (6b) may be yet more dominant, due to its lower energy barrier. Consequently, formic acid abundances are artificially high. Adjusting the branching ratio accordingly may yield more accurate results; we leave this to future study. It should be noted that the excitation temperatures obtained by B07 for formic acid are, except for source W3(H_2O), uniformly less than 100 K, while the value for W3)H_2O), 189 ± 108 K, is still consistent with such a low value. While this behavior may be in line with the model predictions of a low-temperature component for gas-phase formic acid abundance, it would also likely place this molecule, like formaldehyde, into a regime in which the LTE assumption is not strictly valid.

Formamide is overproduced and consequently optically thick in our simulations even after omitting the formation pathway $NH_{2(g)} + H_2CO_{(g)} \rightarrow NH_2CHO_{(g)} + H_{(g)}$ from the network. The rationale for excluding this reaction follows the finding by Song & Kästner (2016) that the entrance barrier to the reaction is too high to be viable, although Barone et al. (2015) suggest the converse. The fact that formamide remains overproduced in our models, in spite of the absence of this reaction, implies that the efficiency of our Reaction (13) is too high, as it is the only major formation pathway in the network. It is possible that the $NH_{2(s)}$ and $HCO_{(s)}$ radicals are segregated within actual ices. Given the high extinction threshold of CO (Whittet et al. 2001), $HCO_{(s)}$ could be expected to occupy outer ice layers to a greater extent than $NH_{2(s)}$, a possibility that our models cannot explicitly take into account in their subsequent chemistry. However, the collapse stage of our models does indeed allow the layering of these species to be traced during the formation of the ice on the grain surfaces and indicates that the radicals NH_2 and HCO both share their highest cumulative abundances with respect to water in outer ice layers (Figure 2.14). An alternative explanation is that the reaction of $NH_{2(s)}$ and $HCO_{(s)}$, which has another product branch, to form ammonia and $CO_{(s)}$, may not have the appropriate branching ratios, which are currently assumed to be 1:1. Indeed, H abstraction by $NH_{2(s)}$ should be efficient, and this branch may be underestimated in the models.

2.5.3 Implications for Glycine Detection

According to model results, glycine achieves the largest peak solid- and gas-phase abundances for models with medium t_{wu} and large ζ (Figure 2.4, panel $t_5\zeta_9$), corresponding to $t = 5.00 \times 10^4$ yr and $\zeta = 8.32 \times 10^{-16}$ s^{-1}. From these results, we may assert that larger ζ are most conducive to glycine formation. In the efforts to detect glycine, we may consider sources with similar ionization rates. For example, van der Tak et al. (2006) calculate $\zeta = 4 \times 10^{-16}$ s^{-1} toward Sgr B2, which is consistent for producing glycine in large abundances in our models.

The best-fit models may also offer an indication of glycine abundances in the four sources surveyed. We cite values of N_{tot} for glycine using the best-fit models in Table 2.6. NGC 6334 IRS 1 and W3(H_2O) have the largest N_{tot} of 1.3×10^{15} and 4.0×10^{14} cm^{-2} respectively. Accordingly, these sources may be also be candidates for future efforts to detect glycine with ALMA.

2.6 Conclusions

In this study, we have investigated the effects of varying the cosmic-ray ionization rate and warm-up timescale on the chemistry of COMs in hot cores. Clear behaviors emerge from this treatment, and trends may be identified in the interplay between the two physical parameters tested. However, it is also clear from this work that degeneracy between the two is limited; the total fluence of cosmic rays in these models is important, but the observable abundances of COMs depend on the explicit values of both the cosmic-ray ionization rate and the period of exposure.

By mapping the generic models onto physical profiles from the literature for observed sources, we have identified the best-fit model to reproduce observed molecular line emission from each of four hot-core sources. Although this method is simple, it has turned out to be a powerful technique and has produced clear relationships between the best-fit cosmic-ray ionization rate and warm-up timescale and the physical characteristics of the observed sources. The fact that these relationships exist and are are well behaved – especially that between the warm-up timescale and the hot-core mass – indicates that the determination of the best-fit models is meaningful. The fits to observed sources and the relationships between physical quantities that they establish may be useful for adaptation to modeling other hot-core sources. More dynamically detailed chemical simulations of both specific observational sources and of generic, model sources would be valuable to improve the constraint of the key physical quantities.

The use of COM abundances in this way to constrain cosmic-ray ionization rates naturally tends to bias those ionization rates toward those most appropriate for the dense regions in which such molecules are found. This is an improvement over more direct observational/modeling techniques that are based on ion abundances in more diffuse regions. The relationship between cosmic-ray ionization rate and total hydrogen column density that is established in the present study is a consistent with values at the upper limit of, or somewhat higher than, those established by others through separate theoretical calculations (Padovani et al. 2018).

Here we list a selection of main conclusions from this study:

1. The grid of chemical models of various cosmic-ray ionization rates and warm-up timescales indicates that larger ζ values tend to produce more radicals in the dust-grain-surface ices, which can react to form large abundances of COMs; at the highest ζ values tested here, destruction of these COMs on grains at higher temperatures and in the gas phase is also widespread.

2. These destructive effects associated with cosmic rays are most pronounced for long warm-up timescales (t_{wu}). The trends suggest that sources with intermediate warm-up timescales that also have medium to large ζ values (10^{-16} s^{-1}) may be the most chemically rich.

3. The direct comparison between observed and modeled emission-line-integrated intensities has proved to be a useful method for testing the fidelity of the models to observational COM abundances, which removes the requirement to obtain unique column density and excitation temperature values for each molecule.

4. The best-fitting models for four observed hot-core sources all provide cosmic-ray ionization rates higher than the canonical value and warm-up timescales shorter than any values previously used in our models.

5. The best-fitting models demonstrate a strong negative correlation ($r = -0.87$) between ζ and total hydrogen column density for each source. An even stronger negative correlation ($r = -0.97$) is found between warm-up timescale and total source mass, based on the integrated density profile. The emergence of these relationships gives further confidence in the validity of the chemical model fits. Assuming that density profiles for a specific source exist, these relationships may be useful in determining cosmic-ray ionization rates and warm-up timescales for other sources, in the absence of other information.

6. Following the chemical trends, glycine is produced in its largest abundance for medium t_{wu} and large ζ. Accordingly, observational efforts to detect it may benefit from studying sources with ζ on the order of 10^{-16} s^{-1} that also have only a modest total mass (to provide a longer warm-up timescale). NGC 6334 IRS 1 and W3(H_2O) also have the largest calculated values of N_{tot}, so they may be good targets for future detection.

7. Our models fail to reproduce observed results for formaldehyde, formic acid, and formamide. These molecules are generally overproduced by around two orders of magnitude. This could be attributed to problems with branching ratios of formation reactions that are present in the chemical network, to problems with trapping species in the ice, and to the use of a purely LTE radiative transfer model.

8. The best fits to modeled integrated intensities for W3(H_2O) lie in different regions of the cosmic-ray fluence grid, as some molecules agree well in one region, whereas others agree in a different region. The behavior could be attributed to the fact that the source is a protobinary system. If this is true, then it would imply that the existence of source substructure can be inferred through modeling t_{wu} and ζ, if those values differ between substructures.

9. NGC 6334 IRS 1 and W3(H_2O) have the best agreement among modeled and observed integrated intensities, whereas NGC 7538 IRS 1 and W33A have the worst. Poor mapping of static warm-up models to the temperature and density profiles may contribute to poor agreement.

Chapter 3

Combined Hydrodynamic and Gas-Grain Chemical Modeling of Hot Cores

C. J. Barger, K. H. Lam, R. T. Garrod, Z.-Y. Li, S. W. Davis, & E. Herbst

3.1 Introduction

Hot cores are high-mass star-forming regions with temperatures and gas densities in excess of 100 K and 10^7 cm^{-3} respectively. A notable feature of hot cores is their rich molecular line-emission in the millimeter/sub-millimeter range. A variety of complex organic molecules (COMs) including alcohols, aldehydes, esters, acids, and amines have been detected in high abundances toward these objects (Herbst & van Dishoeck 2009; Garrod & Widicus Weaver 2013). Furthermore, high gas densities allow COM emission in hot cores to be well-approximated by local thermodynamic equilibrium (LTE). In LTE, measured or modeled excitation temperatures represent local gas kinetic temperatures, which makes COMs valuable tracers of the inner thermal structure of hot cores. The rich chemical complexity of these sources makes them compelling objects to study, and they offer an appropriate setting in which theories of COM formation and processing in the ISM can be tested and refined.

Hot-core chemistry has long been known to be associated with the formation and sublimation of dust-grain ice mantles (Millar et al. 1991; Charnley et al. 2005). Simple molecules including water, carbon monoxide, formaldehyde, methanol, ammonia, and methane form or deposit on dust-grain surfaces during the early cold stages of hot-core formation. Chemical models and experiments (Garrod & Herbst 2006; Öberg et al. 2009a) demonstrate that radiative processing of ice mantles leads to the production of radicals derived from these molecules, which can recombine to produce more complex molecular structures. As protostellar radiation warms surrounding material, surface- and mantle-bound radicals become mobile via thermal diffusion, allowing the radicals to meet and react. For instance, CH_3O and HCO, derived from methanol and formaldehyde respectively, undergo rapid surface diffusion at around 30 K and may combine to create methyl formate (CH_3OCHO). As core temperatures surpass 100 K, the bulk of COMs formed on grains desorb into the gas phase where their spectral emission can be observed. The ejection of molecular material in this way can lead to further gas-phase production of molecules.

Chemical networks used in hot-core modeling have advanced in recent years to accommodate the ever-increasing set of detected molecules in the ISM, while the treatment of the physical structure of dust-grain ice mantles has also advanced. The three-phase modeling approach introduced by Hasegawa & Herbst (1993), which accounts for ice-mantle processes in addition to grain-surface and gas-phase processes, has been widely employed (Garrod & Pauly 2011; Garrod 2013; Taquet et al. 2014; Barger & Garrod 2020). Chemical networks have been continuously updated, particularly focusing on incorporating newly-detected or predicted COMs (e.g. Garrod et al. 2017). Although there remain inherent uncertainties regarding chemical mechanisms and parameters, these hot-core models have been successful in reproducing observed abundances in various star-forming sources to within order-of-magnitude tolerances.

Despite the successes of gas-grain hot-core models in reproducing observed chemical abundances, they continue to lack an accurate treatment of physical conditions in the context of star-formation. The density and temperature evolution in the models are based on generic parameterizations (e.g. Viti & Williams 1999), with the warm-up rate usually treated as a free parameter. The models also typically concentrate on only one representative – and arbitrary – position in the hot core; thus, no spatial structure is explicitly included, and differences in the physical histories of different regions within the source are ignored. Recent chemical modeling studies have employed physical models with coupled density and temperature evolution, based on observational constraints (Bonfand et al. 2019; Willis et al. 2020), while others have mapped the single-point temperature-dependent abundances onto physical profiles of observed sources (Garrod 2013; Barger & Garrod 2020) to obtain column density estimates. While providing a great improvement in the ability to compare with individual sources, such methods represent – at best – an analytical treatment of the time- and space-dependent physical conditions, and lack details that a fully self-consistent physical simulation may provide, such as a consideration of radiation propagation, and the effects of radiation pressure on the collapse timescale. A realistic, self-consistent temperature treatment is especially necessary for hot-core modeling, due to the strong dependence of the chemistry and desorption behavior of molecules on the dust and gas temperatures. A combination of hydrodynamic simulations with chemical models would provide much more realistic simulations of hot-core chemistry.

Such treatments are now more necessary than ever, as observations with ALMA highlight physical structures on very small spatial scales (e.g. Brogan et al. 2016; Belloche et al. 2019; Csengeri et al. 2019). Furthermore, in spite of this improved spatial resolution, molecular column density determinations are nevertheless dependent on line-of-sight integrated emission from a range of physical and chemical conditions through the source. Single-point models of hot-core chemistry therefore cannot capture the full range of physical/chemical conditions represented in observationally determined (i.e. column density-based) fractional abundances. Meaningful evaluation of model results therefore requires that the models explicitly trace the time-dependent physical and chemical evolution throughout the core, so that column densities and their ratios may be calculated and compared directly with observed values.

In this work we present combined one-dimensional physical and chemical models

Table 3.1: Important parameters for the dynamical model.

Mass-Accretion Rate ($M_\odot/yr$)	Total Mass ($M_\odot$)	Outer Radius (AU)	Final Stellar Mass ($M_\odot$)	Simulation Time (yr)	Final Density (cm^{-3})	# Trajectories
3.0×10^{-3}	65	9.89×10^{3}	25	1.0×10^{4}	4.1×10^{8}	78
1.0×10^{-3}	65	2.03×10^{4}	23	2.9×10^{4}	4.7×10^{8}	77
1.0×10^{-4}	65	9.29×10^{4}	30	2.9×10^{5}	7.6×10^{7}	83

of hot-core evolution that allow the spatial and time-dependence of the chemistry to be traced under realistic physical conditions; we plan to extend this work to two-dimensions (assuming axisymmetry) in the near future.

Ideally, one would compute the dynamics and chemistry during the process of dense core collapse and star formation simultaneously. However, it would be difficult to incorporate the detailed chemical treatments described above directly into the dynamical calculations, and the computational cost would be prohibitive at present. Our approach, described in detail below, de-couples the dynamics and chemistry; the dynamics are simulated first, which then yields the density and temperature distributions of the system at different times. Lagrangian tracer particles are used to record the density and temperature histories of representative parcels of gas, which are then used to evolve the chemistry of the gas parcels. This approach is reasonable, because the dynamics of the massive collapsing core is dominated by the gravity and, to a lesser extent, radiation, rather than the chemistry.[1] The use of the radiation hydrodynamic code *Athena++* (Stone et al. 2020) allows the effects of radiation on the gas dynamics to be captured. This also enables the self-consistent computation of the temperature that is crucial for the hot-core chemistry.

A set of radiation-hydrodynamic (RHD) models is run using three mass-accretion rates, to obtain the temporal and spatial information for Lagrangian trajectories up to a time when the stellar luminosity exceeds the Eddington Luminosity. The resulting physical data are used as the input for the three-phase astrochemical model *MAGICKAL*, which provides the final time- and space-dependent chemical abundances from which molecular column densities are calculated. These results are analyzed and compared with observational values.

The methods pertaining to the physical and chemical modeling are described in Section 2. Major results including time- and spatially-dependent chemical abundances are explored in Section 3. Discussion and conclusions are provided in Sections 4 and 5, respectively.

3.2 Methods

Two main techniques are employed in this study: (i) the simulation of physical structure and conditions through a hydrodynamically-evolving hot core, using radiation hydrodynamics (RHD); and (ii) the simulation of gas-grain chemical kinetics

---

[1] Magnetic fields can potentially be dynamically important, introducing a coupling between the chemistry and dynamics through the number densities of charged species, which control the degree of coupling between the magnetic field and the bulk neutral medium (e.g. Nakano et al. 2002; Li et al. 2011). Treating magnetic fields is beyond the scope of this paper.

influenced by those conditions. The RHD simulations are run first, to provide time-dependent physical conditions for a selection of trajectories as the core collapses. Each trajectory represents a mass-conserved parcel of gas (and dust), which begins at its own initial radius within the core. The physical conditions (such as gas density, temperature, visual extinction and radius) of each of these trajectories are tabulated. The chemical model is then run for each trajectory independently using these time-dependent input values; the chemistry of the different trajectories therefore do not have any influence over the physical results (nor over each other). The chemical and physical models thus may be considered coupled only in one direction. In order to prepare the chemical model for the main RHD evolution, a pre-collapse chemical model is run for each trajectory, under (mostly) atomic initial conditions; in these chemical models, the physical conditions for each trajectory starting-point evolve under a simple one-dimensional, isothermal, freefall collapse from diffuse conditions until the initial physical conditions of that trajectory are reached. The timescale of the freefall collapse is held constant for all trajectories in each of the three physical models, and is on the order of 10^5 yr (see Section 3.2.2 below for details). The chemical abundances obtained at the end of the pre-collapse models, which we label "stage 1", are used as the starting conditions for the main chemical models, which we label "stage 2".

The physical and chemical models are described in more detail in the subsections below.

3.2.1 Physical Model (RHD)

To obtain the physical models of hot cores, we solve the radiation-hydrodynamic equations using *Athena++* (Stone et al. 2020). Specifically, the equations that we solve are

$$\frac{\partial \rho}{\partial t} + \nabla \cdot (\rho \mathbf{v}) = 0, \tag{3.1}$$

$$\rho \frac{\partial \mathbf{v}}{\partial t} + \nabla \cdot (\rho \mathbf{v}\mathbf{v} + P) = \rho \mathbf{g} - \mathbf{G}_{\mathrm{r}}, \tag{3.2}$$

$$\frac{\partial E}{\partial t} + \nabla \cdot [(E + P)\, \mathbf{v}] = \rho \mathbf{v} \cdot \mathbf{g} - G^0_{\mathrm{r}}, \tag{3.3}$$

$$\frac{\partial I}{\partial t} + c\, \mathbf{n} \cdot \nabla I = S\,(I, \mathbf{n})\,. \tag{3.4}$$

Here, ρ is the gas density, $\mathbf{v}$ is the velocity, P is the gas pressure, E is the total energy density, $\mathbf{g}$ is the gravitational acceleration, and I is the (frequency-integrated) specific intensity of the radiation field. The energy density E is related to the gas pressure by

$$E = \frac{P}{\gamma - 1} + \frac{1}{2}\rho \mathbf{v}^2 \tag{3.5}$$

where $\gamma = 5/3$ is the adiabatic index. The radiative transfer equation is solved as in Jiang et al. (2019), but with two important updates: the equation is solved co-variantly following the modified procedure described in Section 3.2.3 of Chang et al. (2020) and additional terms are added to account for spherical symmetry, following the formalism described by Davis & Gammie (2020). The radiative force $\mathbf{G}_{\mathrm{r}}$ and net heating/cooling rate G^0_{r} couple the radiative and hydrodynamic momentum and energy equations, respectively.

The source term in the radiative transfer equation is defined as

$$S\left(I, \mathbf{n}\right) = c\rho \left[\kappa_{\mathrm{a,P}} \left(\frac{c a_{\mathrm{r}} T^4}{4\pi} - J\right) + \kappa_{\mathrm{a,R}} \left(J - I\right)\right], \tag{3.6}$$

where $\kappa_{\mathrm{a,P}}$ and $\kappa_{\mathrm{a,R}}$ are the Planck and Rosseland mean absorption opacity, respectively, T is the gas temperature, $J = \int I\, d\Omega / \left(4\pi\right)$ is the angular quadrature of the intensity (i.e., the mean intensity). $\mathbf{G}_{\mathrm{r}}$ and G_{r}^{0} are computed after the intensity is determined from the radiative transfer equation. In the limit that $v \to 0$, they are given by $-\rho\kappa_{\mathrm{a,R}}\mathbf{F}_{\mathrm{r}}/c$ and $c\rho\kappa_{\mathrm{a,P}}\left(a_{\mathrm{r}}T^4 - E_{\mathrm{r}}\right)$, where $\mathbf{F}_{\mathrm{r}}$ is the radiation flux and E_{r} is the radiation energy, respectively. The gas temperature is calculated using the ideal gas law $P = \rho k_{\mathrm{B}} T/\mu$ with $\mu = 2.33\,\mathrm{u}$. We adopted the same prescription of frequency-averaged absorption opacity as in Kuiper et al. (2010). In order to speed up the calculations, the reduced speed of light approximation (see. e.g. Chang et al. 2020) is used with a reduction factor of 10^3.

We solved the equations in 1D spherical symmetry using 128 logarithmically spaced cells in the radial direction. At the inner boundary (see below), the gas that flows into the central sink cell is collected and added to the mass of the central star. The central star is then coupled with the simulations by setting the inner boundary of the radiation. The total luminosity L_{tot} of the central star is the sum of the accretion luminosity L_{acc} and stellar luminosity L_*. The accretion luminosity is computed using

$$L_{\mathrm{acc}} = \frac{GM_*}{R_*}\dot{M}, \tag{3.7}$$

where M_* is the mass of the central star, R_* is the stellar radius, and $\dot{M}$ is the mass accretion rate. The stellar radius and luminosity are taken from Hosokawa & Omukai (2009) according to the chosen mass accretion rate. At the outer boundary of the simulations, the intensity is set such that the effective temperature is equal to the initial gas temperature.

We performed three simulations with expected mass accretion rates of 3×10^{-3}, 10^{-3} and $10^{-4}\,\mathrm{M}_{\odot}\,\mathrm{yr}^{-1}$. The initial density profiles assume a singular isothermal sphere (Shu 1977) with a constant temperature of 8 K and zero velocity. The total mass, M_{tot}, and outer radius, R_{max}, used in each calculation are summarized in Table 3.1, along with other selected parameters.

The inner boundaries are set to $R_{\mathrm{min}} = 10\,\mathrm{AU}$ for all models in order to resolve the dust sublimation front (Kuiper et al. 2010). The initial mass of the central star is, therefore, $M_{*,0} = M_{\mathrm{tot}} R_{\mathrm{min}}/R_{\mathrm{max}}$. The initial intensity is set to be in equilibrium with an effective temperature of 8 K. The models are able to produce the expected mass accretion rates up to a time when the radiative pressure force starts to dominate the gravity, as shown in Section 3.3.1.

3.2.2 Chemical Model

We use the three-phase astrochemical kinetics model *MAGICKAL* (Garrod 2013) to simulate hot-core chemical evolution based on the three one-dimensional physical models described above. The physical models are set up to provide data for four thousand individual trajectories, from which only a selection are drawn for chemical simulations. For physical setups with mass-accretion rates 3.0×10^{-3}, 1.0×10^{-3}, and 1.0×10^{-4} $M_{\odot}/yr$, we produce chemical models for 78, 77, and 83 unique trajectories, respectively (see Table 3.1), corresponding to different initial radii. The number and spacing of trajectories are chosen to ensure a sufficiently high resolution in temperature at the end-point of the chemical models, since our chemical outputs are strongly temperature-dependent. For trajectories that finish at temperatures at or below about 60 K, we choose enough trajectories to produce a maximum spacing of 5 K. Between 60 and 200 K, we choose trajectories separated by a maximum of 2 K; a finer resolution is chosen in this temperature regime because this is where much of the thermal desorption of COMs occurs. For trajectories that finish with temperatures between 200 and 300 K, a 10 K maximum spacing is used. For trajectories that finish between 300 and 400 K, the maximum spacing is 15 K. The coarse resolution in the highest temperature regimes is sufficient because the chemical evolution becomes less variable. Consistent with previous studies, all chemical models are limited to a maximum temperature of 400 K, beyond which the gas and grain chemistry could become unreliable. Note that the resolution considerations above do not concern the temperature resolution within each individual chemical model, which is determined by the numerical solver, based on the variable time-step required to ensure error-per-step values of 10^{-4} in chemical abundances.

The gas-grain chemical network used here is based on that presented by Garrod (2013) and updated by (Garrod et al. 2017), and includes the isocyanide chemistry presented by Willis et al. (2020). Although not explored here, other additions to the network pertaining to the current work include gas-phase and grain-surface/mantle-processing of vinyl alcohol (C_2H_3OH) and ethylene oxide (C_2H_4O, see Garrod et al., *in prep.*). We also include a set of reactions in which proton transfer occurs between certain protonated molecules and ammonia in the gas phase, following the work of Taquet et al. (2016). These reactions generate protonated ammonia and neutral gas-phase molecules. Proton transfer to ammonia is allowed for species whose unprotonated form has a proton affinity that is less than that of ammonia. The rates of these processes are assumed to occur at the collisional rate calculated for the ion-molecule pair in question, calculated using the method of Herbst & Leung (1986).

Chemical evolution in the model proceeds by reactions and energetic processes. Grain-surface and ice-mantle reactions occur via the Langmuir-Hinshelwood mechanism. Adsorbed species thermally diffuse across the surface and through the mantle until they meet another species with which to react. Thermal diffusion occurs once a species acquires sufficient energy to overcome its diffusion barrier. Diffusion barriers used in this work are based on those given by Garrod (2013). The modified-rate approach described by Garrod (2008) is used for surface reactions when applicable. Our network includes various ion-neutral, neutral-neutral, radical-neutral, radical-radical, and dissociative recombination reactions in the gas phase. Transfer of species between the gas and grain-surface can occur through various desorption schemes (see Barger & Garrod 2020, and references therein) and accretion. Chemical processing may also occur via (UV-induced) cosmic-ray ionization and photodissociation, as well as by direct cosmic-ray impingement for gas-phase species.

To ensure that the chemical modeling of the dynamical evolution begins from appropriate initial conditions, the chemistry of each trajectory is treated as a two-stage process. A pre-collapse stage, which we label “Stage 1”, allows the chemical and physical conditions of each individual trajectory to be reached through a gradual evolution from diffuse conditions to the somewhat denser initial conditions for “Stage

2" (where the latter corresponds to the dynamical evolution calculated using the RHD simulations).

Stage 1 starts under mostly atomic conditions (excepting H_2), with the gas density evolving under a simple freefall collapse (Nejad et al. 1990); this is much like past hot-core models (e.g. Barger & Garrod 2020), with the distinction that the final Stage-1 density is much lower in the present case. During Stage 1, the preparatory chemical model for each trajectory assumes an initial, local gas number density of $n_H = 1.0 \times 10^3$ cm^{-3}, which then evolves over time (independent of the other trajectories). The freefall collapse timescale in each case is ~1 Myr. The use of this simple treatment to prepare the chemical model allows the dynamical simulations to concentrate explicitly on the later evolution of the dense core from which the hot core forms.

During Stage 1, the dust temperature evolves as a function of the visual extinction (Garrod & Pauly 2011), while the gas temperature is held constant at 10 K. To determine the evolution of the visual extinction over time during Stage 1, the extinctions at the end of Stage 1 (i.e. the beginning of Stage 2) are calculated, using the initial Stage-2 density profile that is already defined. Based on the radial position of each trajectory at the start of Stage 2, the density profile is integrated outward to obtain the total H column density, which is then converted into a visual extinction (Bohlin et al. 1978), with an additional background extinction of 3 added on, i.e.

$$\begin{aligned} A_{\mathrm{V,basic}} &= \frac{3.1}{5.8 \times 10^{21}} N_H \\ A_{\mathrm{V,tot}} &= A_{\mathrm{V,basic}} + 3 \end{aligned} \tag{3.8}$$

Knowing this visual extinction at the end of Stage 1 for each trajectory/chemical model, the visual extinction $A_{\mathrm{V,basic}}$ is then scaled with $n_H^{2/3}$ during the Stage-1 evolution. The hydrogen number density, n_H (cm^{-3}), is derived from the gas density ρ (g cm^{-3}) following

$$n_H = 4.428 \times 10^{23} \rho, \tag{3.9}$$

which is based on a mean-molecular mass calculation assuming local molecular hydrogen and atomic helium fractional abundances of 0.5, and 0.09 respectively (the small atomic H fractional abundance of 2×10^{-3} is ignored). The initial chemical abundances are taken from Garrod (2013).

During Stage 2, the evolution of time, temperature, density, and spatial position are then treated according to the outputs of the RHD model (in which the gas and dust temperatures are assumed to be equal). In cases where the Stage-2 gas or dust temperature is lower than the final Stage-1 gas or dust temperature, the higher value is chosen in either case. This ensures complete continuity in physical conditions between Stages 1 and 2. During Stage 2, the visual extinction for each trajectory is again calculated as a function of N_H, using the instantaneous one-dimensional density profile produced by the dynamical calculations.

A summary of important modeling parameters is provided in Table 3.1.

3.3 Results

The following subsections describe the physical and chemical modeling results. A basic analysis of the accretion rate and luminosity for the $10^{-3}\,\mathrm{M}_\odot\,\mathrm{yr}^{-1}$ model is provided. Trends in fractional abundances and column densities among the three mass-accretion rates are presented for nine complex organic molecules relevant to hot-core chemistry.

3.3.1 RHD Model Results

With the adoption of the initial conditions described in Section 3.2.1, the expected initial constant accretion rates are reproduced to an acceptable tolerance for all models. Figure 3.1 shows the accretion history of the representative $10^{-3}\,\mathrm{M_\odot\,yr^{-1}}$ model; the accretion rate adheres closely to the expected $10^{-3}\,\mathrm{M_\odot\,yr^{-1}}$ value over the first 2/3 of the simulation. The evolution of the luminosity of the central star in the same model is shown in Figure 3.2. In all models, the luminosity is initially dominated by the accretion luminosity. The stellar luminosities then start to take over around the mid-point of the simulations. For the $10^{-3}\,\mathrm{M_\odot\,yr^{-1}}$ model, the accretion slows down at $t \simeq 20$ kyr or $M_* \simeq 20$ $\mathrm{M_\odot}$, which is when the stellar luminosity reaches the Eddington luminosity ($\sim 10^5\,\mathrm{L_\odot}$). All of the results are consistent with Kuiper et al. (2010).

Figures 3.3 and 3.4 show the temperature and density values, respectively, for which chemistry is modeled in each of the mass-accretion rate models. Values for each individual trajectory are marked, with different colors representing different evolutionary times.

In general, temperatures and densities increase in all modeled trajectories as the simulation proceeds (for all three models), while the radial distribution of trajectories also becomes much more extended (Figure 3.3) due to the greater infall velocities at smaller radii. All three mass-accretion rate models reach a final temperature of 400 K (panels (a) through (c)), although the final density varies with each model. In particular, the 1.0×10^{-4} $M_\odot/yr$ model reaches a final density (panel (f)) that is around a factor 5–6 lower than the other two models. Also, the time it takes for the temperature and density to evolve significantly increases as the mass accretion rate decreases (Figure 3.4).

Figure 3.4 shows the physical conditions experienced by the innermost trajectory for which the chemistry is simulated, for each accretion-rate model, as a function of time. The climb to the final density and temperature is seen to be quite rapid at the end, after a long period of only modest growth; this is especially true for the lowest accretion-rate model.

3.3.2 Chemical Results

We focus on the chemical results of ten commonly-studied COMs: methanol (CH_3OH), ethanol (C_2H_5OH), methyl formate (CH_3OCHO), glycolaldehyde (CH_2OHCHO), dimethyl ether (CH_3OCH_3), formaldehyde (H_2CO), methyl cyanide (CH_3CN), ethyl cyanide (C_2H_5CN), methyl isocyanide (CH_3NC), and vinyl cyanide (C_2H_3CN). We discuss fractional abundance and column-density trends in the following sub-sections.

Fractional Abundances

To assess the chemical response to the three different physical models, we generate fractional abundance plots for various COMs with respect to molecular hydrogen, shown in Figures 3.5 and 3.6, with panels ordered in the same way as for the physical

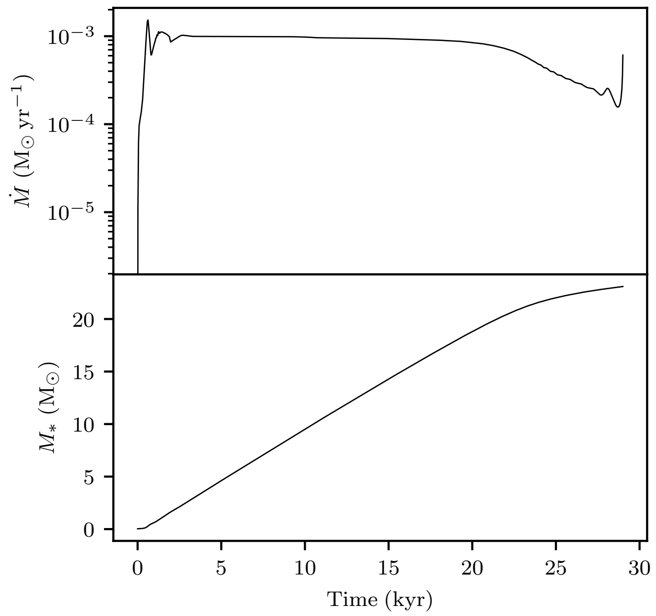

Figure 3.1: Evolutionary history of the central star. The upper and lower panels show the accretion rate and stellar mass of the representative $10^{-3}\,\mathrm{M_\odot\,yr^{-1}}$ model, respectively.

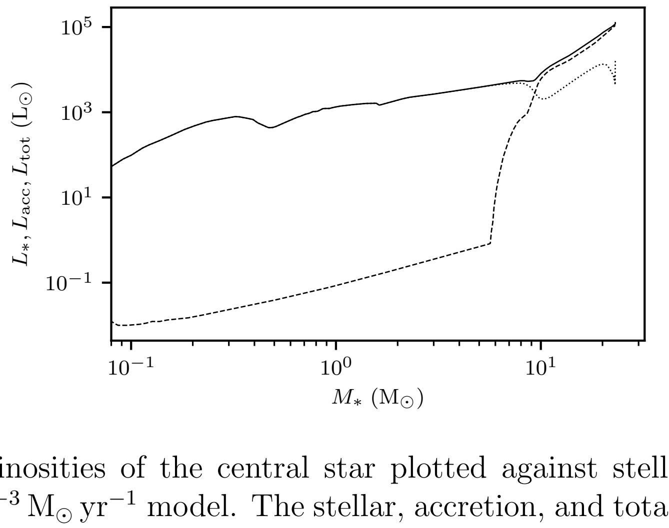

Figure 3.2: Luminosities of the central star plotted against stellar mass, for the representative $10^{-3}\,\mathrm{M_\odot\,yr^{-1}}$ model. The stellar, accretion, and total luminosities (as functions of stellar mass) are given by dashed, dotted, and solid lines, respectively.

Table 3.2: Peak gas-phase fractional abundances for the innermost trajectory of each mass-accretion rate model.

Species	3.0×10^{-3} $(M_{\odot}/yr)$	1.0×10^{-3} $(M_{\odot}/yr)$	1.0×10^{-4} $(M_{\odot}/yr)$
CH_3OH	6.5(-6)	6.5(-6)	7.7(-7)
C_2H_5OH	2.3(-7)	3.0(-7)	2.2(-7)
CH_3OCHO	1.3(-7)	1.1(-7)	9.5(-11)
H_2CO	2.3(-6)	2.2(-6)	1.2(-9)
CH_3CN	1.2(-8)	1.3(-8)	1.6(-8)
C_2H_5CN	1.5(-8)	1.6(-8)	3.5(-8)
CH_3NC	4.3(-10)	8.1(-10)	2.1(-10)
C_2H_3CN	4.8(-9)	9.2(-9)	2.1(-10)
CH_3OCH_3	6.4(-9)	1.3(-8)	6.4(-8)

conditions in Figures 3.3 and 3.4. Each panel in Figure 3.5 corresponds to all trajectories at the final simulation time, whereas each panel in Figure 3.6 tracks the innermost trajectory through all simulation times. Generally, COMs become abundant in the gas-phase at a radius and time corresponding to the temperature at which thermal desorption occurs.

Surface- and ice-mantle abundances are generally static for all molecules until the molecules desorb (Figure 3.5). Most COMs form first on grains either in the Stage-1 collapse, or early in the Stage-2 warm-up, by hydrogenation or by radical addition. Methanol and formaldehyde, for example, form late in the cold collapse phase by successive hydrogenation of CO. Ethanol forms during the warm-up beginning at about 12 K via addition of CH_3 and CH_2OH. Methyl formate and glycolaldehyde begin to form at around 15 K by addition of HCO with CH_3O and CH_2OH, respectively. Methyl cyanide is formed early in the warm-up by addition of CH_3 and CN; methyl isocyanide, on the other hand, is formed by radiative association and subsequent recombination of CH_3^+ and HCN in the gas phase (Willis et al. 2020). Both ethyl and vinyl cyanides form during the collapse phase via successive hydrogenation of C_3N. A more thorough discussion of formation and destruction mechanisms is presented by Barger & Garrod (2020).

For most COMs, except formaldehyde, desorption begins at about 105 K. This corresponds to a radius of 3.0×10^{16} cm (2,000 au) for the 3.0×10^{-3} $M_{\odot}/yr$ model, 2.8×10^{16} cm (1,870 au) for the 1.0×10^{-3} $M_{\odot}/yr$ model, and 2.4×10^{16} cm (1,600 au) for the 1.0×10^{-4} $M_{\odot}/yr$ model. Desorption is typically complete by 130 K, where peak gas-phase abundances are achieved (see Table 3.2). Formaldehyde begins to desorb at about 37 K, due to its low binding energy. This corresponds to a radius of 5.9×10^{16} cm (3,940 au) for the 3.0×10^{-3} $M_{\odot}/yr$ model, 9.4×10^{16} cm (6,280 au) for the 1.0×10^{-3} $M_{\odot}/yr$ model, and 1.7×10^{17} cm (11,400 au) for the 1.0×10^{-4} $M_{\odot}/yr$ model.

After desorption occurs, gas-phase abundances are also generally static for all molecules except formaldehyde and methyl isocyanide (Figure 3.5). Abundances of these molecules especially decline for the 1.0×10^{-4} $M_{\odot}/yr$ model. Peak gas-phase abundances are generally consistent among the 3.0×10^{-3} and 1.0×10^{-3} models. However, gas-phase abundances are notably diminished for the 1.0×10^{-4} $M_{\odot}/yr$ model, especially for formaldehyde and methyl formate.

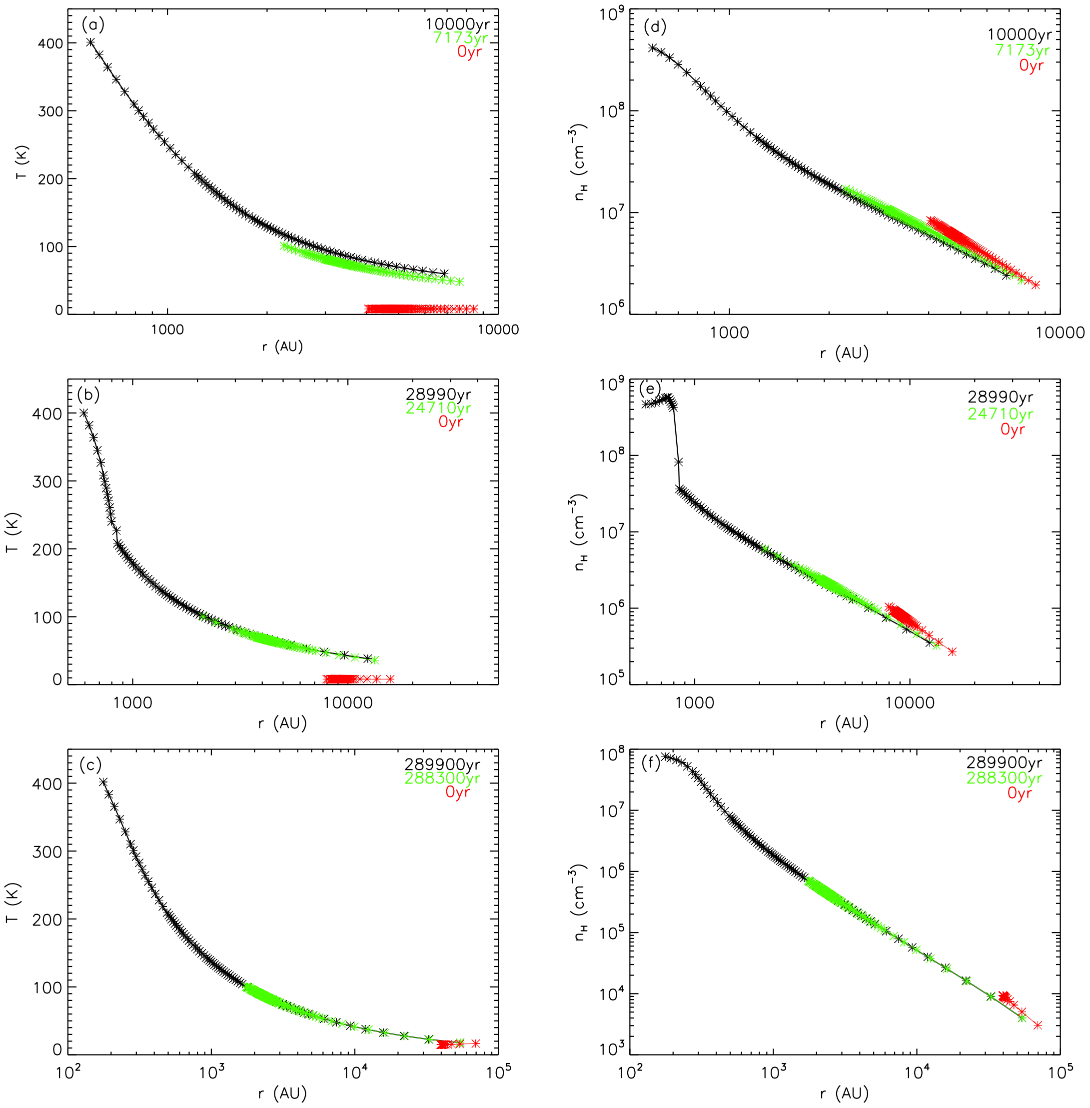

Figure 3.3: Radius-dependent physical profiles of the three mass accretion rates used in the chemical models. Panels (a) through (c) show temperature profiles as a function of radius, whereas panels (d) through (f) show density profiles as a function of radius. Upper panels (a and d) correspond to the 3.0×10^{-3} $M_{\odot}/yr$ mass accretion rate, middle panels (b and e) correspond to the 1.0×10^{-3} $M_{\odot}/yr$ mass accretion rate, and the lower panels (c and f) correspond to the 1.0×10^{-4} $M_{\odot}/yr$ mass accretion rate. The black curves represent the final stage-2 simulation time, the green curves represent a stage-2 simulation time corresponding to 100 K for the innermost trajectory of each mass accretion rate, and the red curves represent the initial stage-2 simulation time. Note that the horixontl axis values for all three mass accretion rates.

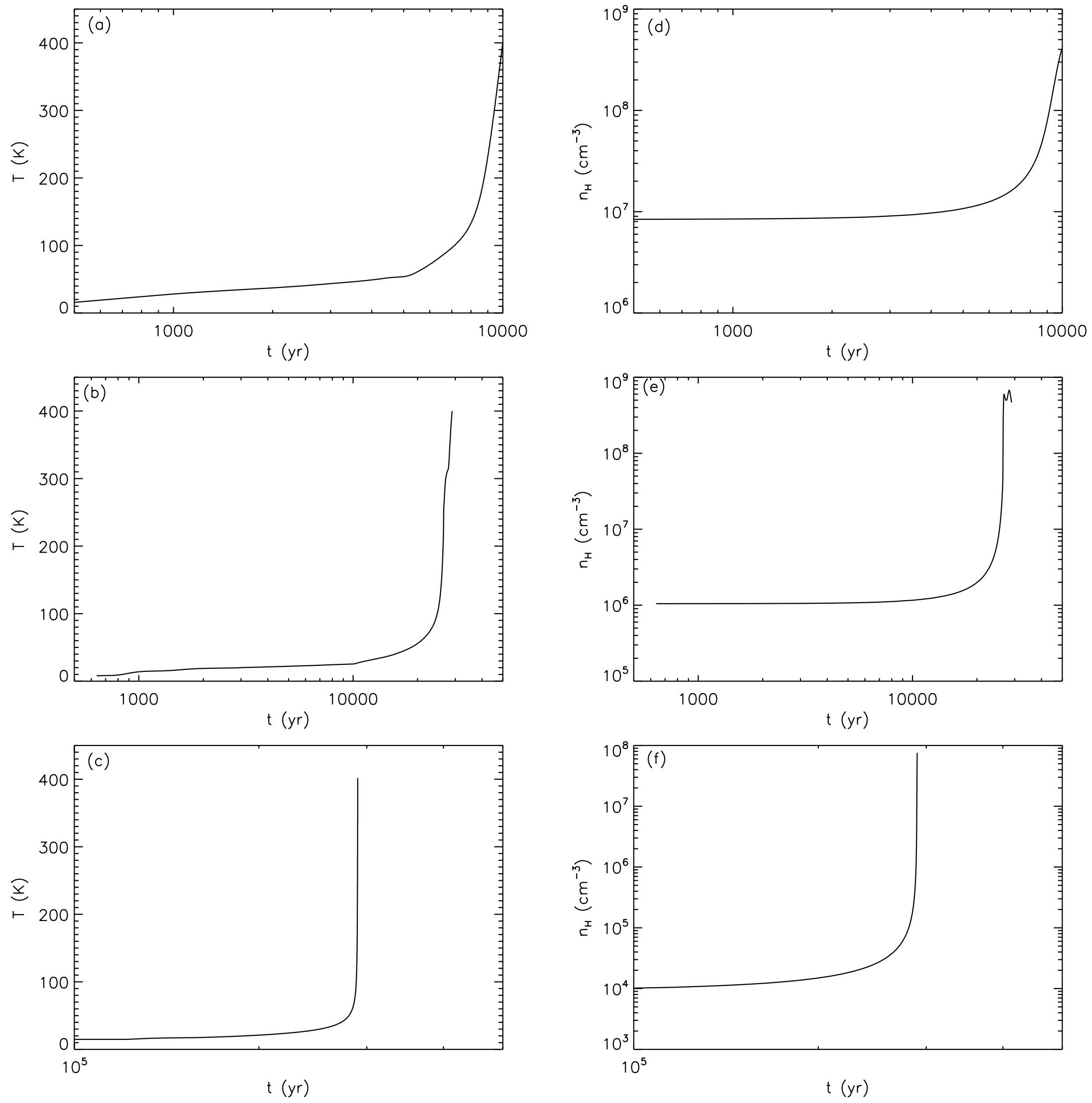

Figure 3.4: Time-dependent physical profiles of the three mass-accretion rates used in the chemical models. Panels (a) through (c) illustrate temperature profiles as a function of time, whereas panels (d) through (f) illustrate density profiles as a function of time. Upper panels (a and d) correspond to the 3.0×10^{-3} $M_{\odot}/yr$ mass-accretion rate, middle panels (b and e) correspond to the 1.0×10^{-3} $M_{\odot}/yr$ mass-accretion rate, and lower panels (c and f) correspond to the 1.0×10^{-4} $M_{\odot}/yr$ mass-accretion rate. Note that the horizontal axis varies for all three mass-accretion rates.

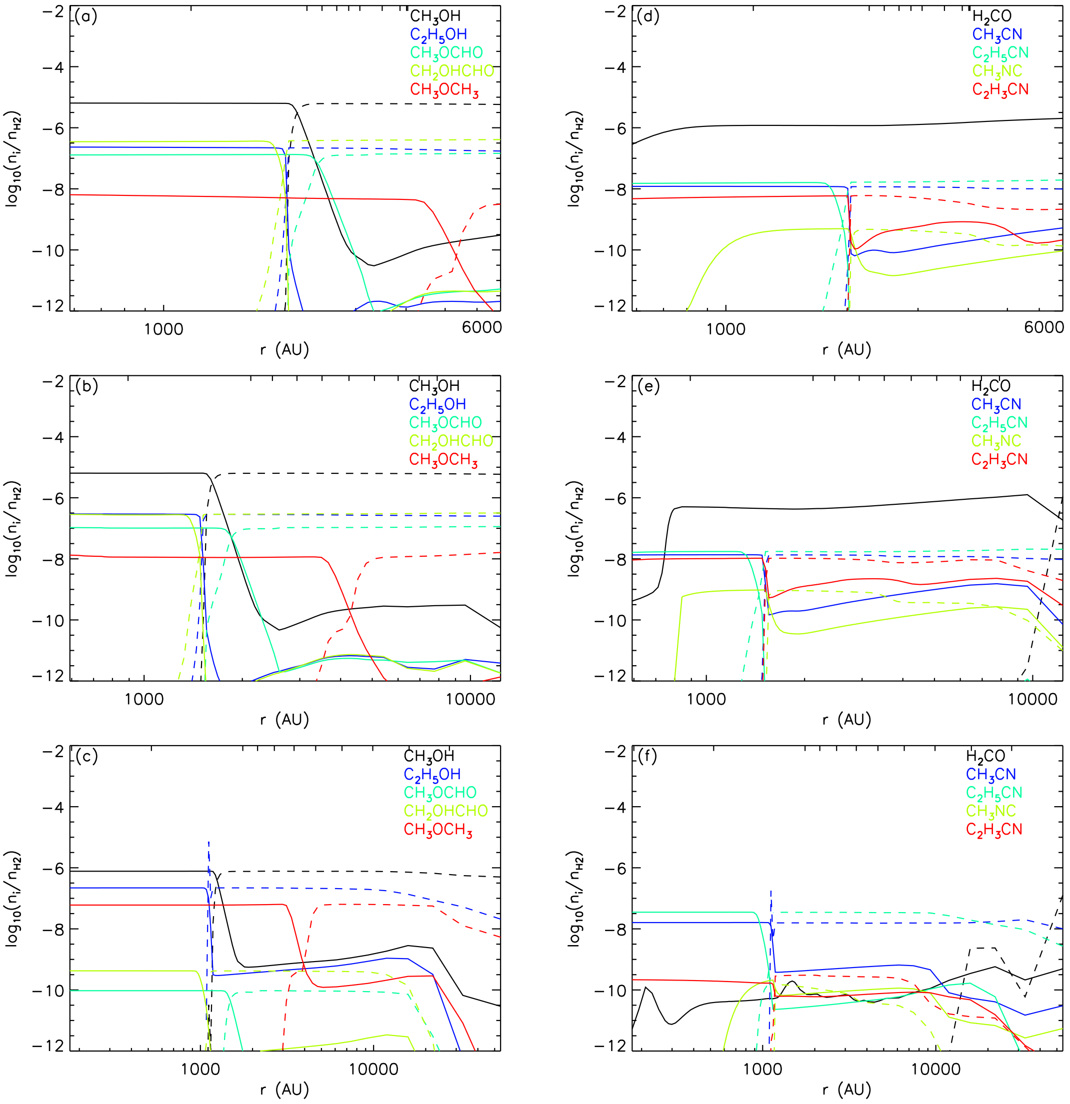

Figure 3.5: Spatially-dependent fractional abundance plots (with respect to H_2) for select complex organic molecules, at the end time of each accretion-rate model. Panels (a) through (c) show fractional abundances for methanol (black), ethanol (blue), methyl formate (green), glycolaldehyde (yellow), and dimethyl ether (red). Panels (d) through (f) show fractional abundances for formaldeyde (black), methyl cyanide (blue), ethyl cyanide (green), methyl isocyanide (yellow), and vinyl cyanide (red). Upper panels (a and d) correspond to the 3.0×10^{-3} $M_{\odot}/yr$ mass-accretion rate, middle panels (b and e) correspond to the 1.0×10^{-3} $M_{\odot}/yr$ mass-accretion rate, and lower panels (c and f) correspond to the 1.0×10^{-4} $M_{\odot}/yr$ mass-accretion rate. Solid lines correspond to gas-phase abundances, whereas dashed lines correspond to surface/ice-mantle abundances. Note that the range for the horizontal axis is different for models of different mass accretion rates.

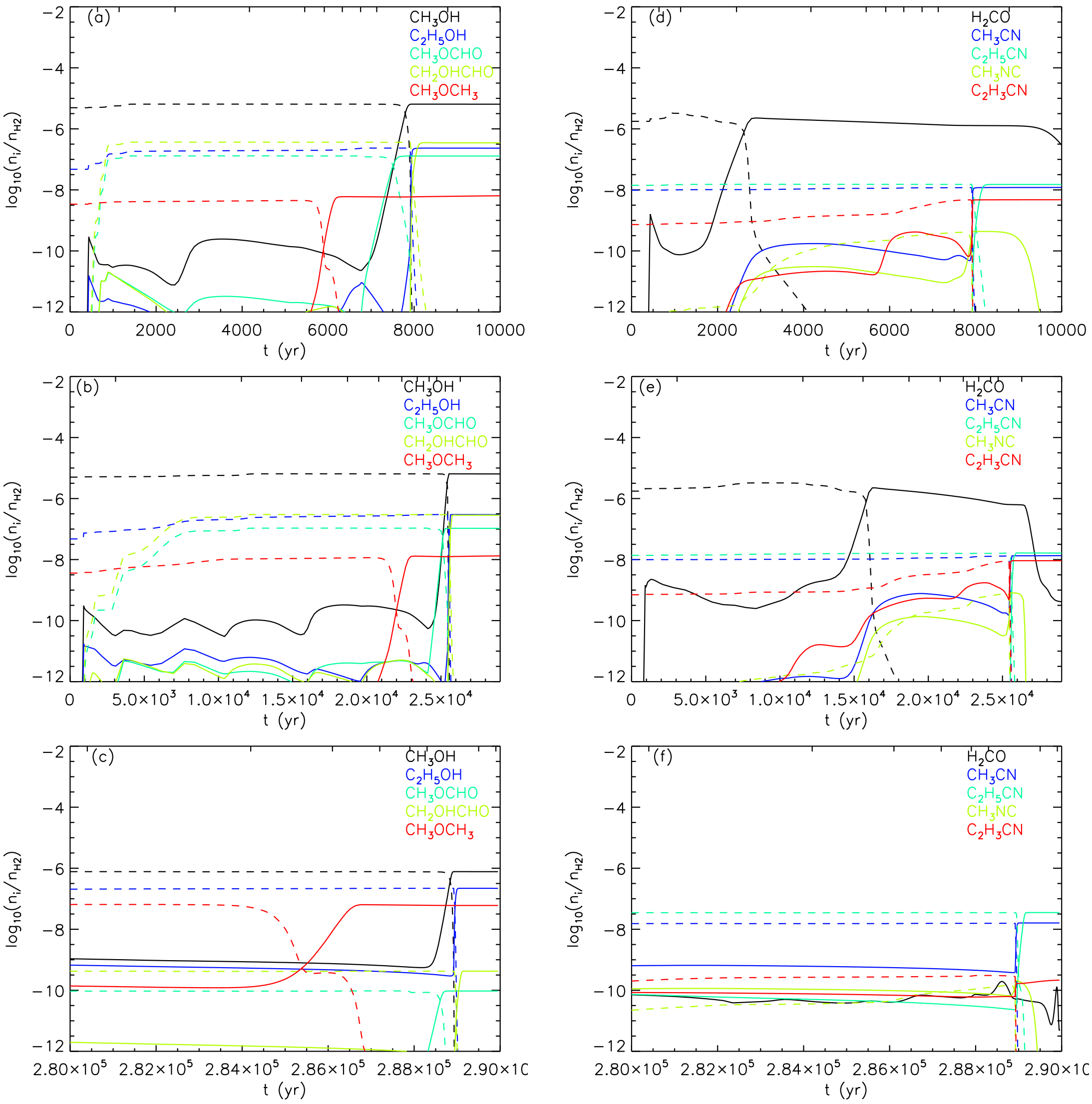

Figure 3.6: Time-dependent fractional abundance plots (with respect to H_2) for select complex organic molecules, for the innermost trajectory in each accretion-rate model. Panels (a) through (c) show all-time innermost trajectory fractional abundances for methanol (black), ethanol (blue), methyl formate (green), glycolaldehyde (yellow), and dimethyl ether (red). Panels (d) through (f) show all-time innermost trajectory fractional abundances for formaldehyde (black), methyl cyanide (blue), ethyl cyanide (green), methyl isocyanide (yellow), and vinyl cyanide (red). Upper panels (a and d) correspond to the 3.0×10^{-3} $M_\odot/yr$ mass-accretion rate, middle panels (b and e) correspond to the 1.0×10^{-3} $M_\odot/yr$ mass-accretion rate, and lower panels (c and f) correspond to the 1.0×10^{-4} $M_\odot/yr$ mass-accretion rate. Solid lines correspond to gas-phase abundances, whereas dashed lines correspond to surface/ice-mantle abundances. Note that the range for the horizontal axis is different for models of different mass accretion rates.

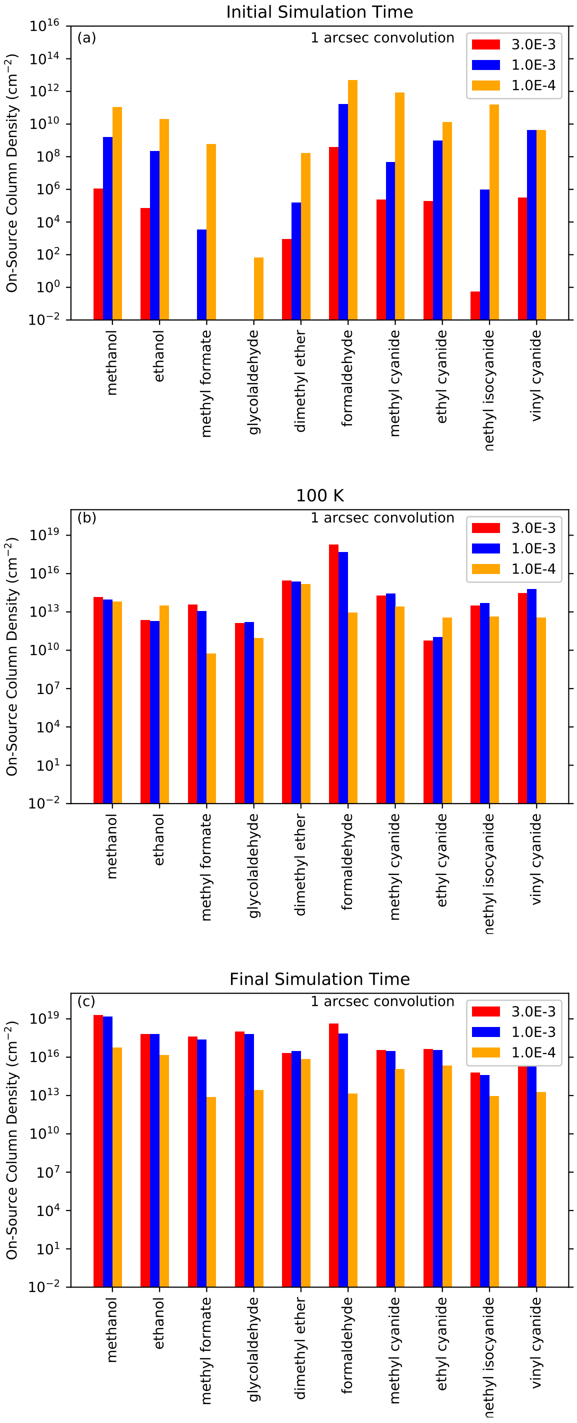

Figure 3.7: On-source column densities for select complex organic molecules using a 1 arcsec beam convolution. The red bars illustrate column densities for the 3.0×10^{-3} $M_{\odot}/yr$ model, the blue bars illustrate column densities for the 1.0×10^{-3} $M_{\odot}/yr$ model, and the orange bars illustrate column densities for the 1.0×10^{-4} $M_{\odot}/yr$ model. Panel (a) shows column densities for the initial stage-2 simulation time, panel (b) shows column densities for stage-2 simulation times that correspond to a temperature of 100 K, and panel (c) shows column densities for the final stage-2 simulation time. Note that the ranges for the vertical axis are the same for the middle and right panels but different from that of the left panel.

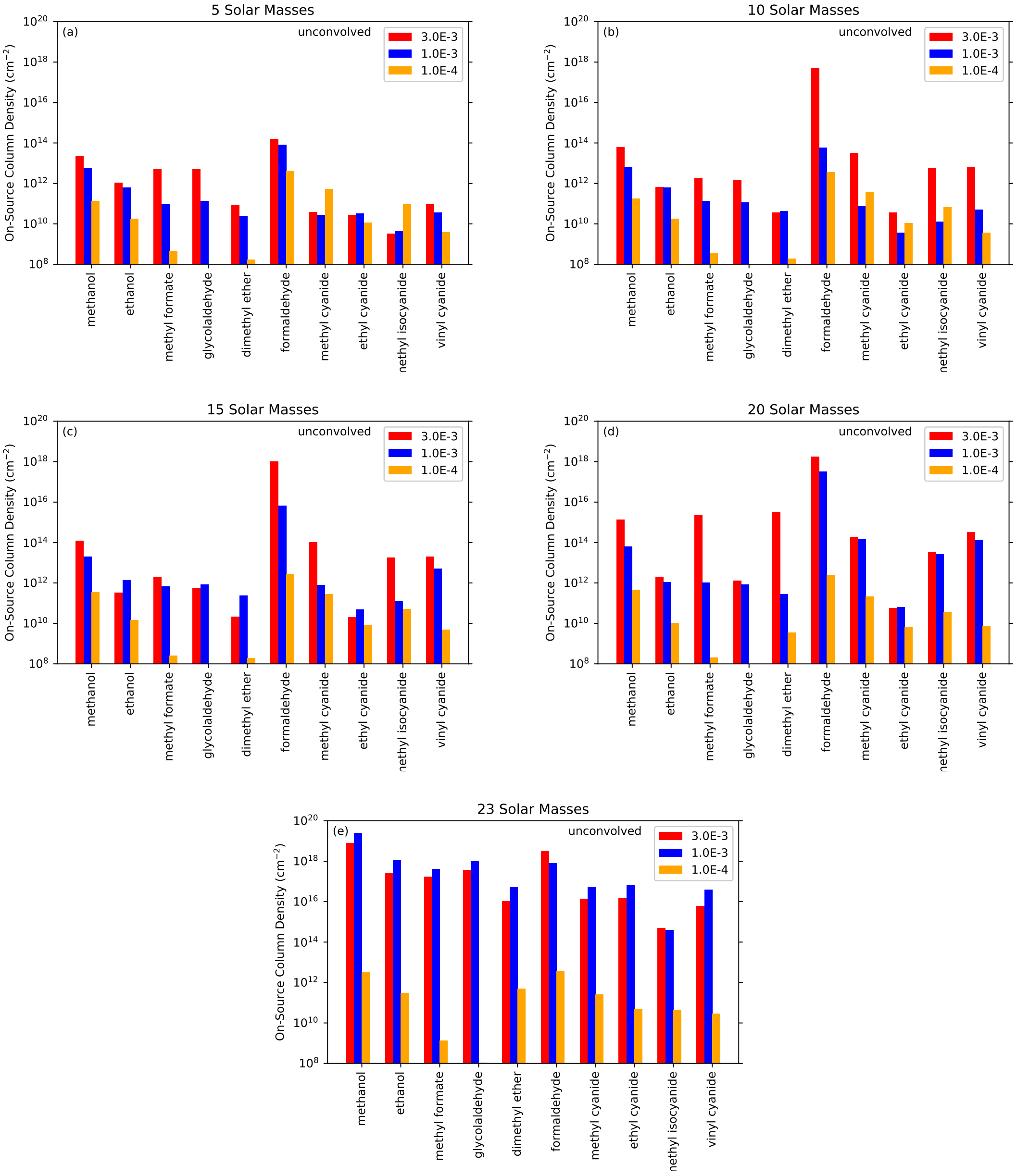

Figure 3.8: Unconvolved on-source column densities for select complex organic molecules. The red bars illustrate column densities for the 3.0×10^{-3} $M_{\odot}/yr$ model, the blue bars illustrate column densities for the 1.0×10^{-3} $M_{\odot}/yr$ model, and the orange bars illustrate column densities for the 1.0×10^{-4} $M_{\odot}/yr$ model. Panel (a) corresponds to stage-2 simulation times for which each model has a mass of 5 $M_{\odot}$, panel (b) corresponds to times for which each model has a mass of 10 $M_{\odot}$, panel (c) corresponds to times for which each model has a mass of 15 $M_{\odot}$, panel (d) corresponds to times for which each model has a mass of 20 $M_{\odot}$, and panel (e) corresponds to times for which each model has a mass of 23 $M_{\odot}$.

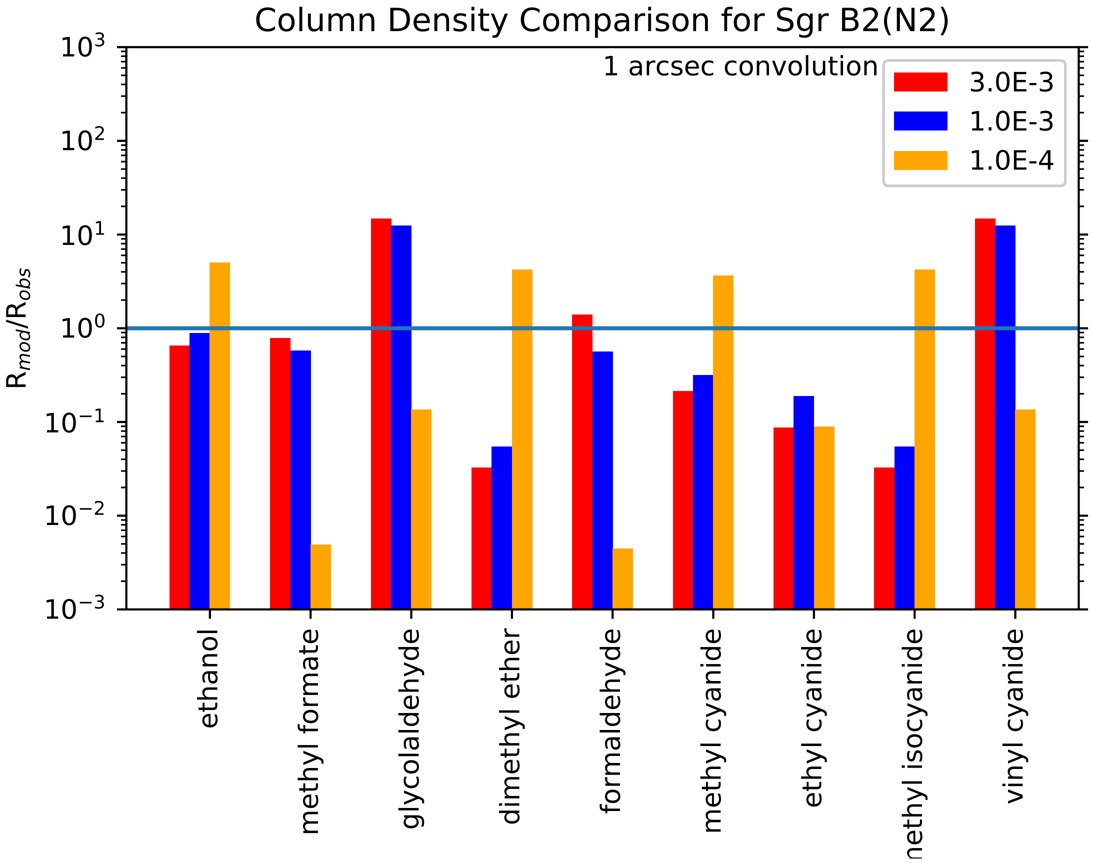

Figure 3.9: A comparison among observed column densities for select complex organic molecules toward Sgr B2(N2) and those modeled on-source using a 1 arcsec beam convolution. The red bars illustrate column densities for the 3.0×10^{-3} $M_\odot/yr$ model, the blue bars illustrate column densities for the 1.0×10^{-3} $M_\odot/yr$ model, and the orange bars illustrate column densities for the 1.0×10^{-4} $M_\odot/yr$ model. R_{mod} represents modeled column density ratios relative to methanol, and R_{obs} represents observed column density ratios relative to methanol (Jørgensen et al. 2020). The horizontal blue line indicates a value of 1 on the y-axis.

Evolution of Column Densities

In order to assess our results in a format commensurate with observational data, we integrate the absolute abundances of molecules along various lines of sight through the 1D core to obtain circularly-symmetric column density maps, which are then convolved with a gaussian beam (directed on-source). In this study we compare our results with molecular observations taken toward the high-mass star-forming core Sgr B2(N2). (Jørgensen et al. 2020) collated observational abundances of various COMs with respect to methanol toward this region, obtained from the EMoCA survey of Belloche et al. (2016). To compare directly with those values, column density maps from the chemical models are convolved using a 1" beam and an assumed distance to Sgr B2 of 8.34 kpc, following the measurements of Reid et al. (2014). The choice of beam size is intended to approximate the capabilities of ALMA in the 3 mm band.

Plots of on-source gas-phase column densities for various COMs are given in Figure 3.7. Panel (a) shows column densities obtained at the beginning of Stage 2. Panel (b) gives Stage-2 column densities calculated at a time corresponding to a temperature of 100 K for the innermost trajectory of each model. This occurs at 7.17×10^3, 2.47×10^4, and 2.88×10^5 yr, respectively, for the 3.0×10^{-3}, 1.0×10^{-3}, and 1.0×10^{-4} $M_\odot/yr$ models (see Figure 3.3). Panel (c) shows column densities at the final Stage-2 simulation time for each mass-accretion rate model.

The column densities at the initial Stage-2 simulation time (Figure 3.7) are all low compared with typical observational values, and typically range from 10^5 to 10^{10} cm^{-2}. This owes to the fact that the gas and grain temperatures are between 8 and 14 K at this time. Consequently, complex molecules do not have sufficient energy to thermally desorb from the grains, and the gas-phase column densities are low. However, when a temperature of 100 K is reached by the innermost trajectory, most COMs are beginning to desorb from the grains, and the column densities in panel (b) rise to values typically ranging from 10^{12} to 10^{15} cm^{-2}. At the final simulation time, all COMs have desorbed into the gas phase in a large fraction of the simulated trajectories, and column densities typically reach their highest values, which are in the approximate range 10^{16} to 10^{19} cm^{-2}.

Locally, complex molecules tend to become more abundant in the gas phase as the simulation proceeds, which leads to higher overall column densities. By the final simulation time, the column densities of the 3.0×10^{-3} and 1.0×10^{-3} $M_\odot/yr$ models are generally within an order of magnitude of each other (Figure 3.7). However, column densities in the 1.0×10^{-4} $M_\odot/yr$ model are consistently much lower by several orders of magnitude, partially because of the lower gas column density associated with the lower mass accretion rate.

Column Densities for Constant Source Mass

While it is instructive to consider the fractional abundances and column densities at various times throughout our models, each mass-accretion rate necessarily leads to a somewhat different physical outcome. In order to allow a more direct comparison between each physical model, we also consider the column densities produced by each at certain fixed masses achieved by the central source. To avoid differing beam-dilution effects between different accretion-rate models, based on their varied spatial extents, these on-source column densities are presented without convolution.

Unconvolved on-source column densities for source masses 5, 10, 15, 20, and 23

$M_\odot$ are shown in Figure 3.8 for various COMs. Generally, the column densities of all molecules increase with mass, which is true for all three mass-accretion rates. This owes to the fact that higher masses correspond to later simulation times; consequently, the overall gas column densities are higher due to the isotropic collapse, while the greater accretion and stellar luminosities (see Figure 3.2 for example) also lead to higher temperatures that are conducive to COM production and desorption.

The 3.0×10^{-3} $M_\odot/yr$ model generally features the highest column densities for all source masses, with the exception of 23 $M_\odot$ (Figure 3.8). The 1.0×10^{-4} model consistently features the lowest column densities. For instance, at 23 $M_\odot$ mass, column densities are up to around 7 orders of magnitude lower compared to the other two models. This trend is caused by two effects. First, a higher mass accretion rate leads to a higher gas column density. Second, and perhaps more importantly, a higher mass-accretion rate leads to a higher accretion luminosity for a given stellar mass, which, in turn, leads to higher temperatures, especially at relatively early times when the accretion luminosity dominates the stellar luminosity (see Figure 3.2 for an illustration). Both effects enhance the COM column densities as the accretion rate increases.

Comparing Observed and Modeled Column Densities

A comparison of our modeled column densities with those observed and previously modeled toward Sgr B2(N2) (Jørgensen et al. 2020 and references therein) is presented in Figure 3.9. The figure plots the ratio of our modeled column densities, R_{mod}, to observed column densities R_{obs}, where each quantity represents column densities relative to methanol. The horizontal blue line on the plot represents a value of 1, where $R_{mod} = R_{obs}$. The comparison with respect to methanol allows the further removal of possible confounding physical effects due to differences between the three accretion-rate models and/or Sgr B2(N2) itself; methanol should track well with the overall column density of the dense, hot gas within the core.

The comparison for ethanol is the best of any COM surveyed, as the agreement among R_{obs} and R_{mod} is within a factor of 10 for all mass accretion rate models (Figure 3.9), with an even closer match for the two highest mass accretion rates. The comparison for methyl formate and formaldehyde is also good for the 3.0×10^{-3} and 1.0×10^{-3} $M_\odot/yr$ models, as the agreement is also within a factor of 10. However, our modeled column densities for these COMs are severely under-produced for the 1.0×10^{-4} $M_\odot/yr$ model, as R_{mod} is more than two magnitudes lower than R_{obs}. All other COMs surveyed generally disagree with R_{obs} values by a factor of $10 - 100$ for all models. Furthermore, R_{mod} values are consistently lower than corresponding R_{obs} values, with the exception of a few cases.

3.4 Discussion

3.4.1 Fractional Abundances

Solid-phase abundances of COMs are mostly static in the Stage-2 simulations until thermal desorption occurs (Figures 3.5 and 3.6). Most COMs form on grains either during the Stage-1 collapse, or at relatively low temperatures (12 to 25 K) during the Stage-2 warm-up, and thus, grain-surface and mantle abundances plateau in

Stage 2. Once the species desorb, gas-phase abundances are also mostly static, with the exception of formaldehyde and methyl isocyanide, for the remainder of the simulation, for all models.

Gas-phase abundances are particularly static after species desorb, for all models/timescales; this effect is especially notable when comparing with previous modeling work (Garrod 2013; Barger & Garrod 2020). In those earlier studies, gas-phase abundances tend to diminish noticeably, especially for longer timescales, due to destruction by ionic species. The difference may be partially attributed to the present models' incorporation of proton-transfer reactions with ${NH_4}^+$, following the suggestion of Taquet et al. (2016), which allows protonated COMs to be de-protonated without destroying their structure, as would typically be the case if electronic recombination were the only destruction mechanism for those species. This addition diminishes a major gas-phase destruction pathway for COMs. Another reason for the relatively constant COM abundances is that, once a parcel of gas reaches a high enough temperature to thermally desorb COMs, it is already close to the central stellar object and falls into the star quickly, allowing little time for reactions. As may be seen in Figure 3.4, the time period available for gas-phase chemistry above 100 K is on the order of just a few thousand years. The corresponding timescales of the past models ranged from a few 10^4 years to more than half a million years.

Formaldehyde (H_2CO) is destroyed in the gas phase (Figures 3.5 and 3.6, panels d-f) due to reactions with atomic hydrogen and oxygen. This effect is especially pronounced in the 1.0×10^{-4} $M_\odot/yr$ model (panel f), owing to much higher abundances of both atomic hydrogen and oxygen. The low mass-accretion rate of this model is achieved by assuming low gas densities at the beginning of the Stage-2 collapse; this means that gas-phase reactions and freeze-out onto dust grains are less effective, while the visual extinction is also very low for trajectories starting at greater radii. Accordingly, atomic species are much more abundant in the gas phase for this model.

Gas- and solid-phase methyl formate (CH_3OCHO) and glycolaldehyde (CH_2OHCHO) abundances are severely diminished (by 3 to 4 orders of magnitude) in the 1.0×10^{-4} $M_\odot/yr$ model (Figures 3.5 and 3.6 panel (c)) compared to the other two mass accretion rate models. This is primarily caused by a scarcity of HCO on the dust grains, which otherwise leads to the formation of these species via radical addition with CH_3O/CH_2OH. During the early times in the models, at very low temperatures, CO from the gas phase is accreted onto the grains, where it is converted to formaldehyde (H_2CO) and thence to methanol (CH_3OH) via reactions with atomic H that originates in the gas phase. In the lowest mass-accretion rate model, the slow build-up of the ices (caused by low gas densities) combined with the high abundance of gas-phase H leads to the more complete hydrogenation of CO on the grain surfaces. This removes formaldehyde from the ice mantles, which could otherwise be photodissociated (or otherwise chemically processed) later on to produce the HCO needed for the above COMs to be formed.

Methyl isocyanide (CH_3NC) is destroyed in the gas phase due to reaction with atomic hydrogen (Figures 3.5 and 3.6, panels d-f), in agreement with the findings of Graninger et al. (2014). This effect is also pronounced in the 1.0×10^{-4} $M_\odot/yr$ model due to its large abundance of atomic hydrogen.

In general, the peak gas-phase abundances tend to be similar between the 3.0×10^{-3} and 1.0×10^{-3} $M_\odot/yr$ models for the innermost trajectory (see Table 3.2). In comparison with the lowest mass-accretion rate model, these two models tend to show greater local abundances for most species; however, for certain species, such as CH_3OCH_3, C_2H_5CN and CH_3CN, the lowest accretion rate model shows higher or comparable abundances.

The similarity in abundances between the 3.0×10^{-3} and 1.0×10^{-3} $M_\odot/yr$ models is related to their more similar mass-accretion rates and the associated physical and time-related conditions under which chemistry occurs. While the overall timescale of the low accretion-rate model is longer than the others, it is still approximately in inverse proportion to the lower final central density of that model (Table 3.1). However, the initial densities in each model vary much more strongly than this. As seen in Fig. 3.4, the innermost trajectory in the low mass-accretion rate model spends most of its time at gas densities on the order of 10^4 cm^{-3}, while the other models have densities for their innermost trajectories that are a factor 100 or 1000 higher. This far outweighs the longer timescale available to the low mass-accretion rate model. As a result, the amount of chemical evolution and overall ice build-up is substantially lower in the 1.0×10^{-4} $M_\odot/yr$ case. Also, while this model spends a much longer period of time at temperatures below 100 K than the other two (approximately 288,000 yr, vs. 24,000 and 7,000 yr), it spends a shorter time above (approximately 1,600 yr, vs. 4,200 and 2,800 yr), limiting the time available for any gas-phase production of COMs (in those cases where such processes exist, such as for dimethyl ether).

The only area in which the chemical evolution of the low mass-accretion rate model is favored is in the cosmic ray-induced photo-processing of the ice mantles, which produces reactive radicals. In spite of the lower abundance of solid-phase molecules as described above, the long timescale for this model allows the ices to experience a larger overall fluence of CR-induced UV photons, and therefore a larger degree of processing of the solid-phase material that is present.

In the low mass-accretion rate model, the abundances of CH_3CN, C_2H_5CN, and CH_3OCH_3 are elevated, whereas the abundances of CH_3OCHO, H_2CO, CH_3NC, and C_2H_3CN are diminished, as compared with the two higher mass-accretion rate models (Table 3.2). The elevated nitrogen-bearing species and dimethyl ether are likely formed in excess by the longer timescale due to cosmic-ray-induced photolysis of bulk-ice species; dimethyl ether may be formed solely from methanol dissociation products, so the lack of H_2CO in the ices in the low mass-accretion rate model is less important, while the longer timescale counterbalances the lower methanol abundance in the ice. In contrast to past models, CH_3OCH_3 is not formed in the gas phase in any substantial amount in any of the models, due to the short timescales available to gas-phase COM chemistry at temperatures greater than 100 K. In the case of CH_3NC, its gas-phase destruction is still rapid enough, through reactions with atomic H (Willis et al. 2020), to be apparent in all of the models, in spite of the short timescales available.

3.4.2 Column Densities

According to Figure 3.8, there does not appear to be consistency among column densities for all three mass-accretion rate models at constant source mass. Each of the five source masses illustrate a variety of column density values among the models for any particular species. This is likely due to the fact that although the source mass is constant, each model reflects a different simulation time, and thus temperature. Gas-phase fractional abundances and thus column densities, are particularly temperature-dependent, and the temperatures of these models are inconsistent at any given source mass. This is pronounced especially at 23 $M_\odot$ mass. The COM column densities of the 1.0×10^{-4} $M_\odot/yr$ model are significantly lower than the other two models because the temperature is much lower than those needed for COMs to desorb and the column density of the gas is also lower because of the lower mass accretion rate.

Our modeled column density ratios of CH_3NC to CH_3CN toward Sgr B2(N2) are 0.15, 0.17 and 1.2 respectively for the 3.0×10^{-3}, 1.0×10^{-3}, 1.0×10^{-4} $M_\odot/yr$ models. These values are relatively high compared to the best fit results toward Sgr B2(N) presented by Willis et al. (2020), which are 1.3×10^{-2} and 1.4×10^{-3}. Our values are also higher than the observational ratio of 4.5×10^{-3} toward Sgr B2(N2) reported by Jørgensen et al. 2020. This suggests that we may be overproducing isocyanide species in our models relative to normal cyanides.

Our modeled column densities are consistently lower than those observed and modeled toward Sgr B2(N2) (Figure 3.9). Although many uncertainties remain in our chemical network, the fact that the column densities are lower for all species suggests a potential systematic error. In particular, our physical profiles for all three models are inconsistent with that derived for Sgr B2(N2) (Bonfand et al. 2019). In all cases, the gas densities of our models are lower than those toward Sgr B2(N2) by a couple magnitudes, which could account for the comparatively lower column densities. Accordingly, comparing our results to those for Sgr B2(N2) may not be appropriate, and we may require a more compatible source for comparison in the future.

3.5 Conclusions

1. Gas-phase fractional abundances of the COMs we surveyed tend to remain static after thermal desorption occurs. This effect contrasts to the gradual diminishing of abundances over time from previous modeling studies, and is likely attributed to our incorporation of new gas-phase electronic recombination reactions in our network and short time interval between COM desorption and falling into the star.

2. Fractional abundances in the 3.0×10^{-3} and 1.0×10^{-3} $M_\odot/yr$ models are similar, and likely due to the fact that the physical conditions are similar. Fractional abundances in the 1.0×10^{-4} $M_\odot/yr$ model are higher for some species, and lower for others. The difference could be attributed to a longer timescale for some species to become abundant, and a lower gas column density and a lower temperature due to less heating from a lower accretion luminosity).

3. Column densities increase over time in the stage 2 simulation due to species thermally desorbing from grains at higher temperatures. Column densities also increase with source mass, as higher masses reflect higher temperatures from higher stellar and accretion luminosities.

4. There is no apparent consistency among column densities at constant source

mass. Although the source mass may be the same, the simulation time, temperature, and thus fractional abundances and column densities are different.

5. We consistently under-produce column densities for select species compared to observations and other calculations toward Sgr B2(N2). This is likely attributed to incompatibilities among our physical profiles and that modeled toward this source.

Chapter 4

A Look Ahead to Work Beyond this Thesis

The work in this thesis demonstrates the utility of astrochemical gas-grain modeling in the context of studying hot cores. Through the use of hot core modeling and observational data, we can suggest potential values of the cosmic-ray ionization rate ζ, and chemical warm-up timescale t_{wu} in several hot core sources. We can also derive useful relationships among source parameters, including the relationship between ζ and column density (N_H), and the relationship between t_{wu} and source mass (M) (Chapter 2). Furthermore, we introduce modeling hot cores with an explicit physical evolution using a three-phase chemical model coupled with radiation-hydrodynamics. We can study the effect of mass accretion rate and source mass on the abundances of several complex organic molecules (COMs), and evaluate how our abundances compare toward an observed source (Chapter 3). However, further study can be done following the work presented here to advance astrochemical modeling.

Some of the findings shown in Chapter 2 and 3 suggest general improvements can be made in astrochemical models. In Chapter 2, the chemical values of formaldehyde, formamide, and isocyanic acid produced by models systematically disagrees with observational values. Models can be improved in the future with better networks and parameters therein. More accurate branching ratios, reaction rates, and energy barriers could provide more robust results in further studies. We also address the issue of systematically under-producing column densities of COMs compared to observations for a particular source in Chapter 3. The physical parameters of the source may be incompatible with those use to model, or we might lack accurate physical profiles, or perhaps error may result from some combination of the two. In any case, more precise and accurate fits to physical profiles can benefit and limit uncertainties in astrochemical modeling.

More advanced improvements of astrochemical models can result from increasing the dimensionality of the modeling scheme itself. A major limitation of the work presented in chapters 2 and 3 is that only one spatial dimension is considered in modeling, which yields a spherically symmetric rendition of a hot core. This approach is an oversimplification of these systems, as there may be (are probably) spatial irregularities in real sources that can only be accounted for by modeling in higher dimensions. Furthermore, some attributes of star formation including magnetic effects (e.g. braking, drift), turbulence in gas parcels, and fragmentation can and probably do affect the chemical evolution of these objects significantly. Hot core modeling in 2 and 3 dimensions in the future will allow us to not only study the chemical response to these effects independently, but generate an overall more realistic and comprehensive physical and chemical modeling scheme of star formation.

Bibliography

[1] Allen, M., & Robinson, G. W. 1977, ApJ, 212, 396

[2] Allen, V., van der Tak, F. F. S., & Walsh, C. 2018, A&A, 616, A67

[3] Álvarez-Barcia, S., Russ, P., Kästner, J., & Lamberts, T. 2018, MNRAS, 479, 2

[4] Alvarez-Idaboy, J. R., Mora-Diez, N., Boyd, R. J., Vivier-Bunge, A. 2001, J. Am Chem Soc, 123, 2018

[5] Ball, J. A., Gottlieb, C. A., Lilley, A. E., & Radford, H. E. 1970, ApJL, 162, L203

[6] Barger, C. J., & Garrod, R. T. 2020, ApJ, 888, 38

[7] Barone, V., Latouche, C., Skouteris, D., et al. 2015, MNRAS, 453, L31

[8] Bisschop, S. E., Jørgensen, J. K., van Dishoeck, E. F., & de Wachter, E. B. M. 2007, A&A, 465, 913

[9] Belloche, A., Garrod, R. T., Müller, H. S. P., et al. 2009, A&A, 499, 215

[10] Belloche, A., Garrod, R. T., Müller, H. S. P., & Menten, K. M. 2014, Science, 345, 1584

[11] Belloche, A., Meshcheryakov, A. A., Garrod, R. T., et al. 2017, A&A, 601, A49

[12] Belloche, A., Müller, H. S. P., Garrod, R. T., et al. 2016, A&A, 587, A91

[13] Bergin, E. A., Alves, J., Huard, T., & Lada, C. J. 2002, ApJ, 570, L101

[14] Beuther, H., Linz, H., & Henning, Th. 2013, A&A, 558, A81

[15] Bohlin, R. C., Savage, B. D., & Drake, J. F. 1978, ApJ, 224, 132

[16] Bonfand, M., Belloche, A., Garrod, R. T., et al. 2019, A&A, 628, A27

[17] Brogan, C. L., Hunter, T. R., Cyganowski, C. J., et al. 2016, ApJ, 832, 187

[18] Brogan, C. L., Hunter, T. R., Cyganowski, C. J., et al. 2018, ApJ, 866, 87

[19] Butscher, T., Duvernay, F., Danger, G., & Chiavassa, T., 2016, A&A, 593, A60

[20] Caproni, A., Abraham, Z., & Vilas-Boas, J. W. S. 2002, IAU Symposium, 206

[21] Caselli, P., Walmsley, C. M., Terzieva, A., & Herbst, E. 1998, ApJ, 499, 234

[22] Ceccarelli, C., Hily-Blant, P., Montmerle, T., et al. 2011, ApJL, 740, L4

[23] Chang, P., Davis, S. W., & Jiang, Y.-F. 2020, MNRAS, 493, 5397

[24] Charnley, S. B., Tielens, A. G. G. M., & Millar, T. J. 1992, ApJ, 399, L71

[25] Charnley, S. B., Kress, M. E., Tielens, A. G. G. M., & Millar, T. J. 1995, ApJ, 448, 232

[26] Chen, H. R., Welch, W. J., Wilner, D. J., Sutton, E. C. 2006, ApJ, 639, 975

[27] Cheung, A. C., Rank, D. M., Townes, C. H., Thornton, D. D., & Welch, W. J. 1968, PhRvL, 21, 1701

[28] Cheung, A. C., Rank, D. M., Townes, C. H., Thornton, D. D., & Welch, W. J. 1969, Natur, 221, 626

[29] Choudhury, R., Schilke, P., Stephan, G., Bergin, E., Möller, T., Schmiedeke, A., & Zernickel, A. 2015, A&A, 575, A68

[30] Clements, A. R., Berk, B., Cooke, I. R., & Garrod, R. T. 2018, Phys. Chem. Chem. Phys., 20, 5553

[31] Csengeri, T., Belloche, A., Bontemps, S., et al. 2019, A&A, 632, A57

[32] Cuppen, H. M., & Herbst, E. 2005, MNRAS, 361, 565

[33] Davis, S. W., & Gammie, C. F. 2020, ApJ, 888, 94

[34] DeMore, W. B., Sander, S. P., Golden, D. M., et al. 1997, Jet Propulsion Laboratory Publication, 97-4, 1

[35] Douglas, A. E., & Herzberg 1941, ApJ, 94, 381

[36] Duley, W. W. & Williams, D. A. 1993, MNRAS, 260, 37

[37] Duley, W. W., & Williams, D. A. 1984, Interstellar Chemistry (London: Academic Press)

[38] Favre, C., Ceccarelli, C., López-Sepulcre, A., et al. 2018, ApJ, 859, 136

[39] Gaches, B. A. L., Offner, S. S. R., & Bisbas, T. G. 2019, ApJ, 878, 105

[40] Garrod, R. T., Belloche, A., Müller, H. S. P., & Menten K. M. 2017, ApJ, 601, A48

[41] Garrod, R. T., & Herbst, E. 2006, A&A, 457, 927

[42] Garrod, R. T. 2008, A&A, 491, 239

[43] Garrod, R. T. 2013, ApJ, 765, 60

[44] Garrod, R. T., & Pauly, T. 2011, ApJ, 735, 15

[45] Garrod, R. T., Wakelam, V., & Herbst, E. 2007, A&A, 467, 1103

[46] Garrod, R. T.,Widicus Weaver, S. L., & Herbst, E. 2008, ApJ, 682, 283

[47] Garrod, R. T., & Widicus Weaver, S. L. 2013, Chem. Rev., 113, 8939

[48] Geppert, W. D., et al. 2006, Faraday Discuss. 133, Chemical Evolution of the Universe (Cambridge: RSC Pub.), 177

[49] Goldsmith, P. F., & Langer, W. D. 1999, ApJ, 517, 209

[50] Graninger, D. M., Herbst, E, Öberg, K. I., & Vasyuninm, A. I. 2014, ApJ, 787, 74

[51] Hamberg, M., Österdahl, F., Thomas, R. D., et al. 2010, A&A, 514, A83

[52] Hasegawa, T. I., & Herbst, E. 1993, MNRAS, 263, 589

[53] Hasegawa, T. I., Herbst, E., & Leung, C. M., 1992, ApJS, 82, 167

[54] Herbst, E., & Klemperer, W. 1973, ApJ, 185, 505

[55] Herbst, E., & Leung, C. M. 1986, ApJ, 310, 378

[56] Herbst, E. & Millar, T. J. 2008, The Chemistry of Cold Interstellar Cloud Cores ed Smith, I. W. M. (London: Imperial College Press), 1

[57] Herbst, E., & van Dishoeck, E. F. 2009, ARA&A, 47, 427

[58] Hidaka, H., Watanabe, N., Shiraki, T., Nagaoka, A., & Kouchi, A. 2004, ApJ, 614, 1124

[59] Hosokawa, T., & Omukai, K. 2009, ApJ, 691, 823

[60] Ivlev, A. V., Padovani, M., Galli, D., & Caselli, P. 2015, ApJ, 812, 135

[61] Izquierdo, A. F., Galvan-Madrid, R., Maud, L. T., et al. 2018, MNRAS, 478, 2505

[62] Jiang, Y.-F., Stone, J. M., & Davis, S. W. 2019, ApJ, 880, 67

[63] Jørgensen, J. K., Belloche, A., & Garrod, R. T. 2020, ARA&A, 58:1-55

[64] Kalváns, J. 2018, MNRAS, 478, 2

[65] Kuiper, R., Klahr, H., Beuther, H., et al. 2010, ApJ, 722, 1556

[66] Le Petit, F., Roueff, E., & Herbst, E. 2004, A&A, 417, 993

[67] Le Petit, F., Ruaud, M., Bron, E., et al. 2016, A&A, 585, A105

[68] Li, Z.-Y., Krasnopolsky, R., & Shang, H. 2011, ApJ, 738, 180

[69] Liszt, H. S., 2020, ApJ, 897, 104L

[70] McGuire, B. A., 2018, ApJS, 239, 17

[71] McKellar, A. 1940, PASP, 52, 187

[72] Millar, T. J., Herbst, E., & Charnley, S. B. 1991, ApJ, 369, 147

[73] Molinari, S., Brand, J., Cesaroni, R., & Palla, F. A&A, 355, 617

[74] Nakano, T., Nishi, R., & Umebayashi, T. 2002, ApJ, 573, 199

[75] Nejad, L. A. M., Williams, D. A., & Charnley, S. B. 1990, ApJ, 246, 183

[76] Öberg, K. I., Garrod, R. T., van Dishoeck, E. F., & Linnartz, H. 2009a, A&A, 504, 891

[77] Öberg, K. I., van Dishoeck, E. F., & Linnartz, H. 2009b, A&A, 496, 281

[78] Öberg, K. I., van Dishoeck, E. F., & Linnartz, H. 2009c, ApJ, 693, 1209

[79] Ocana, A. J,. Jiménez, E., Canosa, A., et al. 2017, ApJ, 850, 28

[80] Oka, T., Geballe, T. R., Goto, M., Usuda, T., & McCall, B. J. 2005, ApJ, 632, 882

[81] Padovani, M., & Galli, D. 2011, aap, 530, A109

[82] Padovani, M., Galli, D., Ivlev, A. V., et al. 2018, A&A, 614, A144

[83] Padovani, M., Walmsley, C. M., Tafalla, M., et al. 2009, A&A, 505, 1199

[84] Prasad, S. S., & Tarafdar, S. P. 1983, ApJ, 267, 603

[85] Reid, M. J., Menten, K. M., Brunthaler, A. et al. 2014, ApJ, 783, 130

[86] Rimmer, P. B., Herbst, E., Morata, O., & Roueff, E. 2012, A&A, 537, A7

[87] Rimola, A., Taquet, V., Ugliengo, P., et al. 2014, A&A, 572, A70

[88] Shingledecker, C. N., Le Gal, R., & Herbst, E. 2017, Phys. Chem. Chem. Phys., 19, 11043

[89] Shingledecker, C. N., Tennis, J. D., Le Gal, R., & Herbst, E. 2018, ApJ, 861, 1

[90] Shu, F. H. 1977, ApJ, 214, 488

[91] Snyder, L. E., Buhl, D., Zuckerman, B., & Palmer, P. 1969, PhRvL, 22, 679

[92] Snyder, L. E., Lovas, F. J., Hollis, J. M., et al. 2005, ApJ, 619, 914

[93] Song, L., & Kästner, J. 2016, Phys. Chem. Chem. Phys., 18, 29278

[94] Stone, J. M., Tomida, K., White, C. J., et al. 2020, arXiv e-prints, arXiv:2005.06651

[95] Swings, P., & Rosenfeld, L. 1937, ApJ, 86, 483

[96] Taquet, V., Charnley, S. B., & Sipila, O. 2014, ApJ, 791, 1

[97] Taquet, V., Wirström, E. S., & Charnley, S. B. 2016, ApJ, 821, 46

[98] Tideswell, D. M., Fuller, G. A., Millar, T. J., & Marwick, A. J. 2010, A&A, 510, A85

[99] van der Tak, F. F. S., & van Dishoeck, E. F. 2000, A&A, 358, L79

[100] van der Tak, F. F. S., Belloche, A., Schilke, P., et al. 2006, A&A, 454, L99

[101] van der Tak, F. F. S., van Dishoeck, E. F., Evans, N. J., II, & Blake, G. A. 2000, ApJ, 537, 283

[102] Vaupré, S., Hily-Blant, P., Ceccarelli, C., et al. 2014, A&A, 568, A50

[103] Viti, S., Collings, M. P., Dever, J. W., McCoustra, M. R. S., & Williams, D. A. 2004, MNRAS, 354, 1141

[104] Viti, S., & Williams, D. A. 1999, MNRAS, 354, 1141

[105] Watanabe, N. & Kouchi, A. 2002, ApJ, 571, L173

[106] Walsh, C., Millar, T. J., 2014, An Introduction to Astrochemical Modeling. *UMIST Database for Astrochemistry*, 1-9

[107] Webber, W. R. 1998, ApJ, 506, 329

[108] Weinreb, S., Barrett, A. H., Meeks, M. L., & Henry, J. C. 1963, Natur, 200, 829

[109] Whittet, D. C. B., Gerakines, P. A., Hough, J. H. & Shenoy, S. S. 2001, ApJ, 547, 872

[110] Willis, E. R., Garrod, R. T., Belloche, A., et al. A&A, accepted

[111] Yetter, R. A., Rabitz, H., Dryer, F. L., et al. 1989, J. Chem. Phys., 91, 4088

[112] Yusef-Zadeh, F., Hewitt, J. W., Wardle, M., et al. 2013, ApJ, 762, 33

[113] Zanchet, Z., del Mazo, P., Aguado, A., et. al. 2018, Phys. Chem. Chem. Phys., 20, 5415